Symmetries and Large N Limits of Majorana Fermion Models

Preethi N. Pallegar

A Dissertation
Presented to the Faculty
of Princeton University
in Candidacy for the Degree
of Doctor of Philosophy

Recommended for Acceptance
by the Department of
Physics
Adviser: Igor R. Klebanov

September 2021

Abstract

In this thesis, we study generalizations of well-known Majorana fermion models, including the SYK model and the Klebanov-Tarnopolsky tensor model. The models are compared at finite and large N, where we find that the models simplify considerably and can even become solvable.

In chapter 2, we study quantum mechanical models in which the dynamical degrees of freedom are real fermionic tensors of rank five and higher. For the tensors of rank five, there is a unique $O(N)^5$ symmetric sixth-order Hamiltonian leading to a solvable large N limit dominated by the melonic diagrams. We solve the large N Schwinger-Dyson (SD) equations for higher rank Majorana tensor models and show that they match those of the corresponding SYK models exactly.

In chapter 3, we study a family of tensor models of complex fermions, with a six fermion interaction whose index structure resembles the topology of a prism. The model is dominated by melonic diagrams in the large N limit after introducing an auxiliary field. We consider interactions that preserve the $U(1)$ global symmetry, solving the SD equations at large N and examining the bilinear spectrum. We find a complex scaling dimension in the $U(1)$ charged sector in addition to an $\mathcal{O}(1)$ gap between the ground and first excited states. This model has a negative charge compressibility.

In chapter 4, we present a class of Hamiltonians H for which a sector of the Hilbert space invariant under a Lie group G, which is not a symmetry of H, possesses the essential properties of many-body scar states. These include the absence of thermalization and the 'revivals' of special initial states. Our study of an extended 2D tJU model illustrates the properties of the invariant scars and supports our findings.

Acknowledgements

There are many people who have supported me throughout my time at Princeton. Firstly, I would like to thank Igor Klebanov, for his valuable guidance and patience. He is a kind and brilliant person, and his discussions, encouragement, and suggestions have made my PhD possible. I am lucky to have learned from him and to have had him as an adviser.

I would like to thank Simone Giombi for being on my committee and also for providing advice and guidance for the complex prismatic project. I want to also thank Sanfeng Wu for serving on my committee, and thank you to Silviu Pufu for being my second reader. I am grateful to Juan Maldacena for teaching me about the SYK model early on in my PhD. I am also very grateful to Kiryl Pakrouski, Fedor Popov, and Wenli Zhao for their collaborations and discussions.

I want to thank Barbara Engelhardt for advising me during my experimental project, and I also want to thank Kasey Wagoner for being a great lab manager. His passion for teaching is inspiring, and I have enjoyed working with him throughout my time in Princeton. I am grateful to Kate Brosowsky for always answering any questions I had, and for being such a patient and kind person. I am thankful to Akash Maharaj, Natalie Paquette, Nathan Benjamin, Jordan Cotler, and I am especially thankful to Raghu Mahajan, for all of their help and guidance throughout my undergraduate and graduate career. I would also like to thank my undergraduate adviser, Shamit Kachru, for inspiring me to pursue physics.

Thank you to all of my friends I met in Princeton: Sarah Marie Bruno, Wonjae Lee, Himanshu Khanchandani, Wayne Zhao, Henry Lin, Lisa Jian, Joe Eichenhofer,

Ksenia Bulycheva, Steven Li, Boya Wen, Ziming Ji, Akshay Yelleshpur Srikant, Ho Tat Lam, Akash Goel, Diana Valverde Mendez, Christian Jepsen, Jim Wu, Corwin Shiu, Nana Shumiya, Nikolay Sukhov, Connie Phung, Sagar Setru, Shao Ma, and I am also very thankful to the Princeton climbing community. I have enjoyed countless conversations, movie nights, dinners, climbing adventures, and baking parties with you. You all have made my time at Princeton wonderful.

I want to thank Sara Altman, for being my closest friend and a constant source of support since our first year of college. I look forward to many adventures with you.

Finally, I want to thank my family. Thank you to my parents, Naresh and Krishna Pallegar, and to my brother, Praveen Pallegar, for your love and support throughout my life. I could not have done this without you. And thank you to my husband, Amr Mohamed, for your patience, love, and support, and for always believing in me. I dedicate this thesis to you.

To my husband, Amr.

Contents

Chapter 1

Introduction

In this chapter, we introduce and motivate the study of models where the number of the degrees of freedom, N, becomes very large. In this large N limit, several models simplify, becoming more tractable and sometimes even analytically solvable. We begin by briefly reviewing well known limits in the cases of vector and matrix models, and then move on to describe the large N behavior of tensor models and the Sachdev-Ye-Kitaev (SYK) model, which are a focus of this work. We end this chapter with a general overview of various metrics of quantum chaos, which we use later on to understand information preservation in thermalizing systems.

The SYK model is an example of a strongly interacting chaotic system that is exactly solvable at large N. It is valuable to understand this and closely related models, namely tensor models, so we can learn about how chaotic behavior and similar properties appear in other strongly interacting models. This model is not only relevant in high energy theory, but it is one that is also very relevant in condensed

matter theory, and in fact originated from a model of a random quantum Heisenberg magnet [1]. Because of its random couplings, the SYK model requires averaging over many ensembles, and so it is not a usual quantum mechanical model. Tensor models, however, do not require this averaging over disorder and share many of the large N properties of the SYK model. In fact, quantum mechanical models in which the dynamical degrees of freedom are fermionic tensors of rank 3 and higher have attracted much attention in recent literature, starting with the papers [2, 3].

At large N, the dominating diagrams for both the tensor and SYK models are the same, and their dominant 'melonic' diagrams can be studied and simply summed [3–11] (for reviews, see [12–15]). As a result, the large N tensor and SYK models are closely related, although there are also some important differences [15]. These differences are manifest in the small N exact diagonalizations of the Hamiltonians [16–21], since it is harder to numerically study the spectrum of the tensor model as the Hilbert space has dimension $\sim 2^{N^{(q-1)/2}}$, whereas the SYK Hilbert space has dimension $\sim 2^{N/2}$. However, we expect to numerically observe chaotic features, like a dip ramp plateau structure in the spectral form factor (SFF), in the tensor models at large enough N. Furthermore, these models are solvable at large N and may be considered as examples of holography. The SYK and tensor models have (nearly) conformal behavior at large N and the SYK model may be dual to the two-dimensional Anti-de Sitter (AdS_2) space [4]. This duality is further supported when we examine the chaos properties of the model. The SYK model has a SFF characteristic of a random Gaussian matrix, and it saturates the chaos bound, as we would expect for a model dual to a black hole [22].

In addition to studying the spectral and chaos properties of the SYK and tensor models, we also study the chaos properties of several vector and matrix models. We are particularly interested in models with a chaotic bulk and a non-thermalizing subsector. These non-thermalizing states are called scar states, and a key property is that they violate the eigenstate thermalization hypothesis (ETH).

1.1 Large N Limits

A notable example of the utility of large N methods is in the application to the $O(N)$ ferromagnet. The model has energy $E = -J\sum_{\langle ij\rangle}\vec{n}_i\cdot\vec{n}_j$ where $\vec{n} = (n^1,\ldots,n^N)$, $\vec{n}^2 = 1$, $J > 0$ and $\langle ij\rangle$ are the nearest neighbor lattice sites. This model has a second order phase transition, and close to the critical βJ, has the action [15],

$$\begin{aligned} S &= \int d^dx\,\left[\frac{1}{2}\left(\nabla\phi_i\right)^2 + \frac{m^2}{2}\phi_i^2 + \frac{g}{4}\left(\phi_i^2\right)^2\right] \\ &= \int d^dx\,\left[\frac{1}{2}\left(\nabla\phi_i\right)^2 - \frac{i}{2}\sigma\phi_i^2 + \frac{1}{4g}\sigma^2\right], \end{aligned} \tag{1.1.1}$$

where the auxiliary field σ is introduced in the second line. Integrating out the N ϕ_i fields gives a $1/N$ expansion for the scaling dimensions, see [15, 23, 24]. The resulting expansion matches very closely with numerical results [25].

Another useful application of the large N methods is in $SU(N)$ gauge theory, where 't Hooft defined the large N limit keeping g^2N fixed (g is the Yang-Mills coupling) [26]. In $d = 3$, [27] found that at large N, finite volume corrections to the glueball masses are suppressed. This is because the glueball operators are single trace, whereas the finite volume states are double trace and therefore will be subleading at

large N. The $1/N$ mass expansion,

$$\frac{M}{g^2 N} = c_0 + \frac{c_1}{N^2} + \frac{c_2}{N^4} + \dots \tag{1.1.2}$$

where $g^2 N$ is the 't Hooft coupling, has good agreement with the low-lying glueball masses [15, 27].

In this section, we review two examples of large N limits in some detail. This first is that of a vector model and the second is that of a matrix model. Vector models have degrees of freedom that transform as N-component vectors, whereas matrix models have degrees of freedom that transform as matrices of size $N \times M$.

1.1.1 Vector model

To illustrate the large N simplifications of the vector model, we can consider an example where we have an $O(N)$ symmetric theory with N scalar fields in zero dimensions with a double trace $\frac{g}{24}(\phi^a \phi^a)^2$ interaction. We start by writing the general partition function for theory with the ϕ^4 interaction [15],

$$Z = \prod_{i=1}^{n} \int_{-\infty}^{\infty} \frac{d\phi_i}{\sqrt{2\pi}} e^{-\frac{1}{2}\phi_i \phi_i - \frac{1}{24} J_{ijkl} \phi_i \phi_j \phi_j \phi_l} \tag{1.1.3}$$

Here, J_{ijkl} is a fully symmetric tensor. We can write the logarithm of Z via the graph expansion at various orders of interaction, see figure 1.1.

The single vertex interaction is the figure eight diagram, and double vertex diagrams are the 'melonic' diagram and the triple bubble diagram. The symmetry factors of the expansion are determined combinatorially, and each vertex has a factor

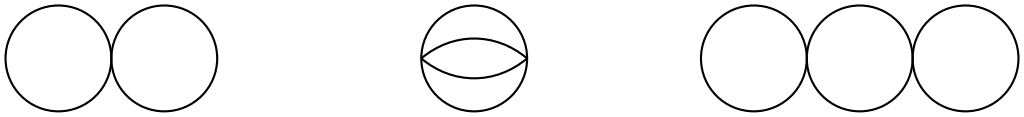

Figure 1.1: Left: figure eight diagram, middle: 'melonic' diagram, right: triple bubble diagram.

of $-J_{ijkl}$. And so we can write the logarithm of Z as follows,

$$\log Z = -\frac{J_{iijj}}{8} + \frac{J_{ijkl}J_{ijkl}}{2 \cdot 4!} + \frac{J_{iikl}J_{jjkl}}{2^4} + \mathcal{O}(J^3) \tag{1.1.4}$$

Now let us consider the $O(N)$ symmetric model with the $\frac{g}{24}(\phi^i\phi^i)^2$ interaction. In this case, we let J_{ijkl} be equal to $\frac{g}{3}(\delta_{ij}\delta_{kl} + \delta_{ij}\delta_{kl} + \delta_{ij}\delta_{kl})$. Now we can expand the coefficients in equation (1.1.4) in terms of δ_{ij},

$$\begin{aligned} J_{iijj} &= \frac{g}{3}(\delta_{ii}\delta_{jj} + 2\delta_{ij}\delta_{ij}) = \frac{g}{3}(N^2 + 2N) \\ J_{ijkl}J_{ijkl} &= \frac{3g^3}{9}((\delta_{ij}\delta_{kl})^2 + \delta_{ij}\delta_{kl}\delta_{ik}\delta_{jl} + \delta_{ij}\delta_{kl}\delta_{il}\delta_{jk}) = \frac{3g^2}{9}(N^2 + 2N) \\ J_{iikl}J_{jjkl} &= \frac{g^2}{9}(\delta_{ii}\delta_{kl} + \delta_{ik}\delta_{il} + \delta_{il}\delta_{ik})^2 = \frac{g^2}{9}N(N+2)^2. \end{aligned} \tag{1.1.5}$$

Plugging this into equation (1.1.4) and dividing both sides by N, we have

$$\frac{\log Z}{N} = -\frac{N+2}{24}g + \frac{N+2}{144}g^2 + \frac{(N+2)^2}{144}g^2 + \mathcal{O}(g^3) \tag{1.1.6}$$

Above, the first term corresponds to the connected snail diagram, the second corresponds to the melon graph, and the third corresponds to the triple bubble diagram.

We can also note the powers of N in each of these diagrams by labeling the indices and counting the closed index loops. If we want this expansion to be finite in the

Figure 1.2: Left: Graphical representation of the quartic interaction vertex in equation (1.1.8). Right: Graphical representation of the quartic interaction vertex in equation (1.2.1).

large N limit, we must hold $\lambda = gN$ fixed. We can think of sending N to infinity while we send g to 0, so gN remains constant. Rewriting equation (1.1.6) terms of λ,

$$\frac{\log Z}{N} = -\lambda\left(\frac{1+2/N}{24}\right) + \frac{\lambda^2}{N}\left(\frac{1+2/N}{144}\right) + \lambda^2\left(\frac{1+2/N+4/N^2}{144}\right) + \mathcal{O}(\lambda^3) \quad (1.1.7)$$

When we do this, it is clear that the melonic diagrams are suppressed at order $\frac{1}{N}$. So for sufficiently small coupling, we can write our partition function as a convergent sum corresponding to the snail diagrams.

1.1.2 Matrix model

The second class of large N limits we discuss are called matrix models. Here we have N^2 degrees of freedom and our particles are treated as real $N \times N$ matrices. We let each index have $O(N)$ symmetry so that the model is in the bi-fundamental representation. We let the model have a quartic interaction term, and we can represent the interaction vertex as a two color fat graph, see figure 1.2.

In this example, we only consider the single trace $\frac{g}{4}(\phi^{i_1 j_1}\phi^{i_1 j_2}\phi^{i_2 j_1}\phi^{i_2 j_2})$ interaction, and can write the partition function as follows,

$$Z = \prod_{i,j=1}^{n} \int_{-\infty}^{\infty} \frac{d\phi^{ij}}{\sqrt{2\pi}} e^{-\frac{1}{2}\phi^{ij}\phi^{ij} + \frac{g}{24}\phi^{i_1 j_1}\phi^{i_1 j_2}\phi^{i_2 j_1}\phi^{i_2 j_2}} \tag{1.1.8}$$

Using a similar procedure to the vector model, we can solve for the log of the partition function to get the following,

$$\frac{\log Z}{N^2} = -\frac{2N+1}{24}g + \frac{N^2+2N+3}{288}g^2 + \frac{(2N+1)^2}{144}g^2 + \dots \tag{1.1.9}$$

We can see that we have a finite solution when we keep $\lambda = gN$ fixed. Except in this case, the melons and snails both contribute, so more diagrams survive compared to the vector model, making this a more complex model.

1.2 Klebanov-Tarnopolsky and SYK Models

1.2.1 Tensor model

The third class of large N limits we examine is tensor models. In this section, we consider the rank three four fermion Klebanov-Tarnopolsky tensor model, proposed and solved in [3]. It is an $O(N)^3$ symmetric quantum mechanical model for Majorana fermions, and the unique non-trivial quartic (maximally single trace) interaction vertex is represented in figure 1.2. The three indices are distinguishable, and each fermion pair shares exactly one index in common. Here, repeated indices are summed

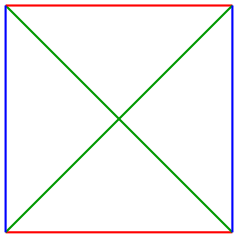

Figure 1.3: The graphical representation of the tetrahedral operator in equation (1.2.1).

over and each of the indices ranges from 1 to N.

$$H_{\text{tetra}} = \frac{g}{4}\psi^{abc}\psi^{ab'c'}\psi^{a'bc'}\psi^{a'b'c} \quad \text{where,} \quad \{\psi^{a_ib_ic_i}, \psi^{a_jb_jc_j}\} = \delta^{a_ia_j}\delta^{b_ib_j}\delta^{c_ic_j}. \tag{1.2.1}$$

This is called a 'tetrahedral' interaction because of the form of its corresponding graph, see figure 1.3. In the interaction graph, we let each edge of the graph represent an index contraction, the vertices represent the fermions, and the distinct colors represent the three distinct $O(N)$ groups.

The model transforms under the tri-fundamental representation of $O(N)^3$:

$$\psi^{abc} \to M_1^{aa'}M_2^{bb'}M_3^{cc'}\psi^{a'b'c'}, M_1, M_2, M_3 \in O(N). \tag{1.2.2}$$

We consider only this tetrahedral interaction of the four allowed quartic operators since the others have a smaller vertex to index loop ratio, and thus decay to zero at a faster rate. The allowed quartic operators include the unique $q = 4$ tetrahe-

dral operator in equation (1.2.1), and three 'pillow operators' of the general form $\psi^{a_1 b_1 c_1}\psi^{a_2 b_1 c_1}\psi^{a_2 b_2 c_2}\psi^{a_1 b_2 c_2}$.[a]

Using the same method as for the vector and matrix examples, we can expand the the log of the partition function of the model via the graph expansion, see figure 1.1. The snail diagram gives us one factor of g and one factor of N from a single index loop. The middle, melonic diagram, gives us a factor of g^2 from the two vertices along with a factor of N^3 from three closed index loops. Finally, the last triple bubble diagram has two vertices giving us a factor of g^2 with only two closed index loops giving a factor of N^2. Only including the terms with largest contribution from each of the three diagrams, we have,

$$\begin{aligned}\frac{\log Z}{N^3} &= \mathcal{O}\left(gN\right) + \mathcal{O}\left(g^2N^3\right) + \mathcal{O}\left(g^2N^2\right) + \dots \\ &= \mathcal{O}\left(\frac{\lambda}{\sqrt{N}}\right) + \mathcal{O}\left(\lambda^2\right) + \mathcal{O}\left(\frac{\lambda^2}{N}\right) + \dots\end{aligned} \tag{1.2.3}$$

In the second line we let $\lambda = gN^{3/2}$. When we hold λ constant, we can see that the melonic diagram has the only surviving contribution in the large N limit. Since only the melonic diagram survives in the large N limit, the tensor models appear to be simpler than the matrix models reviewed earlier in section 1.1.2. These diagrams are the same as in the Sachdev-Ye-Kitaev (SYK) model [4, 29–33], where the quartic interactions contain a random four-index tensor.

The melonic dominance in this model can be proved using Euler's theorem, which states that $f = \chi + e - v$, where f, e, and v are the numbers of faces, edges, and

[a]The three quartic terms of 'pillow' topology [11] are the quadratic Casimir operators of the three $SO(N)$ groups [28] and are, therefore, determined by the group representation. In the gauged model they vanish.

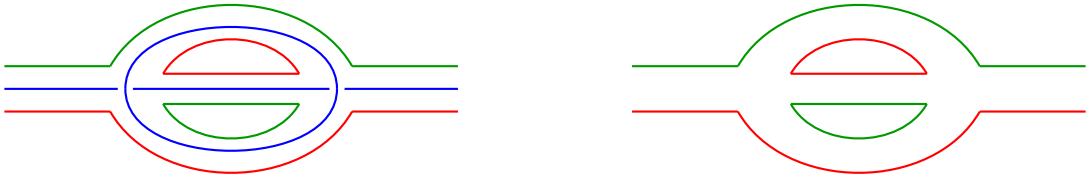

Figure 1.4: Left: The melonic diagram with interaction vertex (1.2.1). Right: The melonic fat graph of (1.2.1) where we have erased the blue lines.

vertices respectively, and χ is the Euler characteristic. To use Euler's theorem, we will draw fat graphs, meaning we erase one of the three colors in the graph, and count the number of loops from two colors at a time. In this theory we have $e = 2v$, so we can simplify to $f = \chi + v$. We want to use this equation to calculate a bound on the number of faces, f, or closed loops, because this gives us the factors of N.

Let us first focus of the fat graph with only green and red, as in figure 1.4; we will call the green line index a and the red line index c. Thus the total number of faces of this diagram is $f_{ac} = f_a + f_c$. Adding the faces in the three possible fat graphs, we get that $f_{ab} + f_{bc} + f_{ac} = 2(f_a + f_b + f_c) = \chi_{ab} + \chi_{bc} + \chi_{ac} + 3v$. Following the derivation in [3], we can use the fact that the Euler character, χ, is equal to $2 - 2g$ to find a bound on the number of faces. We get $f_{tot} \leq 3 + \frac{3v}{2}$ since the genus is nonnegative, $g \geq 0$. The proof is completed in [3] by showing that all graphs saturating this bound are melonic. Since the leading free diagrams contribute at order N^3, we find the large N limit when $\lambda = g^2 N^3$.

We can sum up the melonic contributions to the propagator to find the full two point function in the IR limit, and we can also study the four point function to get the spectrum of bilinears. Both calculations are done in detail for the general q tensor

model with the maximally single trace interaction in chapter 2. To demonstrate that the tensor models with the tetrahedral interaction term have the same large N behavior as the corresponding SYK model, we will briefly sketch the computation of the two point function for the rank three, $q = 4$ tensor model with the following action [3],

$$S = \int dt \, \frac{i}{2}\psi^{abc}\partial_t\psi^{abc} + \frac{g}{4}\psi^{abc}\psi^{ab'c'}\psi^{a'bc'}\psi^{a'b'c}. \tag{1.2.4}$$

Since the melonic diagrams dominate, these are the only diagrams we consider when we consider the full two point function, see figure 1.5. We first write the bare propagator,

$$\left\langle T\left(\psi^{abc}(t)\psi^{a'b'c'}(0)\right)\right\rangle_0 = \delta^{aa'}\delta^{bb'}\delta^{cc'}G_0(t), \tag{1.2.5}$$

where $G_0(t) = \text{sign}(t)/2$. We can express the Schwinger Dyson equation for the two point function, which results from the summation of all melonic diagrams:

$$G(t-t') = G_0(t-t') + g^2N^3\int dt_1\, dt_2\, G_0(t-t_1)G(t_1-t_2)^3G(t_2-t'). \tag{1.2.6}$$

By taking the Fourier transform of (1.2.6), we have the following expression of $G(w)$,

$$G(w) = \left(-i\omega - \Sigma(\omega)\right)^{-1}, \qquad \Sigma(t) = g^2N^3G(t)^3. \tag{1.2.7}$$

We assume that in the IR, the Σ will dominate the derivative term and we make the following conformal ansatz,

$$G(t) = \frac{a\,\text{sign}(t)}{|t|^{2\Delta}}, \qquad \Sigma(t) = g^2N^3\frac{a^3\,\text{sign}(t)}{|t|^{6\Delta}}. \tag{1.2.8}$$

Taking the Fourier transform of (1.2.8), we have the following expressions,

$$\begin{aligned} G(\omega) &= 2^{1-2\Delta} i\sqrt{\pi}\frac{\Gamma(1-\Delta)}{\Gamma(1/2+\Delta)} a|\omega|^{2\Delta-1}\text{sign}(\omega), \\ \Sigma(\omega) &= 2^{1-6\Delta} i\sqrt{\pi}\frac{\Gamma(1-3\Delta)}{\Gamma(1/2+3\Delta)} a^3\text{sign}(\omega) g^2 N^3 |\omega|^{6\Delta-1}. \end{aligned} \tag{1.2.9}$$

Using that $G(\omega) = -1/\Sigma(\omega)$ in the IR limit,

$$-1 = G(\omega)\Sigma(\omega) = -2^{2-8\Delta} a^4 g^2 N^3 \pi \frac{\Gamma(1-\Delta)\Gamma(1-3\Delta)}{\Gamma(1/2+\Delta)\Gamma(1/2+3\Delta)} |\omega|^{8\Delta-2}, \tag{1.2.10}$$

where,

$$a^4 = \frac{\Gamma(\frac{1}{2}+\Delta)\Gamma(\frac{3}{2}-\Delta)}{\pi g^2 N^3 \Gamma(1-\Delta)\Gamma(\Delta)}. \tag{1.2.11}$$

We find that $\Delta = 1/4$, and we can now substitute these values into our ansatz to solve for the propagator,

$$\begin{aligned} G(t) &= \left(\frac{\Gamma(\frac{1}{2}+\Delta)\Gamma(\frac{3}{2}-\Delta)}{\pi g^2 N^3 \Gamma(1-\Delta)\Gamma(\Delta)}\right)^{1/4} \frac{\text{sign}(t)}{|t|^{2\Delta}} \\ &= \left(\frac{1}{4\pi g^2 N^3}\right)^{1/4} \frac{\text{sign}(t)}{|t|^{1/2}}. \end{aligned} \tag{1.2.12}$$

We show in section 1.2.2 that equation (1.2.12) matches that of the $q = 4$ SYK model at large N. The spectrum of bilinear operators of this model is explored in [3], and a key result is that the scaling dimensions have a solution that is responsible for quantum chaos in the model and is the mode dual to gravity, as is the case in the SYK model.

Figure 1.5: We must sum all melonic contributions to find the full two point function. On the far left is the bare propagator, and the others are examples of contributing melonic diagrams.

1.2.2 SYK model

The SYK model is a model describing N Majorana fermions, with a small number, q, of random interactions at a time. The Hamiltonian of the model is as follows [4, 34]:

$$H = \left(\frac{i^{q/2}}{q!}\right) \sum_{1 \leq j_1 < \ldots < j_q < N} J_{j_1 \ldots j_q} \psi_{j_1} \psi_{j_2} \ldots \psi_{j_q}, \text{ where } \{\psi_j, \psi_k\} = \delta_{jk}. \tag{1.2.13}$$

Here j is a mean zero random gaussian variable that has variance,

$$\langle J^2_{j_1 \ldots j_q} \rangle = \frac{J^2 (q-1)!}{N^{q-1}}. \tag{1.2.14}$$

The model (1.2.13) defines a quantum mechanical system that shares some properties with a two-dimensional black hole in AdS. Namely, when we solve the model at large N in the $1/N$ expansion, the correlation functions of this model agree with those of a two-dimensional black hole. The $1/N$ expansion allows us to pick out and evaluate the dominant Feynman diagrams at large N, just like in the tensor model.

The melonic diagrams dominate for this model at large N. Let us define a face as a cycle made of alternating propagator and disorder lines. Each face contributes a factor of N, and each disorder line contributes a factor of $N^{-(q-1)}$. Thus, the melonic diagrams maximize the number of faces for a given number of vertices. Examples of

Figure 1.6: Examples of the melonic contributions to the full two point function of the SYK model. The dotted lines represent the average over disorder.

melonic contributions to the SYK two point function are presented in figure 1.6, and a detailed diagrammatic proof of melonic dominance is presented in [35].

Here we show that the full two point function of the $q = 4$ SYK model and is equal to (1.2.12). First, let us write the $q = 4$ SYK Hamiltonian,

$$H = -\frac{1}{12} \sum_{1 \leq i < j < k < l < N} J_{ijkl}\, \psi_i \psi_j \psi_k \psi_l, \text{ with } \langle J_{ijkl}^2 \rangle = \frac{6J^2}{N^3}. \tag{1.2.15}$$

The Schwinger Dyson equations match those of the $q = 4$ tensor model presented in section 1.2.1,

$$G(\omega) = \left(-i\omega - \Sigma(\omega)\right)^{-1}, \qquad \Sigma(t) = J^2 G(t)^3. \tag{1.2.16}$$

Thus, the resulting two point function of the SYK model matches that of the tensor model with $J^2 = g^2 N^3$. We explore more properties of the SYK model in chapters 2 and 3; in particular, we study the chaos properties as well as higher q computations in comparison to the corresponding tensor model.

1.2.3 Complex SYK model

The tensor models and the SYK model may both be generalized to include complex fermions. In chapter 3, we study a 'prismatic' complex tensor model (rank three, $q = 6$) along with its analogous $q = 6$ disordered model, which we call the $q = 6$ WL-

SYK model, due to the Wishart Laguerre (WL) coupling we find. In this section, we first introduce the complex SYK (cSYK) model by adding a global $U(1)$ symmetry, in addition to a chemical potential, to the standard SYK model, and we discuss a few key findings in the $q = 4$ cSYK model.

We start by writing the cSYK Hamiltonian [36],

$$H = \sum_{\substack{j_1<\ldots<j_{q/2} \\ k_1<\ldots<k_{q/2}}} J_{j_1<\ldots<j_{q/2},k_1<\ldots<k_{q/2}} \mathcal{A}\{\psi^\dagger_{j_1} \ldots \psi^\dagger_{j_{q/2}} \psi_{k_1} \ldots \psi_{k_{q/2}}\}, \tag{1.2.17}$$

where $\mathcal{A}\{\ldots\}$ is equal to the antisymmetrized product of the Majorana fermions. The antisymmetrization preserves the particle hole symmetry of the model, meaning this model is invariant under $\psi^\dagger_j \leftrightarrow \psi_j$. The variance of the random coupling $J_{j_1<\ldots<j_{q/2},k_1<\ldots<k_{q/2}}$ is given by,

$$\left\langle \left| J_{j_1<\ldots<j_{q/2},k_1<\ldots<k_{q/2}} \right|^2 \right\rangle = J^2 \frac{(q/2)!(q/2-1)!}{N^{q-1}}. \tag{1.2.18}$$

We will focus on the model with $q = 4$ with the following Hamiltonian is,

$$\begin{aligned} H &= \sum_{j_1<j_2,k_1<k_2} J_{j_1j_2k_1k_2} \frac{1}{2}\{\psi^\dagger_{j_1}\psi^\dagger_{j_2}, \psi_{k_1}\psi_{k_2}\} \\ &= \sum_{j_1<j_2,k_1<k_2} J_{j_1j_2k_1k_2} \left(\frac{1}{2}\psi^\dagger_{j_1}\psi^\dagger_{j_2}\psi_{k_1}\psi_{k_2} + \frac{1}{2}\psi_{k_1}\psi_{k_2}\psi^\dagger_{j_1}\psi^\dagger_{j_2} \right) \\ &= \sum_{j_1<j_2,k_1<k_2} J_{j_1j_2k_1k_2} \left(\psi^\dagger_{j_1}\psi^\dagger_{j_2}\psi_{k_1}\psi_{k_2} + B_{j_ij_2k_1k_2} \right), \end{aligned} \tag{1.2.19}$$

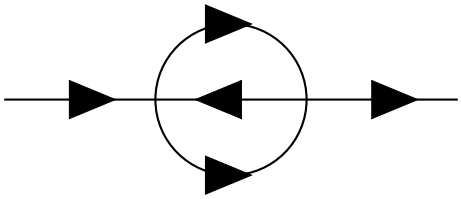

Figure 1.7: This is an example of a melonic contribution to the two point function of the $q = 4$ complex SYK model as defined in (1.2.19).

and the $B_{j_i j_2 k_1 k_2}$ term arises from normal ordering the terms in the second line of equation (1.2.19) using the relations $\{\psi_i, \psi_j\} = 0$ and $\{\psi_i^\dagger, \psi_j\} = \delta_{ij}$:

$$\begin{aligned} &B_{j_i j_2 k_1 k_2} \\ &= \frac{1}{2}\left(\delta_{j_1 k_1}\psi^\dagger_{j_2}\psi_{k_2} + \delta_{j_2 k_2}\psi^\dagger_{j_1}\psi_{k_1} - \delta_{j_1 k_2}\psi^\dagger_{j_2}\psi_{k_1} - \delta_{j_2 k_1}\psi^\dagger_{j_1}\psi_{k_2} + \delta_{j_1 k_2}\delta_{j_2 k_1} - \delta_{j_1 k_1}\delta_{j_2 k_2}\right). \end{aligned} \tag{1.2.20}$$

The global $U(1)$ charge Q is defined as follows,

$$Q = \sum_i \frac{1}{2}\left[\psi_i^\dagger, \psi_i\right] = \psi_i^\dagger\psi_i - \frac{N}{2}. \tag{1.2.21}$$

We write the Schwinger Dyson equations for this theory by noting that the melonic diagrams are again the only contributing diagrams at large N. An example of one of these contributing melonic diagrams is provided in figure 1.7. The Schwinger Dyson equations are,

$$G(t) = \left(\partial_t - \mu - \Sigma(t)\right)^{-1}, \qquad \Sigma(t) = J^2 G(t)^2\left(-G(-t)\right). \tag{1.2.22}$$

These equations differ not only by the form of Σ, but also by the form of the bare propagator, as now we consider the addition of the chemical potential μ. However, in the IR, we can simplify and neglect the bare propagator term, $G_0(t) = -(\partial_t - \mu)^{-1}$. Since the global $U(1)$ symmetry breaks down to a local $U(1)$ symmetry in the IR, we must add a complex phase factor to our ansatz for the IR solution of the two point function. The full two point function in the IR is reported in [36] as,

$$\begin{aligned} G(\pm t) &= \frac{\mp b^{\Delta} e^{\pm \pi \mathcal{E}}}{|t|^{2\Delta}}, \qquad \Sigma(\pm t) = \frac{\mp b^{1-\Delta} e^{\pm \pi \mathcal{E}}}{|t|^{2(1-\Delta)}}, \\ \text{where} \quad b &= \frac{(1-2\Delta)\sin(2\pi\Delta)}{4\pi \cos(\pi\Delta + i\pi\mathcal{E})\cos(\pi\Delta - i\pi\mathcal{E})}, \end{aligned} \tag{1.2.23}$$

where $\mathcal{E}$ is known as the spectral asymmetry, which is a key feature of the complex SYK model. Another interesting feature of the cSYK model that we may examine is the charge compressibility, K. This quantity may be found numerically through quadratically fitting the ground state energy in each charge sector, $E_0(Q)$, versus the charge sector, Q, using the equation $E_0(Q) = E_0 + Q^2(2NK)^{-1}$. For the $q = 4$ cSYK model, the compressibility is found to be a small positive value, $K \approx 1.04$ [36]. We examine several other properties, including the charge compressibility, of our $q = 6$ WL-SYK model in chapter 3. Interestingly, we find that our model has a negative charge compressibility.

1.3 Quantum Chaos

Random matrices and chaotic systems are topics studied in a wide variety of fields including biology, finance, number theory, and physics; in fact, much progress in the

field was made by Eugene Wigner with applications in nuclear physics [37]. We can better understand several properties of our system using knowledge from random matrix theory. Namely, by studying the symmetries of our model, we can determine the corresponding so called 'Dyson ensemble,' and then we may make several generalizations of our model at large N stemming from the expected eigenvalue statistics.

There are three main random matrix ensembles corresponding to the Hermitian models that we study in this paper; these are commonly known as the Wigner ensembles consisting of the Gaussian Orthogonal Ensemble (GOE), the Gaussian Unitary Ensemble (GUE), and the Gaussian Symplectic Ensemble (GSE). The GOE is time reversal invariant and is a random real symmetric matrix ($H = H^T$) where the entries are drawn from a normal Gaussian distribution. The GUE is not time reversal invariant and is a random Hermitian matrix ($H = H^\dagger$) where the entries are drawn from a complex Gaussian distribution. Finally, the GSE is time reversal invariant (but breaks rotational symmetry) and is comprised of real quaternion matrices, meaning that the coefficients c_i are real in the following general form of the 2×2 complex matrix,

$$M = c_0 E_0 + c_1 E_1 + c_2 E_2 + c_3 E_3, \text{ where}$$
$$E_0 = \begin{bmatrix} 1 & 0 \\ 0 & 1 \end{bmatrix}, E_1 = \begin{bmatrix} 0 & i \\ i & 0 \end{bmatrix}, E_2 = \begin{bmatrix} 0 & -1 \\ 1 & 0 \end{bmatrix}, E_3 = \begin{bmatrix} i & 0 \\ 0 & -i \end{bmatrix}. \tag{1.3.1}$$

We can construct the GSE by imposing the symmetry condition $M^*_{ij} = M_{ji}$, leading to real diagonal entries for M, and by summing the direct products between matrices with entries drawn from a normal Gaussian distribution and the above E_i matrices.

1.3.1 Level spacings distribution

Here, we sketch the derivation of the probability density function (pdf) of the spacing between the eigenvalues of a simple 2×2 GOE, following the calculations presented in [38]. We first define a simple GOE matrix,

$$H = \begin{bmatrix} a & b \\ b & c \end{bmatrix}. \tag{1.3.2}$$

where a and c are sampled from $\mathcal{N}(0,1)$ and b is sampled from $\mathcal{N}(0,\frac{1}{2})$; here, we let $\mathcal{N}(\mu,\sigma^2)$ represent the normal distribution with mean μ and variance σ^2. We can solve for the eigenvalues of H through the characteristic equation, $(a-\lambda)(c-\lambda)-b^2=0$ to get that $2\lambda_{1,2} = a+c \pm \sqrt{(a-c)^2+4b^2}$. Thus, the spacing between the eigenvalues is $s = \lambda_1 - \lambda_2 = \sqrt{(a-c)^2+4b^2}$. Now we can write the pdf of the spacing as follows,

$$P(s) = \int_{-\infty}^{\infty} da\, db\, dc \frac{e^{\frac{-a^2}{2}}}{\sqrt{2\pi}} \frac{e^{\frac{-c^2}{2}}}{\sqrt{2\pi}} \frac{e^{-b^2}}{\sqrt{\pi}} \delta(s - \sqrt{(a-c)^2+4b^2}), \tag{1.3.3}$$

since our variables are drawn from a normal distribution. To simplify the calculations, we change variables using the substitutions $a = (r\cos(\theta)+\phi)/2$, $c = (\phi - r\cos(\theta))/2$, and $b = (r\sin(\theta))/2$,

$$\begin{aligned} P(s) &= \frac{1}{2\pi^{3/2}} \int_0^{\infty} dr \int_0^{2\pi} d\theta \int_{-\infty}^{\infty} d\phi \left|\frac{-r}{4}\right| e^{(-r^2\cos^2\theta+\phi^2)/4} e^{(-r^2\sin^2\theta)/4} \\ &= \frac{1}{4\pi^{1/2}} \int_0^{\infty} dr \int_{-\infty}^{\infty} d\phi\, r\, \delta(r-s) e^{-(r^2+\phi^2)/4} \\ &= \frac{1}{4\pi^{1/2}} 2\sqrt{\pi}\, s\, e^{-s^2/4} = \frac{s}{2} e^{-s^2/4}. \end{aligned} \tag{1.3.4}$$

We can rescale this expression by the mean level spacing, $\bar{s} = \sqrt{\pi}$, to get

$$\hat{P}(s) = \sqrt{\pi} P(\sqrt{\pi} s) = (\pi s/2) e^{-\pi s^2/4}. \tag{1.3.5}$$

Equation (1.3.5) is known as Wigner's surmise, and furthermore, Wigner derived an approximation for $\hat{P}(s)$ that can be used at large N [38–40],

$$\hat{P}_W(\beta, s) = A\, s^{\beta} e^{-B\, s^2/2}, \tag{1.3.6}$$

where A and B are normalization constants, and $\beta = 1, 2$ and 4 corresponds to the pdf of the eigenvalue spacings of the GOE, the GUE, and the GSE respectively.

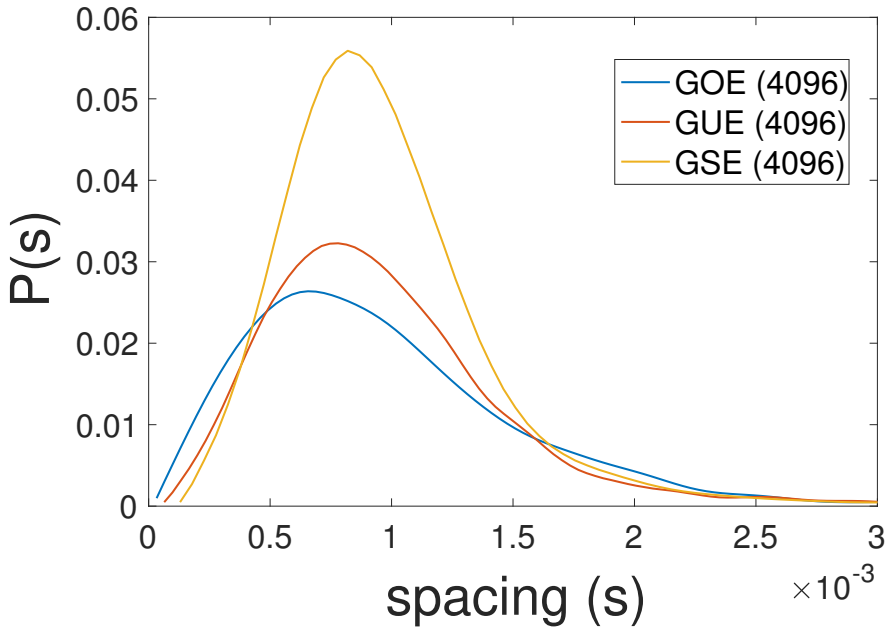

Figure 1.8: The level spacings, or 'unfolded,' plots for the GOE, GUE, and GSE with 2^{12} distinct eigenvalues.

Let us note here that as we send $s \to 0$, the $P(s)$ also falls towards 0, see figure 1.8. In other words, the probability of two eigenvalues having near identical values is extremely small. This phenomenon is known as level repulsion, and is a property of random matrices. This is in contrast to the spacings pdf of i.i.d. real random variables, which display Poisson statistics; thus as $s \to 0$, the probability of s grows large. We can plot the $P(s)$ of our models and observe how the distribution compares to what we expect from the corresponding Winger ensemble. This plot gives us information about the correlation functions of close eigenvalues.

1.3.2 Spectral form factor

We can gain information about the longer range correlations of eigenvalues by examining the spectral form factor (SFF),

$$g(t, \beta) = |Tr(e^{-\beta H - iHt})|^2 / Tr(e^{-\beta H})^2. \tag{1.3.7}$$

The main elements of the SFF for a random matrix is a dip ramp plateau structure. The ramp is caused by the repulsion of eigenvalues that are far apart; these eigenvalues are anti-correlated, which is why the ramp is below the plateau. One can think of the eigenvalue spectrum as comprising a crystal, and the ramp and plateau are a measure of the rigidity or 'floppiness' of the crystalline structure.

The plateau is a result of generic level repulsion, as degeneracies are unlikely. The ramp and plateau occur at later times and thus probe shorter distances—they are a result of a phenomena known as spectral rigidity. The ramp and plateau behavior are

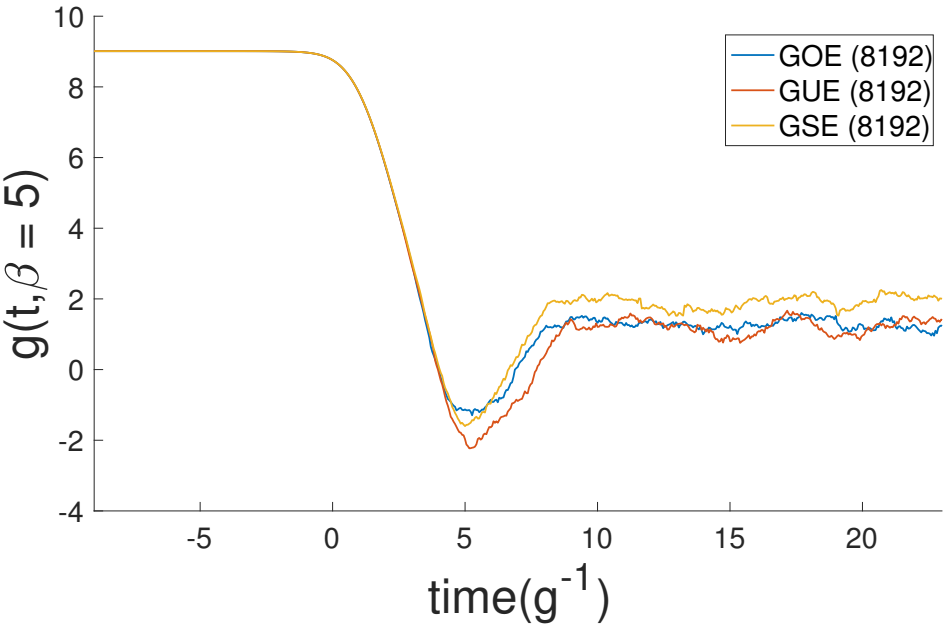

Figure 1.9: The SFF for the GOE, GUE, and GSE, all of size 2^{13}, display the dip ramp plateau structure with slight differences in depth and shape of the dip, the ramp slope, and sharpness of the ramp to plateau transition.

universal features of chaotic systems, and emerge from the realization that near the center of the semi-circle of eigenvalue density, the pair correlation function is expressed as the square of the sine kernel. By Fourier transforming the pair correlation function of the eigenvalue density for the random matrix, we can see that $g(t, 0)$ has a ramp up to what is known as the plateau time t_p, and a constant value after t_p. This derivation can be found in [22]. The time that the ramp starts is known as the 'Thouless time.' Like the scrambling time, it is of order $\log N$ but it has a different prefactor [41, 42]. This Thouless time gives the time scale for energy to diffuse across the system. The dip occurs at early times and so it probes larger distances; it is the Fourier transform

of the entire spectrum. For a random matrix that follows the Winger-Dyson semicircle distribution, the slope of the dip resembles the Bessel function, and this is what we see when we plot its SFF. A chaotic system is expected to have these properties since they share the same nearest-neighbor statistics of the respective RMT ensemble, see figure 1.9.

1.3.3 Level spacings ratio

Another measure of quantum chaos we study is closely related to the level spacings discussed earlier, and is called the consecutive level spacings ratio mean value, $\langle r \rangle$. This quantity is often used when examining transitions in spectral statistics [43]. The ratio, r is equal to,

$$r = \frac{s_i}{s_i - 1}, \text{ where } s_i = \lambda_{i+1} - \lambda_i. \tag{1.3.8}$$

Here, λ_i is the i^{th} eigenvalue. Starting from the Gaussian ensemble joint probability distribution of three consecutive eigenvalues, [40] derives the analog of the Wigner surmise for the probability distribution of the consecutive level spacings ratio, $P_W(\beta, r)$:

$$P_W(\beta, r) = A_\beta \frac{(r + r^2)^\beta}{(1 + r + r^2)^{1+\frac{3\beta}{2}}}, \tag{1.3.9}$$

where A_β is a normalization constant, and $\beta = 1, 2$, and 4 corresponds to the GOE, GUE, and GSE respectively. Note that we see level repulsion here; when we allow $r \to 0$, the probability of the ratio $P(r)$ also approaches a small value. We can now restrict the values of r to have support $[0, 1]$, and we call this new value $\hat{r}$. To compute $\langle \hat{r} \rangle$, we use the fact that $P_W(\beta, \hat{r}) = 2\, P_W(\beta, r)\theta(1 - r)$ as in [40]. We can now find

the analytical expressions for $\langle \hat{r} \rangle$,

$$\langle \hat{r} \rangle_\beta = \int_0^\infty dr\, 2\, A_\beta\, \theta(1-r)\, \frac{r\,(r+r^2)}{(1+r+r^2)^{1+\frac{3\beta}{2}}}. \tag{1.3.10}$$

The values of A_β used are computed in [40], and are equal to $4/27$, $81\sqrt{3}/(4\pi)$, and $729\sqrt{3}/(4\pi)$ for $\beta = 1, 2$, and 4. We find that $\langle \hat{r} \rangle_1 = 4 - 2\sqrt{3} \approx 0.5359$, $\langle \hat{r} \rangle_2 = 2\sqrt{3}/\pi - 1/2 \approx 0.6027$, and $\langle \hat{r} \rangle_4 = 32\sqrt{3}/(15\pi) - 1/2 \approx 0.6762$ for the GOE, GUE, and GSE respectively. We compare to these reference values throughout this work.

1.4 Overview

I thank Igor Klebanov, Kiryl Pakrouski, Fedor Popov, and Wenli Zhao for their valuable collaboration on much of the work presented in this thesis.

Chapter 2 is based largely on work done with Igor Klebanov and Fedor Popov in [44]. I presented this work as a poster in the Strings 2019 conference [45]. We introduce the higher order generalization of the tensor model. We examine the growing number of $O(N)^{q-1}$ invariant tensor interactions for $q > 6$, noting that the maximally single-trace interaction is no longer unique. We review symmetries of the rank five, $q = 6$ model, and examine the spectral properties and compare to those of the corresponding $q = 6$ SYK model. We study the SFF of our models as well as the large N scaling dimensions of the fermion bilinears.

Chapter 3 is based on work in progress done with Simone Giombi, Igor Klebanov, and Wenli Zhao [46]. We introduce the complex fermionic prismatic tensor model,

and consider $U(1)$ preserving interactions. We study the properties of these models, namely the large N scaling dimensions of the bilinears. Finally, we consider the (complex) disordered analog of this model, and note that this model differs from [36] by a broken charge conjugation symmetry and what could be interpreted as a negative charge compressibility.

Chapter 4 is based on work done with Igor Klebanov, Kiryl Pakrouski, and Fedor Popov in [47] and [48]. In this chapter, we focus on models containing scar states, and develop a general framework for construction. We find that many body scar states comprise a group invariant sector of the Hilbert space. These scar states are useful for preserving information of a system over time, and can be realized experimentally. We construct scars in models of varying dimensionality (vector and matrix models), and we also show that several well known scar states can be written via our framework of construction. We support our results numerically with several quantifications of quantum chaos in addition to ETH violation computations and visualizations.

Chapter 2

Majorana fermion quantum mechanics for higher rank tensors

2.1 Introduction and summary

This chapter is based on [44]. We study the Klebanov-Tarnopolsky tensor model that is generalized to higher rank. Rank $q-1$ tensor models with $q>4$ have been the subject of several studies relevant to our paper [3, 49–51]. A comprehensive study of various invariant interaction vertices for a single tensor of rank $q-1$ was carried out in [50, 51]. For $q \geq 8$ there is a very rapidly growing number of 'generalized tetrahedral' interaction vertices, i.e. those that satisfy the constraint that every pair of tensors has exactly one index contraction.[a] As pointed out in [49], their counting is a mathematical problem isomorphic to scheduling of the round-robin tournament.

[a] This is to be contrasted with the Gurau-Witten model [2,5] for q flavors of rank $q-1$ Majorana fermion tensors, where the interaction is uniquely fixed by the $O(N)^{q(q-1)/2}$ symmetry.

Following [50] we mostly focus on the special subclass of such interactions which are 'maximally single-trace' — their stranded diagrams stay connected if all but two of the colors are erased. This facilitates the combinatorial analysis of the Feynman diagrams in the large N limit. It is conjectured that the maximally single-trace (MST) interaction vertices, which are known in mathematical literature as perfect 1-factorizations, exist for any even $q > 2$. They have been proven to exist when either $q-1$ or $q/2$ is prime [52, 53], as well as in some other cases, such as $q = 16, 28, 36, 40, 50, 126, 170$, etc.

A part of our paper is devoted to a careful analysis of the Majorana tensor theory in $0+1$ dimension with rank-5 tensors as the dynamical degrees of freedom. The unique generalized tetrahedral interaction was written down in [3], and the Hermitian Hamiltonian is

$$H_6 = i\frac{g}{2}\big(\psi^{a_1b_1c_1d_1e_1}\psi^{a_1b_2c_2d_2e_2}\psi^{a_2b_2c_3d_3e_1}\psi^{a_2b_3c_2d_1e_3}\psi^{a_3b_3c_1d_3e_2}\psi^{a_3b_1c_3d_2e_3} - \psi^{a_3b_1c_3d_2e_3}\psi^{a_3b_3c_1d_3e_2}\psi^{a_2b_3c_2d_1e_3}\psi^{a_2b_2c_3d_3e_1}\psi^{a_1b_2c_2d_2e_2}\psi^{a_1b_1c_1d_1e_1}\big)\ . \tag{2.1.1}$$

We can graphically depict this interaction by representing each fermion as a vertex of a graph, and each index contraction between pairs of fermions as an edge connecting two vertices (see figure 2.1). In the large N limit, where $\lambda^2 = g^2N^{10}$ is held fixed, the melonic diagrams dominate. The factor of i is necessary to make H_6 real; it is a new feature compared to the rank-3 Hamiltonian (1.2.1). The Hamiltonian (2.1.1) has $SO(N)^5$ symmetry, as well as some discrete symmetries. Some aspects of this tensor model are similar to the $O(N)^3$ tensor model. The energy spectra in both models are symmetric under $E \to -E$, since an interchange of any two of the $O(N)$ groups

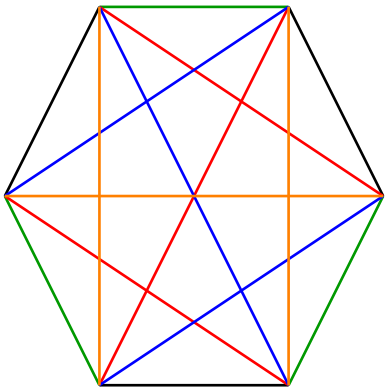

Figure 2.1: A graphical representation of the unique 'generalized tetrahedral' interaction for $q = 6$, given in (2.1.1). Each line represents an index contraction, while different colors correspond to different groups. This interaction is maximally single-trace, since erasing any set of three colors leaves the diagram connected.

sends $H \to -H$. However, there are also some differences: for example, in the $O(N)^5$ model the time-reversal is not a symmetry since it acts as $\mathcal{T}^{-1} H \mathcal{T} = -H$ due to the factor i present in the Hamiltonian (2.1.1).

The $O(N)^5$ model also has some differences from the $q = 6$ SYK model. In particular, at small N the structure of the spectra are rather different. This is due to the large number of continuous and discrete symmetries, which makes the tensor spectrum highly degenerate. The $q = 6$ SYK spectrum is compared with the corresponding Q-hermite polynomial, which is calculated in the double scaling limit, where $N_{\text{SYK}} \to \infty$, $q \to \infty$ with q^2/N_{SYK} held fixed [22, 54]. We find very good agreement, which suggests that the $q = 6$ SYK model shares some spectral properties with the double scaled model.

The structure of the paper is as follows. In section 2.2 we discuss the structure of the Hamiltonian (2.1.1) and its symmetries and use them to explain some of the

degeneracies that we observe in the singlet spectrum in section 2.3. In section 2.4 we numerically study the spectrum of the tensor model and the $q = 6$ SYK model and investigate the differences between the spectral properties at finite N. In section 2.5 we discuss some properties of higher q tensor models. The Schwinger-Dyson equations of the $O(N)^5$ and $O(N)^7$ models are computed in section 2.6. We show the existence of the solution of these equations in the IR limit, and that it is invariant under conformal transformations. Additionally, we study the spectrum of the singlet bilinear and some of the non-singlet bilinears and show that they are identical to the SYK model.

2.2 Hamiltonian and its symmetries

The model contains a set of N^5 Majorana fermions ψ^{abcde} with the anti-commutation relations:

$$\{\psi^{abcde}, \psi^{a'b'c'd'e'}\} = \delta^{aa'}\delta^{bb'}\delta^{cc'}\delta^{dd'}\delta^{ee'} \ . \tag{2.2.1}$$

We will first work at the 'classical level,' where we ignore the delta-function terms on the RHS of (2.2.1) and treat the fermions as real grassman numbers. Then the Hamiltonian we consider is

$$H_{\text{class}} = ig\psi^{a_1b_1c_1d_1e_1}\psi^{a_1b_2c_2d_2e_2}\psi^{a_2b_2c_3d_3e_1}\psi^{a_2b_3c_2d_1e_3}\psi^{a_3b_3c_1d_3e_2}\psi^{a_3b_1c_3d_2e_3} \ . \tag{2.2.2}$$

This is the unique sextic term with $O(N)^5$ symmetry where any pair of fields have one index contraction [3]. The factor i is inserted so that the Hamiltonian is Hermitian. The correct quantum Hamiltonian (2.1.1) is $H_6 = H_{\text{class}} + H_{\text{class}}^\dagger$.

We can show that H_{class} changes sign under permutation of two $O(N)$ groups. For example, when we permute $O(N)_c$ and $O(N)_d$, the fermions transform as

$$\psi^{abcde} \leftrightarrow \psi^{abdce}. \tag{2.2.3}$$

So, $H_{\text{class}} \to H'_{\text{class}}$ where

$$H'_{\text{class}} = ig\psi^{a_1b_1c_1d_1e_1}\psi^{a_1b_2c_2d_2e_2}\psi^{a_2b_2c_3d_3e_1}\psi^{a_2b_3c_1d_2e_3}\psi^{a_3b_3c_3d_1e_2}\psi^{a_3b_1c_2d_3e_3} \ . \tag{2.2.4}$$

Dropping the quantum delta-function terms in (2.2.1), and bringing it to the form so that the fields are read from right to left, we have

$$H'_{\text{class}} = -ig\psi^{a_3b_1c_2d_3e_3}\psi^{a_3b_3c_3d_1e_2}\psi^{a_2b_3c_1d_2e_3}\psi^{a_2b_2c_3d_3e_1}\psi^{a_1b_2c_2d_2e_2}\psi^{a_1b_1c_1d_1e_1} \ . \tag{2.2.5}$$

We find that $H'_{\text{class}} = -H_{\text{class}}$; this can be seen explicitly by relabeling the indices

$$\begin{aligned} &a_1 \leftrightarrow a_3, \quad e_1 \leftrightarrow e_3, \quad b_2 \leftrightarrow b_3, \\ &c_2 \to c_1, \quad c_1 \to c_3, \quad c_3 \to c_2, \\ &d_3 \to d_1, \quad d_1 \to d_2, \quad d_2 \to d_3. \end{aligned} \tag{2.2.6}$$

We examine the behavior under the other $O(N)$ permutations and find that $H' = -H$ in all cases, see table 2.1. Therefore, the symmetry group of the Hamiltonian includes

Group Permutation	Index relabeling
$O(N)_a$ and $O(N)_b$	$c_1 \leftrightarrow c_2, \quad e_1 \leftrightarrow e_3, \quad d_2 \leftrightarrow d_3,$ $a_1 \to a_2, \quad a_2 \to a_3, \quad a_3 \to a_1,$ $b_1 \to b_3, \quad b_3 \to b_2, \quad b_2 \to b_1.$
$O(N)_b$ and $O(N)_c$	$a_2 \leftrightarrow a_3, \quad b_1 \leftrightarrow b_2, \quad c_1 \leftrightarrow c_2,$ $d_1 \leftrightarrow d_2, \quad e_1 \leftrightarrow e_2.$
$O(N)_c$ and $O(N)_d$	$a_1 \leftrightarrow a_3, \quad e_1 \leftrightarrow e_3, \quad b_2 \leftrightarrow b_3,$ $c_2 \to c_1, \quad c_3 \to c_2, \quad c_1 \to c_3,$ $d_3 \to d_1, \quad d_1 \to d_2, \quad d_2 \to d_3.$
$O(N)_d$ and $O(N)_e$	$a_2 \leftrightarrow a_3, \quad b_1 \leftrightarrow b_2, \quad c_1 \leftrightarrow c_2,$ $d_1 \leftrightarrow d_2, \quad e_1 \leftrightarrow e_2.$

Table 2.1: Group permutations that send H to $-H$.

the alternating group A_5. This is related to the fact that it is a maximally single-trace (MST) operator. We expect that the A_{q-1} symmetry also holds for the MST Hamiltonians with higher even q.

When we use the quantum anti-commutation relations (2.2.1), the Hamiltonian (2.2.2) is not Hermitian. Adding the Hermitian conjugate, we find (2.1.1). It is then possible to check that under a permutation of two indices $H_6 \to -H_6$, establishing the A_5 symmetry at the quantum level. In the second term of H_6 we may bring the variables back into the same position as in the first term. To do this we need to make 15 permutations, which give rise to 15 additional quartic terms. Indeed, we can add possible quartic terms to the quantum Hamiltonian (2.1.1), but as it is shown in the section 2.7, they do not preserve the A_5 symmetry mentioned above. The Hamiltonian (2.1.1) can be also obtained via the path integral formulation of the model with real grassmanian variables, and by calculating the corresponding operator by Weyl ordering. Another way to see this is to notice that this is the only operator up to the sixth order in fermions that respects the A_5 symmetry.

We may choose the representation where each ψ^{abcde} is a Hermitian matrix with real entries. Thus, in a given basis (2.1.1) is a Hermitian matrix with imaginary entries; therefore, it is antisymmetric. This means that its eigenvalues are real and come in pairs $\pm E$. This implies that the spectrum has symmetry under $E \to -E$, which is a desired property. The proof is the following: let us start with some real matrix, H'. From H' we can construct a Hermitian matrix, $H = i(H' - H'^T)$. All entries of this matrix are complex, $H = -H^*$, and by definition, $H^\dagger = H$, where $H^\dagger$ is the adjoint. We can therefore conclude that $H^T = -H$. We write the characteristic equation:

$$\det(H - \lambda I) = 0 \Rightarrow \det(H^T - \lambda I) = \det(H + \lambda I) = 0 \tag{2.2.7}$$

Thus we have shown that the energy spectrum of (2.1.1) is symmetric. Another way to see this is to consider the time reversal symmetry, which we discuss in the following section.

2.2.1 Discrete symmetries

As in [18] we can introduce an operator that sends $H \to -H$. This is called the permutation operator, and it implements an $O(N)$ group pair swap. We can implement this operation by introducing the following operator

$$P_{45} = \prod_{a,b,c,d=e} \psi^{abcde} \prod_{a,b,c,d>e} \left(\frac{\psi^{abcde} + \psi^{abced}}{\sqrt{2}} \right), \quad P_{45}^\dagger \psi^{abcde} P_{45} = \psi^{abced}, \tag{2.2.8}$$

which exchanges the last two indices of each fermion in the interaction.

For convenience, it is better to work with Dirac fermions, which can be built in the following way

$$\psi^{abcdn} = \frac{\psi^{abcd(2n-1)} + i\psi^{abcd(2n)}}{\sqrt{2}}, \quad \bar{\psi}^{abcdn} = \frac{\psi^{abcd(2n-1)} - i\psi^{abcd(2n)}}{\sqrt{2}}, \tag{2.2.9}$$

and they satisfy the usual commutation relations of the Dirac fermions,

$$\left\{\psi_I, \bar{\psi}_J\right\} = \delta_{IJ}, \quad \{\psi_I, \psi_J\} = \left\{\bar{\psi}_I, \bar{\psi}_J\right\} = 0. \tag{2.2.10}$$

This formalism has manifest $O(N)^4 \times SU(N/2)$ symmetry, but does not manifest the original $O(N)^5$ symmetry. We can normal order each of these terms to get the following Hamiltonian plus several quartic terms which are not included here.

$$H_6 = ig\times$$
$$\Big[\psi^{ijklm}\psi^{iopqr}\psi^{ntplw}\bar{\psi}^{sjuqw}\bar{\psi}^{stkvr}\bar{\psi}^{nouvm} - \psi^{ijklm}\psi^{iopqr}\psi^{sjuqw}\bar{\psi}^{ntplw}\bar{\psi}^{stkvr}\bar{\psi}^{nouvm} +$$
$$+\psi^{nouvm}\psi^{iopqr}\psi^{sjuqw}\bar{\psi}^{ntplw}\bar{\psi}^{stkvr}\bar{\psi}^{ijklm} - \psi^{nouvm}\psi^{iopqr}\psi^{ntplw}\bar{\psi}^{sjuqw}\bar{\psi}^{stkvr}\bar{\psi}^{ijklm} +$$
$$+\psi^{ijklm}\psi^{stkvr}\psi^{sjuqw}\bar{\psi}^{ntplw}\bar{\psi}^{iopqr}\bar{\psi}^{nouvm} - \psi^{ijklm}\psi^{stkvr}\psi^{ntplw}\bar{\psi}^{sjuqw}\bar{\psi}^{iopqr}\bar{\psi}^{nouvm} +$$
$$+\psi^{nouvm}\psi^{stkvr}\psi^{ntplw}\bar{\psi}^{sjuqw}\bar{\psi}^{iopqr}\bar{\psi}^{ijklm} - \psi^{nouvm}\psi^{stkvr}\psi^{sjuqw}\bar{\psi}^{ntplw}\bar{\psi}^{iopqr}\bar{\psi}^{ijklm}\Big]$$

We notice a symmetry under the exchange of $\psi^{abcd(2n)} \to -\psi^{abcd(2n)}$ in Hamiltonian (2.1.1). It corresponds to the charge conjugation symmetry, C, $\bar{\psi}^{abcdn} \leftrightarrow \psi^{abcdn}$. Under this exchange, each term gains a negative sign during normal ordering, and this results in preservation of the original Hamiltonian: $CHC^{-1} = H$. We can define

the charge conjugation operator,

$$C = \prod_{abcdn} \psi^{abcd(2n-1)}. \tag{2.2.11}$$

In the case of the $q = 4$ tensor model [18] there is an anti-unitary time-reversal symmetry T, that acts in the following way

$$TiT^{-1} = -i, \quad T\psi^{abcde}T^{-1} = \psi^{abcde}, \quad TH_4T^{-1} = H_4.$$

In the case of the Hamiltonian (2.1.1) this is not a symmetry of the theory. Indeed,

$$TH_6T^{-1} = -H_6,$$

which shows that T is not a symmetry of the theory. From this one can see that the eigenvectors come in the pairs $(|E\rangle, T|E\rangle)$ with opposite energies. In the representation where ψ^{abcde} are real matrices and the Hamiltonian is a pure imaginary matrix, the action of T coincides with complex conjugation $T = K$. Let us consider an eigenstate $|E\rangle = c_i |e_i\rangle$, where $|e_i\rangle$ is a basis that we build with the use of the vacuum and the creation operators $\bar{\psi}^{abcde}$. Then

$$KH_{6,ij}K^{-1} = H^*_{6,ij} = -H_{6,ij}, \quad H_{6,ij}c_j = Ec_i \Rightarrow H^*_{6,ij}c^*_j = Ec^*_i, \quad H_{6,ij}c^*_j = -Ec^*_i. \tag{2.2.12}$$

From this one can notice that if the c_i are real then it corresponds to the zero state. Indeed,

$$\langle E|H|E\rangle = c_i H_{6,ij} c_j = -c_i H^*_{6,ij} c_j = 0. \tag{2.2.13}$$

To get a symmetry of the Hamiltonian out of the time reversal symmetry, we can combine it with the permutation operator P_{45} to get $T_{45} = TP_{45}$. This operator interchanges two representations of the A_5 group. The existence of such a symmetry explains the 6-fold degeneracy of ground state in the numerical studies of the $N = 2$ model. The symmetries A_5 together with T_{45} form the S_5 symmetry group.

With the discrete symmetries of our $q = 6$, $O(N)^5$ symmetric tensor model described above, we are now in a position to find the corresponding random matrix model to describe quantitative properties of the spectrum of the model. This is typically done by mapping our model to a random matrix theory ensemble. There are general rules for choosing the associated ensemble based on the various symmetries of the model [55]. The set of possible ensembles we consider is known as the Andreev-Altland-Zirnbaur (AAZ) ten-fold classification. The symmetries we will use to classify our model are the time reversal symmetry (TRS), and the permutation symmetry described above, P_{ij}. As noted above, our Hamiltonian does not posses TRS, like the $q = 6$ SYK model [4]. In the absence of TRS, we can take $P_{ij}^2 = +1$, and we can classify this Hamiltonian as belonging to the AIII ensemble of the AAZ ten-fold classification [56]. With this classification, we find that the corresponding random matrix ensemble is a chiral Gaussian Unitary Ensemble (chGUE) [57]. We may also use

our knowledge of these discrete symmetries to examine the singlet spectrum and its degeneracies, which is done in the following section.

2.3 The spectrum of eigenstates of the $O(2)^5$ model

In this section, we will study the spectrum of the Hamiltonian (2.1.1) for $N_i = 2$. The number of different Majorana fermions in this theory is 2^5, so that there are $2^{16} = 65536$ states. We can represent each fermion by a gamma matrix of $SO(32)$. We construct the pure real gamma matrices of $SO(32)$ by taking tensor products of Pauli spin matrices, as described in [58]. After substituting them into the Hamiltonian (2.1.1) we obtain a matrix which can be diagonalized using a computer program.

We begin by describing the $SO(N)^5$ invariant states in our theory. They are present only when N is even, and we restrict to this case. In order to count the number of these states, we follow the method of [18]. We gauge the free theory to get

$$\mathcal{S}_G = \int dt \left[\psi_{abcde}\partial_t\psi_{abcde} + A^1_{a_1a_2}\psi_{a_1bcde}\psi_{a_2bcde} + \ldots\right]. \tag{2.3.1}$$

The procedure of gauging eliminates all non-singlet states from the spectrum. Indeed, if we calculate the path integral on the circle of the length β and first take the integral over the gauge field we get a constraint $J^i_{ab} = 0$ — the generator of rotations must be equal to zero. After that, we take the integral over fermions to get,

$$\int [d\psi] \prod_{i=1}^{5} [dA^i] e^{i\mathcal{S}} = \mathrm{tr}_{\mathrm{sing}}\, 1 = N_{\mathrm{singlets}}. \tag{2.3.2}$$

If we first calculate the path integral over fermions and gauge the A^i to Cartan subalgebra, where A^i is a skew-symmetric matrix, we get that

$$N_{\text{singlets}} = 2^{15} \int \prod_{i=1}^{5} d\Omega^i_{SO(N)} \prod_{k_1=1,\ldots,k_5=1}^{N} \prod_{\pm} \cos\left[\frac{x^1_{k_1} \pm x^2_{k_2} \pm x^3_{k_3} \pm x^4_{k_4} \pm x^5_{k_5}}{2}\right]. \tag{2.3.3}$$

Here, $x^i_k, k = 1, \ldots, N/2$ and $d\Omega^i_{SO(N)}$ are coordinates and a Haar measure of the i^{th} group. The second product is taken for all possible combinations of the signs. Roughly speaking, the integrand is a character of $SO(N)^5$ and we can decompose it via the characters of the irreducible representations of the group to count the number of the representations. For the case $SO(2)^5$, the integral (2.3.3) gives 222 singlet states, agreeing with the numerical results. Using the same method, we may count the number of singlet states for models of different ranks. For instance, the $O(2)^4 \times O(4)$ model has 106096 singlets.

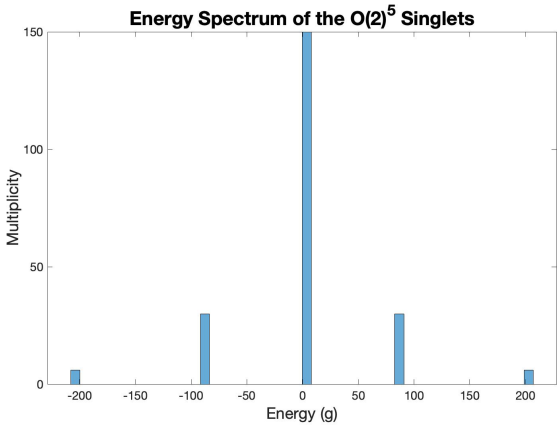

Energy	Count	Percent
$-64\sqrt{10} \approx -202.386$	6	2.70
$-64\sqrt{2} \approx -90.51$	30	13.51
0	150	67.57
$64\sqrt{2} \approx 90.51$	30	13.51
$64\sqrt{10} \approx 202.386$	6	2.70

Figure 2.2: The spectrum of the $SO(2)^5$ invariant states in the $O(2)^5$ tensor model.

We can see that the degeneracy of each state of the singlet spectrum for $N = 2$ is a multiple of six. The six-fold degeneracy is explained in section 2.2.1 by the discrete symmetry S_5. From the precise numerical eigenvalues we can deduce their exact analytic form: $64\sqrt{10} \approx 202.386$ and $64\sqrt{2} \approx 90.51$. Eigenvalues expressible in terms of square roots have appeared in other tensor models with low N [18–21].

Furthermore, from precise numerical results we have been able to infer the exact expressions for the full spectrum of the $O(2)^5$ tensor model. The energies are found to be roots of even polynomial equations up to order 6. This is presumably due to the fact that the various symmetries of H allow for mixing of at most six states. The polynomials have only even powers because they must be invariant under $E \to -E$, which follows from the fact that $H \to -H$ under exchange of any two colors. The results are displayed in figure 2.2. Most of the eigenvalues may be expressed in terms of square roots or nested square roots, which were seen in other tensor model spectra [18–21]. The remaining 18 energies are given by the roots of three distinct even sixth-order polynomials. One of the equations is

$$E^6 - 8704E^4 + 15794176E^2 - 3221225472 = 0 \ . \tag{2.3.4}$$

Degeneracy	Energy (in units of g)
6	$\pm 64\sqrt{10}$
30	$\pm 64\sqrt{2}$
32	$\pm 64\sqrt{42}$
80	$\pm 16\sqrt{18 \pm 6\sqrt{5}}$
80	$\pm 16\sqrt{2\left(5 \pm \sqrt{21}\right)}$
160	$\pm 32\sqrt{11}$
160	$\pm 16\sqrt{2\left(9 \pm \sqrt{57}\right)}$
160	$\pm 16\sqrt{13 \pm \sqrt{73}}$
160	$E^6 - 8704E^4 + 15794176E^2 - 3221225472 = 0$
160	$E^6 - 12800E^4 + 40960000E^2 - 805306368 = 0$
192	$E^6 - 20992E^4 + 53215232E^2 - 1275068416 = 0$
110	± 128
180	$\pm 64\sqrt{3}$
240	$\pm 32\sqrt{10}$
320	± 48
320	$\pm 16\sqrt{9 \pm \sqrt{73}}$
480	$\pm 75\sqrt{2}$
480	$\pm\sqrt{519 \pm 2\sqrt{37514}}$
808	$\pm 32\sqrt{6}$
860	± 64
992	$\pm 32\sqrt{3}$
1120	$\pm 16\sqrt{2}$
1208	$\pm 32\sqrt{2}$
1440	$\pm 16\sqrt{10}$
1600	± 16
3200	± 32
31772	0

Table 2.2: The exact spectrum of the $SO(2)^5$ tensor model. The expressions agree with the numerical results up to 11 digits past the decimal.

Its six solutions are given in terms of $\xi = \sqrt[3]{5023 + 324i\sqrt{533}}$ as follows:

$$E_{1,2} = \pm 16\sqrt{\frac{1}{3}\left(34 + \frac{433}{\xi} + \xi\right)} \approx \pm 79.1523$$
$$E_{3,4} = \pm\sqrt{\frac{8704}{3} - \frac{55424}{3\xi} + \frac{55424i}{\sqrt{3}\xi} - \frac{128}{3}\xi - \frac{128i}{\sqrt{3}}\xi} \approx \pm 46.9662,$$
$$E_{5,6} = \pm\sqrt{\frac{8704}{3} - \frac{55424}{3\xi} - \frac{55424i}{\sqrt{3}\xi} - \frac{128}{3}\xi + \frac{128i}{\sqrt{3}}\xi} \approx \pm 15.2673. \tag{2.3.5}$$

The roots of the other sixth-order polynomials may be expressed analogously. The total number of states listed in table 2.2 adds up to $65536 = 2^{16} = 2^{N^5/2}$, so it contains the full spectrum, which is shown in figure 2.3.

It is interesting to apply the Poincaré recurrence theorem to our system; the theorem states that after a finite amount of time, a state could return arbitrarily close to the the initial state [59]. The amount of time it takes for the state to return close to the initial state is known as the Poincaré recurrence time, and it is a quantity that we can compute. To find the recurrence time, we first consider an arbitrarily chosen initial state, which can be decomposed in terms of the eigenstates,

$$|\psi(t)\rangle = e^{-iHt}\,|\psi(0)\rangle = \sum_n e^{-iE_n t} c_n\,|\phi_n\rangle\,, \tag{2.3.6}$$

where $\sum_n |c_n|^2 = 1$, the $|\phi_n\rangle$ are the energy eigenstates, and we set $|\psi(0)\rangle = \sum_n c_n\,|\phi_n\rangle$. It follows that the distance between the initial state and the state at

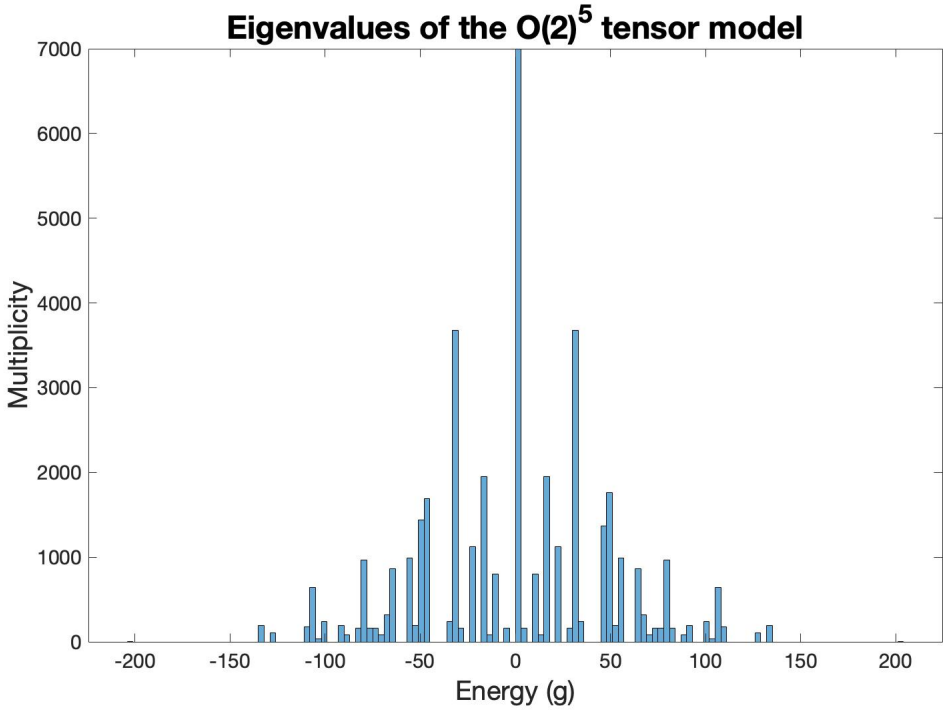

Figure 2.3: Energy spectrum of the $O(2)^5$ tensor interaction. There are 31772 zero energy states; not all are displayed.

time t is expressed as,

$$||\psi(t)\rangle - |\psi(0)\rangle|^2 = 2\sum_n |c_n|^2 \left(1 - \cos(E_n t)\right). \tag{2.3.7}$$

We can now define the recurrence time, t_{rec}, as the time at which $||\psi(t)\rangle - |\psi(0)\rangle| < \epsilon$ for any small $\epsilon > 0$. When this condition is met, we may conclude that the state $|\psi(t_{\text{rec}})\rangle$ is arbitrarily close to the initial state $|\psi\rangle$. The Poincaré recurrence theorem guarantees the existence of such a time, and here we sketch the proof of the existence following [60]. First we will split the sum on the RHS of equation (2.3.7) into two parts:

$$\sum_n |c_n|^2 \left(1 - \cos(E_n t)\right) = \sum_{n=0}^{m-1} |c_n|^2 \left(1 - \cos(E_n t)\right) + \sum_{n=m}^{\infty} |c_n|^2 \left(1 - \cos(E_n t)\right). \tag{2.3.8}$$

Let us first focus on the second term in equation (2.3.8). We note that

$$\sum_{n=m}^{\infty} |c_n|^2 \left(1 - \cos(E_n t)\right) \leq 2\sum_{n=m}^{\infty} |c_n|^2, \tag{2.3.9}$$

since the largest value the quantity $(1 - \cos(E_n t))$ can take on is 2. The sum on the RHS of equation (2.3.9) can be made arbitrarily small by making m larger. And thus, we can conclude that there exists some $\epsilon > 0$ such that,

$$\sum_{n=m}^{\infty} |c_n|^2 \left(1 - \cos(E_n t)\right) < \frac{\epsilon^2}{4}. \tag{2.3.10}$$

We now move on to examine the first term in equation (2.3.8). Using a result of the theory of almost-periodic functions, we may conclude that there exists a time t such that,

$$\sum_{n=0}^{m-1} |c_n|^2 \left(1 - \cos(E_n t)\right) < \frac{\epsilon^2}{4}. \tag{2.3.11}$$

By taking the sum of equation (2.3.11) and equation (2.3.10), we can conclude that there exists a t that satisfies,

$$||\psi(t)\rangle - |\psi(0)\rangle| < \epsilon. \tag{2.3.12}$$

Next we would like to find the recurrence time explicitly. Fortunately, if the exact expression for the energies E_n are known, the Lenstra-Lenstra-Lovász (LLL) lattice basis reduction algorithm may be used to calculate the recurrence time [61]. Namely, the condition (2.3.7) for the t_{rec} can be rewritten in the following form. We are looking for the number q_{rec}, such that

$$\max_n \left| E_n q - \lfloor E_n q \rceil \right| < \epsilon, \tag{2.3.13}$$

where the expression $\lfloor x \rceil$ rounds x to the nearest integer. The recurrence time can be expressed in terms of q as $t_{\text{rec}} = \frac{q}{2\pi}$. We can construct the lattice basis in the form

$$\begin{aligned} \vec{e}_1 &= \left(1, QE_1, QE_2, \ldots, QE_n\right), \\ \left(\vec{e}_i\right)_j &= \delta_{i,j}, \end{aligned} \tag{2.3.14}$$

and apply the LLL algorithm, so that the first basis vector has the form,

$$\vec{b}_1 = (q, Q\,(qE_1 - p_1)\,, Q\,(qE_2 - p_2)\,, \ldots)\,, \quad (qE_i - p_i) < Q^{-\frac{1}{n+1}}, \tag{2.3.15}$$

where p_i are integer numbers, and Q is a large integer chosen to adjust precision. Therefore, the number q found by the LLL algorithm is the required q for the condition (2.3.13).

Applying this algorithm for the spectrum of our model, we find that the recurrence time is

$$t_{\rm rec} = 2185162318761334375334098564981583801357944 28 g^{-1} \approx 2.18 * 10^{45} g^{-1}, \\ \left|1 - \left|\frac{Z(t_{\rm rec})}{Z(0)}\right|\right| < 0.5 * 10^{-2}. \tag{2.3.16}$$

2.4 Comparison with the $q = 6$ SYK model

In this section we calculate the energy spectrum and the spectral form factor of the $N_{\rm SYK} = 26$, $q = 6$ SYK model and compare with corresponding results of the $O(2)^5$ tensor model. The $q = 6$ SYK model Hamiltonian is

$$H_{\rm SYK} = i \sum_{1 \le i_1 < \ldots < i_6 < N_{\rm SYK}} j_{i_1 \ldots i_6} \psi_{i_1} \psi_{i_2} \ldots \psi_{i_6}, \quad \langle j_{i_1 \ldots i_6} j_{j_1 \ldots j_6} \rangle = J^2 \frac{\delta_{i_1 j_1} \ldots \delta_{i_6 j_6}}{N_{\rm SYK}^5}\ . \tag{2.4.1}$$

In this case there are $2^{13} = 8192$ states, and each fermion is assigned to a gamma matrix of $SO(26)$.

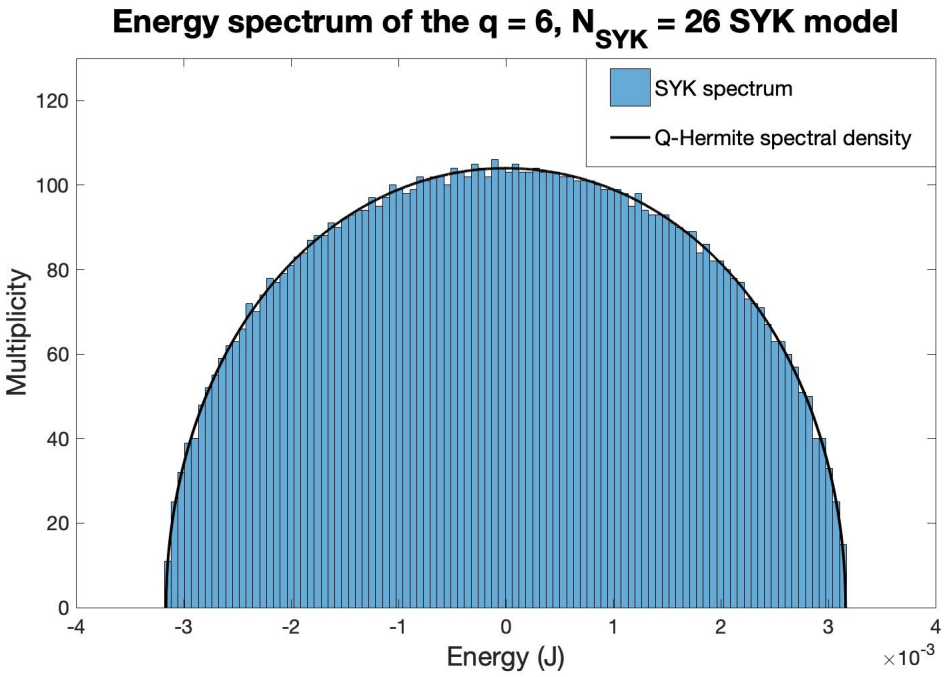

Figure 2.4: The energy spectrum of the $q = 6$ SYK model with $N_{\text{SYK}} = 26$, averaged over 49 samples.

In figure 2.3, we can see that there are large energy gaps in the tensor model, whereas the SYK model has a much denser spectrum and displays a near semi-circular distribution of eigenvalues that is characteristic of random matrices. Upon examining the energy spectrum, we can see the $E \to -E$ symmetry in the $q = 6$ model due to the time-reversal symmetry, which is not present in the $q = 4$ SYK model. We provide a fit for the energy spectrum as shown in figure 2.4. This fit is the spectral density that corresponds to the Q-Hermite polynomial with Q equal to a combinatorial factor, η, that encodes the suppression of crossing diagrams in the Wick contractions of gamma matrices. The suppression factor is derived in [62],

$$\eta = \binom{N_{\text{SYK}}}{q}^{-1} \sum_{p=0}^{q} (-1)^p \binom{q}{p} \binom{N_{\text{SYK}} - q}{q - p}. \tag{2.4.2}$$

The Q-Hermite spectral density, $\rho_{QH}(E)$, is the following [22, 62, 63],

$$\rho_{QH}(E) = A\sqrt{1 - (E/E_0)^2} \prod_{k=0}^{\infty} \left[1 - \left(2\frac{E}{E_0}\right)^2 \frac{1}{1 + \eta^k + \eta^{-k}}\right] \tag{2.4.3}$$

where $A \approx 104$ is the normalization constant, which imposes that the total number of states is equal to $2^{N_{\text{SYK}}/2} = 8192$, $E_0 \approx -0.0032\ J$ is the ground state energy, and $\eta \approx -0.0072$ is the suppression factor. The spectral density, (2.4.3), is calculated in the double scaled limit, where $N_{\text{SYK}} \to \infty$, $q \to \infty$, and q^2/N_{SYK} fixed. We can see that there is strong agreement with the Q-hermite polynomial and the $q = 6$ SYK energy spectrum, which indicates that this model is a very good approximation of the double scaled limit.

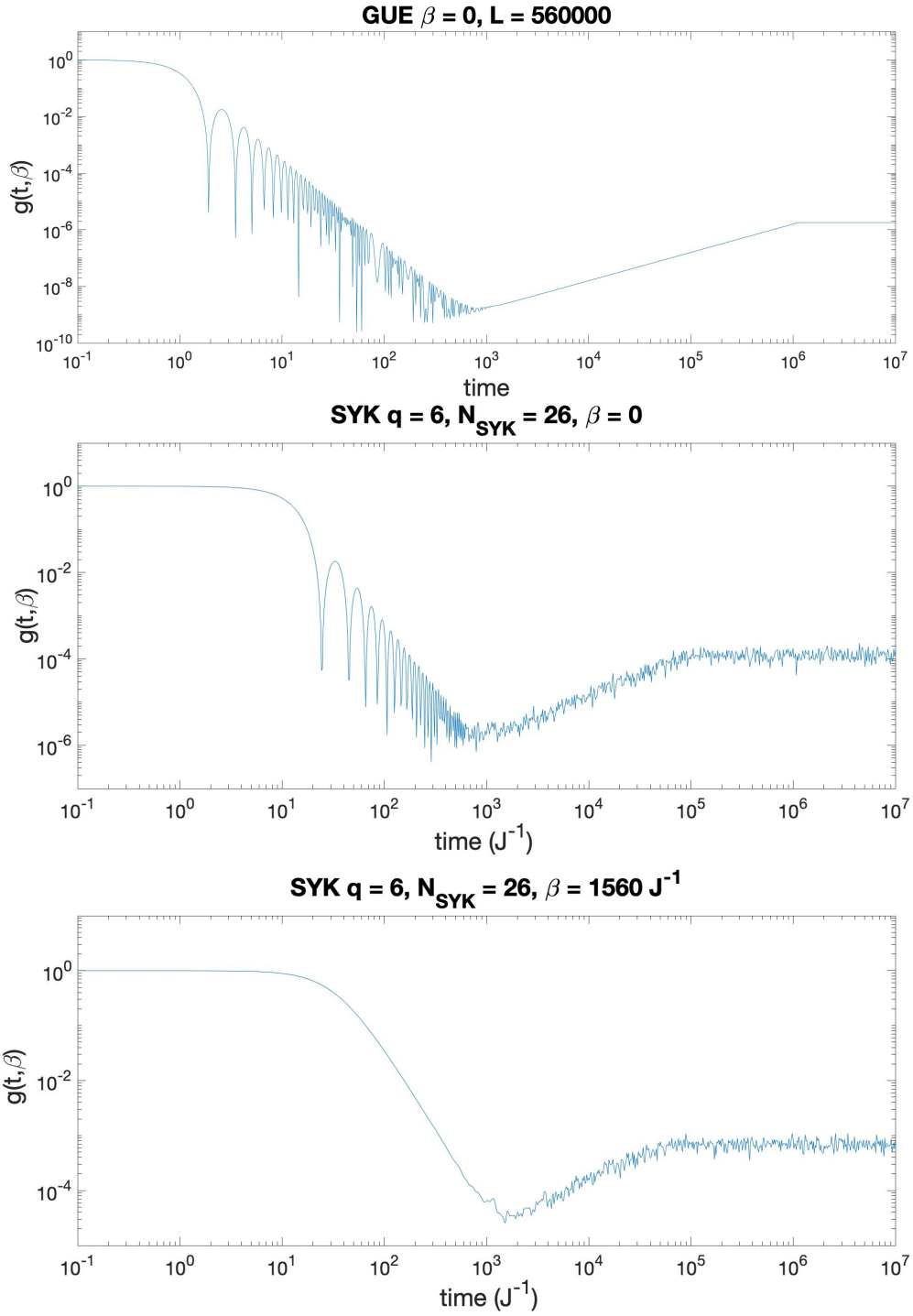

Figure 2.5: Top: SFF for the gaussian unitary ensemble (GUE) associated with the $q = 6$, $N_{\text{SYK}} = 26$ SYK model at $\beta = 0$. Middle: SFF for the $q = 6$, $N_{\text{SYK}} = 26$, $\beta = 0$ SYK model averaged over 49 samples. Bottom: SFF for the $q = 6$, $N_{\text{SYK}} = 26$, $\beta = 1560\ J^{-1}$ SYK model averaged over 49 samples.

Additionally, we can examine and compare the spectral form factor (SFF) for the SYK and tensor models (similar calculations in tensor models with $q = 4$ were performed in [16,17]). The SFF is a measure of the discreteness of the energy spectrum and can be defined as [22, 64]

$$g(t,\beta) = |Z(t,\beta)|^2/Z(\beta)^2, \quad \text{where} \quad Z(t,\beta) = \mathrm{Tr}(e^{-\beta H - iHt}) \ . \tag{2.4.4}$$

In figure 2.5 and figure 2.6, we display plots of the SFF for the $q = 6$ SYK and tensor models. For comparison, we have also plotted the SFF of the corresponding random matrix theory (RMT) ensemble, which is determined by the value of N_{SYK} mod 8 [22]. In our case, we plot for $N_{\mathrm{SYK}} = 26$, which is associated with the gaussian unitary ensemble (GUE). The SFF for the GUE that we have plotted is calculated in [65], and we have included the result at infinite temperature below:

$$g(t)_{GUE} = L^2 \left(\frac{J_1(2t)}{t} \right)^2 + L - L \times \begin{cases} 1 - \frac{t}{2L}, & t < 2L \\ 0, & t > 2L \end{cases} \tag{2.4.5}$$

$J_1(t)$ is the Bessel function of the first kind, and contributes to the early time oscillations of the GUE. L sets the size of the ensemble of random Hermitian matrices, and is related to the plateau time as $t_p = 2L$.

We can see that the SFF for the SYK model has the same features of the corresponding RMT ensemble, indicating properties of quantum chaos; in particular, the dip-ramp-plateau structure is present (see figure 2.5). Some of these properties are more difficult to see in the tensor model because the gaps in the energy spectrum

are sizable for the available value of N. However, we can notice a dip and plateau structure in our tensor model, which suggest signs of chaotic behavior, but there is no obvious ramp (see figure 2.6).

Despite clear differences in the finite N behavior of the tensor model and SYK model, we find that the large N solutions of the two models are identical. Before solving the large N models, we will discuss higher q tensor models followed by the large N limit and the melonic dominance of our tensor model.

2.5 Tensor models with $q > 6$

We begin with a discussion of $q = 8$, where the Majorana fermion tensor is of rank seven, and the model has $O(N)^7$ symmetry. In a 'generalized tetrahedral' interaction vertex, every two tensors have exactly one index in common. In contrast to the $q = 6$ case, there are six distinct such $q = 8$ interactions [50, 51]. However, only one of these interactions has the property that it stays connected whenever any 5 colors are erased. This is the maximally single-trace (MST) vertex in the terminology of [50], and we will show that in the Majorana model it produces a Hamiltonian which is fully antisymmetric under interchange of the $O(N)$ groups. The problem of finding the MST interactions is equivalent to the problem of finding the perfect 1-factorization of the complete graphs [52]. There are two classes where the existence of the perfect 1-factorizations has been proven: for graphs with $p + 1$ vertices or $2p$ vertices, where p is an odd prime number.

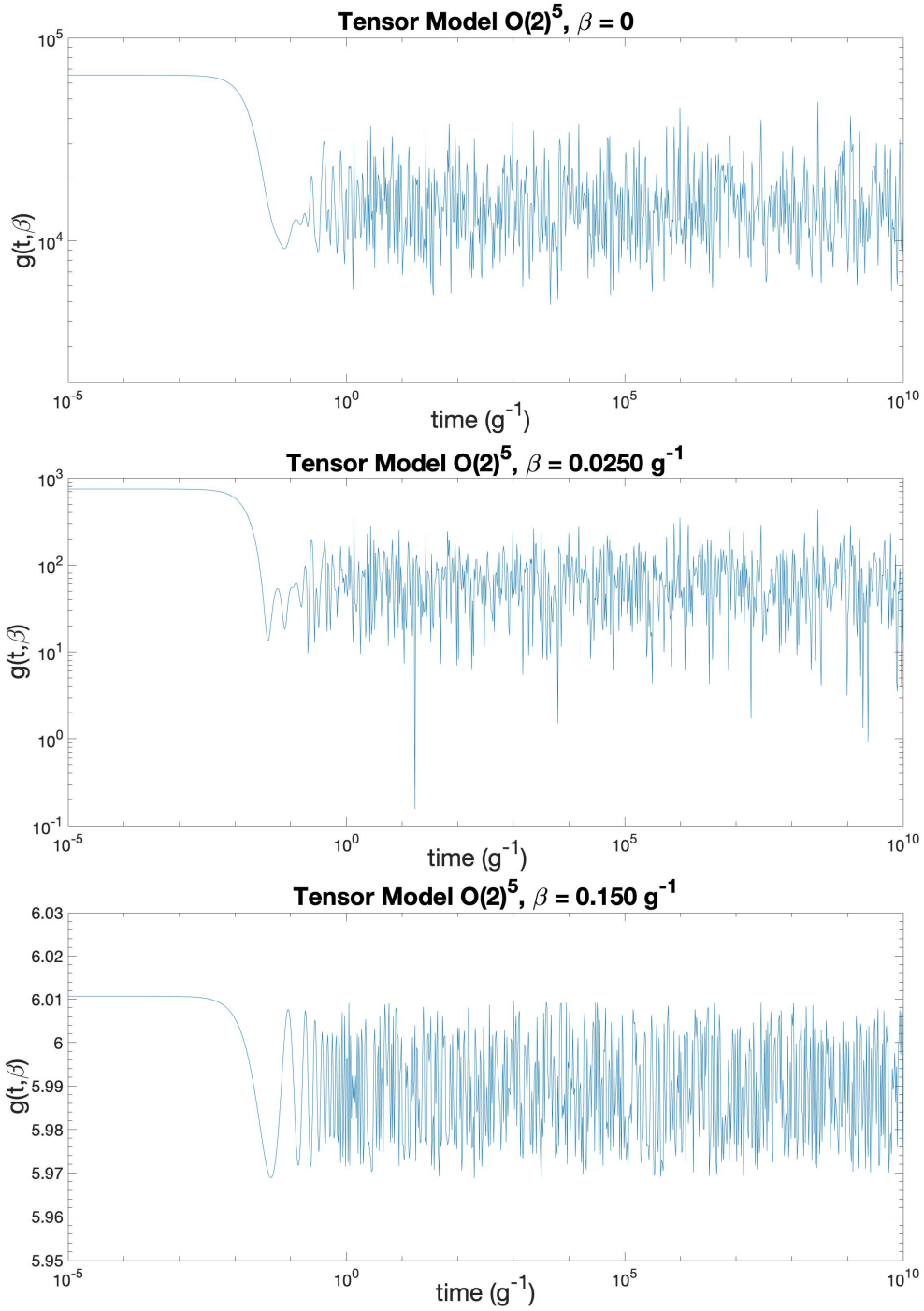

Figure 2.6: SFF for the $O(2)^5$ tensor model for three values of β. Top: $\beta = 0$, middle: $\beta = 0.0250\ g^{-1}$, and bottom: $\beta = 0.150\ g^{-1}$. Note that the fluctuations for the bottom subfigure are much smaller than the two above — this is because the SFF is calculated at a lower temperature.

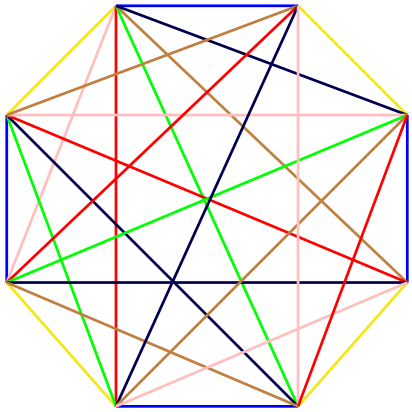

Figure 2.7: A graphical representation of the unique maximally single-trace tensor interaction for $q = 8$. It stays connected when any 5 out of the 7 colors are erased.

The $q = 8$ MST interaction is shown in figure 2.7. This interaction is called the canonical coloring [51]; this means that if we erase any set of 5 colors, we are left with an octagon composed of alternating colors. We can show the antisymmetry of this fermionic interaction as follows. Let us erase all colors except for groups $O(N)_a$ and $O(N)_b$ to get,

$$H_8 = \psi^{a_1b_1c_1d_1e_1f_1g_1}\psi^{a_1b_2c_2d_2e_2f_2g_2}\psi^{a_2b_1c_3d_3e_3f_3g_2}\psi^{a_2b_3c_1d_4e_2f_4g_3} \tag{2.5.1}$$

$$\psi^{a_3b_4c_3d_1e_4f_2g_3}\psi^{a_3b_2c_4d_4e_1f_3g_4}\psi^{a_4b_3c_2d_3e_4f_1g_4}\psi^{a_4b_4c_4d_2e_3f_4g_1} \longrightarrow$$

$$\longrightarrow H_2 = \psi^{a_1b_1}\psi^{a_1b_2}\psi^{a_2b_1}\psi^{a_2b_3}\psi^{a_3b_4}\psi^{a_3b_2}\psi^{a_4b_3}\psi^{a_4b_4}. \tag{2.5.2}$$

Now let us exchange the $O(N)_a$ and $O(N)_b$ groups of H_2 to get,

$$\begin{aligned} H_2' &= \psi^{a_1b_1}\psi^{a_2b_1}\psi^{a_1b_2}\psi^{a_3b_2}\psi^{a_4b_3}\psi^{a_2b_3}\psi^{a_3b_4}\psi^{a_4b_4} \\ &= -\psi^{a_1b_1}\psi^{a_1b_2}\psi^{a_2b_1}\psi^{a_2b_3}\psi^{a_3b_4}\psi^{a_3b_2}\psi^{a_4b_3}\psi^{a_4b_4} = -H_2. \end{aligned} \tag{2.5.3}$$

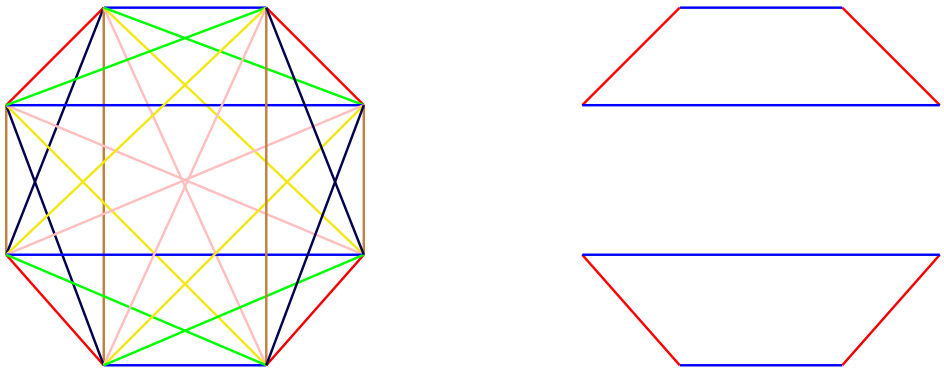

Figure 2.8: The graphical representation of a $q = 8$ tensor interaction which is not maximally single-trace. If we erase all but the blue and red stands, the graph becomes disconnected.

This is in contrast to the other $q = 8$ interactions that satisfy the constraint that one index is shared among any two pairs of fermions, all of which are provided in figure 2 of [51]. We give an example of a non-MST interaction in figure 2.8, corresponding to figure 2,a in [51]. When we erase all but two colors, we are left with two disconnected diagrams, which means this interaction is symmetric under exchange of these two colors.

Let us now comment on the $q = 8$ MST interaction. Since there is no i in this interaction, we have the time reversal symmetry. The $E \to -E$ symmetry comes from the antisymmetry under the exchange of two gauge groups. This interaction is melonic and scales as $g^2 N^{\frac{(q-1)(q-2)}{2}} = g^2 N^{21}$. In section 2.6, we will calculate the scaling dimensions of the bilinears of this model, and also include the result for general q tensor models.

We will define the group of coloring automorphisms, which will be used in calculating the propagator. One can think of a coloring automorphism as a permutation

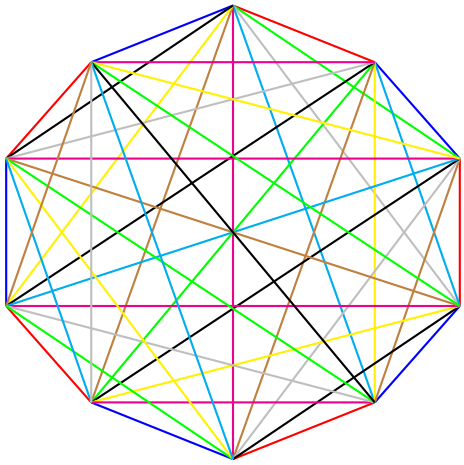

Figure 2.9: The graphical representation of the maximally single-trace tensor interaction for $q = 10$.

of the vertices of the interaction graph in a way that preserves the colors of the edges. Paper [51] explores these symmetries in more detail, and shows that the group of coloring automorphisms is $\mathbb{Z}_2^n$. Furthermore, [51] proves that for $q = u2^v$, u odd, melonic tensor models, the group of coloring automorphisms, which we will denote as Aut, can be at most $\mathbb{Z}_2^v$ for $u = 1$ and $\mathbb{Z}_2^{v-1}$ for $u > 1$.

There are six distinct $q = 8$ interactions that satisfy the constraint that each pair of Majorana fermions has a single index contraction. The difference between them is the order of the coloring automorphism group, which is taken into account in (2.6.1). The more symmetry our interaction has, the larger the order of the automorphism group will be. It follows that the $q = 8$ fully symmetric diagram has the largest group order, with $Aut = \mathbb{Z}_2^3$ [51]. As noted in section 2.6, the $|Aut|$ factor cancels out in the spectra calculation.

The number of possible 'generalized tetrahedral' interactions increases very rapidly with q [50, 51]: for $q = 8$ it is 6, for $q = 10$ it is 396, and for $q = 12$ it is $526,915,620$.

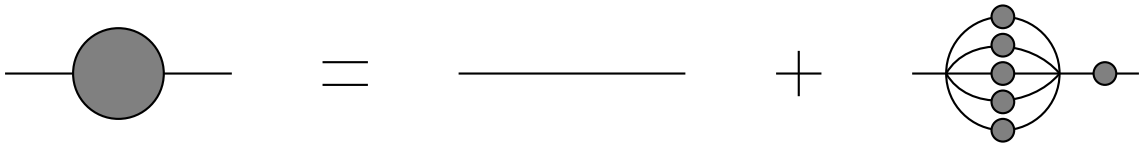

Figure 2.10: Melonic corrections to the propagator. These are the only diagrams that survive at large N.

However, at least for $q = 8$ and 10 the maximally single-trace vertex, or perfect one-factorization, is unique [50].[b] For $q = 10$, the MST vertex is shown in figure 2.9 (see also figure 5 of [50]).

2.6 Large-N scaling dimensions of the fermion bilinears

Due to the melonic dominance for the rank $q-1$ tensor models with MST interactions, we can sum the Feynman diagrams in these large-N theories. This allows us to calculate the propagator of fermionic fields and the spectrum of fermion bilinear operators. We expect the large-N solution of the MST tensor models to be similar to that of the SYK models, which also exhibit the melonic dominance. Indeed, in [49] it was shown that the four-point function for a rank $q-1$ tensor model has the same kernel as the SYK model four-point function with a q fermion interaction. In this section we present further results along these lines.

The large-N Schwinger-Dyson equation for the tensor model two point function with a six fermion interaction is represented diagrammatically in figure 2.10. We can

[b]The smallest value of q where the MST vertex is not unique is 12. We thank Fidel Schaposnik Massolo for informing us of this and providing a reference, [53].

write the Schwinger-Dyson equations from the diagrams in figure 2.10. We start with an MST q-tensor interaction,

$$G(t) = \langle T\psi(t)\psi(0)\rangle = (\partial_t - \Sigma)^{-1}, \quad \Sigma = q|Aut|g^2 N^{\frac{(q-1)(q-2)}{2}} G^{q-1}, \tag{2.6.1}$$

where $|Aut|$ is the order of the automorphism group of the interaction (see section 2.5), and $q|Aut|$ is the number of contributing Feynman diagrams [51]. We introduce $\lambda^2 = q|Aut|g^2 N^{\frac{(q-1)(q-2)}{2}}$, and we make the assumption that in the IR regime the Σ will dominate the derivative. Thus, we use the following conformal ansatz,

$$G(t) = \frac{a\,\mathrm{sign}(t)}{|t|^{2\Delta}}, \quad \Sigma(t) = \lambda^2 \frac{a^{q-1}\mathrm{sign}(t)}{|t|^{2(q-1)\Delta}}. \tag{2.6.2}$$

We take the Fourier transform of (2.6.2) and arrive at,

$$\begin{aligned} G(\omega) &= 2^{1-2\Delta} i\sqrt{\pi}\frac{\Gamma(1-\Delta)}{\Gamma(1/2+\Delta)} a|\omega|^{2\Delta-1}\mathrm{sign}(\omega), \\ \Sigma(\omega) &= 2^{1-2(q-1)\Delta} i\sqrt{\pi}\frac{\Gamma(1-(q-1)\Delta)}{\Gamma(1/2+(q-1)\Delta)} a^{q-1}\mathrm{sign}(\omega)\lambda^2|\omega|^{2(q-1)\Delta-1}. \end{aligned} \tag{2.6.3}$$

In the IR limit we assume that we can neglect the derivative and get $G = -1/\Sigma$. From this we arrive at

$$-1 = G(\omega)\Sigma(\omega) = -2^{2-2q\Delta} a^q \lambda^2 \pi \frac{\Gamma(1-\Delta)\Gamma(1-(q-1)\Delta)}{\Gamma(1/2+\Delta)\Gamma(1/2+(q-1)\Delta)} |\omega|^{2q\Delta-2}. \tag{2.6.4}$$

It follows that $\Delta = 1/q$ and $a^q = \frac{\Gamma(\frac{1}{2}+\Delta)\Gamma(\frac{3}{2}-\Delta)}{\pi\lambda^2\Gamma(1-\Delta)\Gamma(\Delta)}$. Thus, we have that the propagator is,

$$G(t) = \left(\frac{\Gamma(\frac{1}{2}+\Delta)\Gamma(\frac{3}{2}-\Delta)}{\pi\lambda^2\Gamma(1-\Delta)\Gamma(\Delta)}\right)^{\frac{1}{q}} \frac{\text{sign}(t)}{|t|^{2\Delta}}, \tag{2.6.5}$$

which exactly matches that of the general q SYK model [66]. For $q = 6$ and $q = 8$ we have,

$$G_6(t) = \left(\frac{\sqrt{3}}{9\pi\lambda^2}\right)^{\frac{1}{6}} \frac{\text{sign}(t)}{|t|^{1/3}}, \quad G_8(t) = \left(\frac{3}{8\pi\lambda^2\cot(\frac{\pi}{8})}\right)^{\frac{1}{8}} \frac{\text{sign}(t)}{|t|^{1/4}}. \tag{2.6.6}$$

Using this propagator we can study the spectrum of bilinear operators.

Let us first compare the combinatorial factors in the ladder diagrams, shown in figure 2.11, to those in the melonic diagrams for the two-point function, shown in figure 2.10 . As stated above, there are $q|Aut|$ Feynman diagrams that must be counted for each melon insertion. We note that the ladder diagrams may be constructed by 'cutting' one of the internal legs of the melonic diagrams for the two-point function. There are $(q-1)$ choices of which leg to cut. This means that, for every diagram in figure 2.10, we can make $(q-1)$ ladder diagrams by cutting the different internal propagators. So, we have a combinatoricial factor of $q(q-1)|Aut|$ for the ladder diagram. Thus, the factors of $|Aut|$ cancel in the operator spectra calculation, and we find that the spectrum is identical to that of the corresponding q SYK model. The calculation is presented in the following.

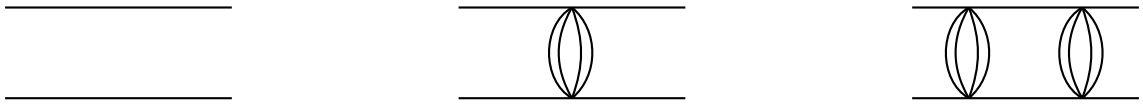

Figure 2.11: A few of the ladder diagrams that contribute to the four-point function.

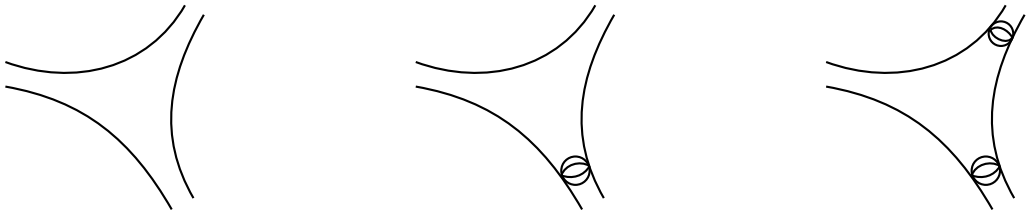

Figure 2.12: Examples of planar diagram contributions to the six-point diagram for the $O(N)^5$ model. There is also another contribution class of diagrams called 'contact' diagrams that are not pictured here [66]. Corrections to the six point function are made by inserting ladder diagrams and melonic corrections.

The kernel comes from one rung of the ladder in figure 2.11. In the general q case, we get that the kernel exactly matches that of the general q SYK model [4]:

$$\hat{K}_q = K_q(t_1, t_2; t_3, t_4) = -(q-1)\lambda^2 G(t_{13}) G^{q-2}(t_{34}) G(t_{24}). \tag{2.6.7}$$

For the $q = 6$ and $q = 8$ case, we have

$$\begin{aligned} \hat{K}_6 &= K_6(t_1, t_2; t_3, t_4) = -5\lambda^2 G(t_{13}) G^4(t_{34}) G(t_{24}), \\ \hat{K}_8 &= K(t_1, t_2; t_3, t_4) = -7\lambda^2 G(t_{13}) G^6(t_{34}) G(t_{24}). \end{aligned} \tag{2.6.8}$$

We substitute the ansatz for the spectrum of singlet bilinears as

$$\begin{aligned} v_{i_1 \ldots i_{q-1}, j_1 \ldots j_{q-1}}(t_1, t_2) &= \langle T O(\infty) \psi_{i_1 \ldots i_{q-1}}(t_1) \psi_{j_1 \ldots j_{q-1}}(t_2) \rangle \\ &= \delta_{i_1 j_1} \ldots \delta_{i_{q-1} j_{q-1}} \frac{\operatorname{sign}(t_1 - t_2)}{|t_1 - t_2|^{2\Delta - h}}, \end{aligned}$$

where h is the dimension of the operator $O(t)$. The spectrum of operators for the $q = 6$ model is computed as follows:

$$\hat{K}v(t_1,t_2) = \int dt_3 dt_4 K(t_1,t_2;t_3,t_4)v(t_3,t_4) =$$
$$= -\frac{5\sqrt{3}}{9\pi}\int dt_3 dt_4 \frac{\text{sign}(t_1-t_3)\text{sign}(t_3-t_4)\text{sign}(t_4-t_2)}{|t_1-t_3|^{\frac{1}{3}}|t_3-t_4|^{\frac{5}{3}-h}|t_4-t_2|^{\frac{1}{3}}} = g_a(h)v(t_1,t_2),$$
$$\text{where} \quad g_a(h) = -5\frac{\Gamma\left(\frac{3}{2}-\Delta\right)\Gamma\left(1-\Delta\right)}{\Gamma\left(\frac{1}{2}+\Delta\right)\Gamma\left(\Delta\right)}\frac{\Gamma\left(\Delta+\frac{h}{2}\right)\Gamma\left(\frac{1}{2}+\Delta-\frac{h}{2}\right)}{\Gamma\left(\frac{3}{2}-\Delta-\frac{h}{2}\right)\Gamma\left(1-\Delta+\frac{h}{2}\right)}\ , \qquad (2.6.9)$$

and $\Delta = \frac{1}{6}$. The scaling dimensions of bilinear operators $\psi_{abcde}\partial_t^{2n+1}\psi_{abcde}$ are determined by the equation $g_a(h) = 1$, and its form coincides with that for the SYK model [4]:

$$g_a(h) = -(q-1)\frac{\Gamma\left(\frac{3}{2}-\Delta\right)\Gamma\left(1-\Delta\right)}{\Gamma\left(\frac{1}{2}+\Delta\right)\Gamma\left(\Delta\right)}\frac{\Gamma\left(\Delta+\frac{h}{2}\right)\Gamma\left(\frac{1}{2}+\Delta-\frac{h}{2}\right)}{\Gamma\left(\frac{3}{2}-\Delta-\frac{h}{2}\right)\Gamma\left(1-\Delta+\frac{h}{2}\right)}\ , \qquad \Delta = \frac{1}{q} \qquad (2.6.10)$$

after setting $q = 6$. There is a solution at $h = 2$, which is the mode dual to the excitation in Jackiw-Teitelboim dilaton gravity [67–70]. One can show that the spectrum has the following asymptotic behavior, $h \to 2n + 4/3$ as $n \to \infty$.

In contrast to the SYK model, the tensor model contains operators which are $SO(N)$ symmetry generators, such as $J_{aa'} = \psi_{abcde}\psi_{a'bcde}$. If there are no ladder corrections to this operator, we would find that its scaling dimension is $\Delta_J = 2\Delta_\psi = \frac{1}{3}$; this would contradict the conservation of such charges. In fact, one can verify that there are ladder corrections to the operator which are non-vanishing in the melonic large N limit [28] (see figure 2.13). Their feature is that, due to the antisymmetry in

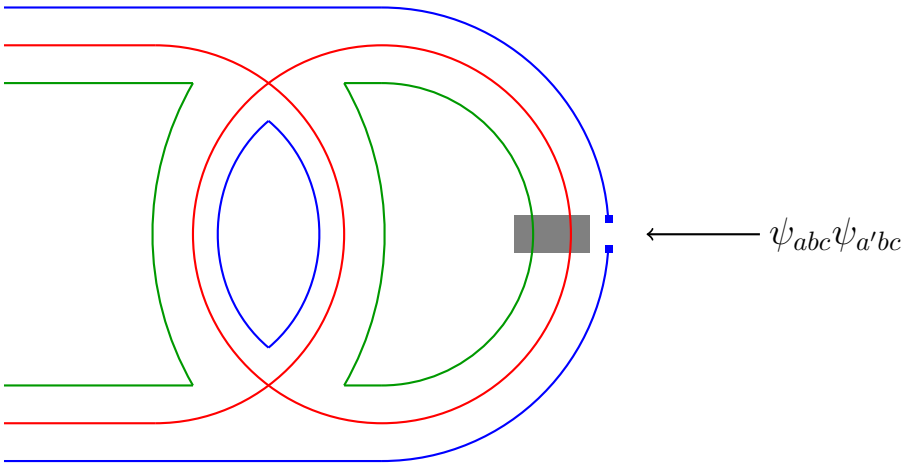

Figure 2.13: The insertion of the colored operator can suppress some diagrams, in contrast to the insertion of the singlet operator. For example, if one inserts the operator of the form $\psi_{ab\ldots yz}\partial_t^{2n+1}\psi_{ab\ldots yz'}$, only one diagram contributes in the large N limit, compared to the $(q-1)$ contributions from a singlet operator. Figure is adapted from reference [44].

a and a', the relevant eigenfunctions are symmetric [28]:

$$v(t_1,t_2)=\langle TO(\infty)\psi_I(t_1)\psi_J(t_2)\rangle=\delta_{IJ}\frac{1}{|t_1-t_2|^{1/3-h}}. \tag{2.6.11}$$

Thus, we have

$$\hat{K}v(t_1,t_2)=\frac{-\sqrt{3}}{9\pi}\int dt_3dt_4\frac{\text{sign}(t_1-t_3)\text{sign}(t_4-t_2)}{|t_1-t_3|^{\frac{1}{3}}|t_3-t_4|^{\frac{5}{3}-h}|t_4-t_2|^{\frac{1}{3}}}=g_s(h)v(t_1,t_2). \tag{2.6.12}$$

In general [71],

$$g_s(h)=-\frac{\Gamma\left(\Delta-\frac{h}{2}\right)\Gamma\left(\Delta+\frac{h}{2}-\frac{1}{2}\right)\Gamma\left(1-\Delta\right)\Gamma\left(3/2-\Delta\right)}{\Gamma\left(\frac{1}{2}+\frac{h}{2}-\Delta\right)\Gamma\left(1-\Delta-\frac{h}{2}\right)\Gamma\left(\frac{1}{2}+\Delta\right)\Gamma\left(\Delta\right)},\qquad \Delta=\frac{1}{q}\ , \tag{2.6.13}$$

and here we set $q=6$.

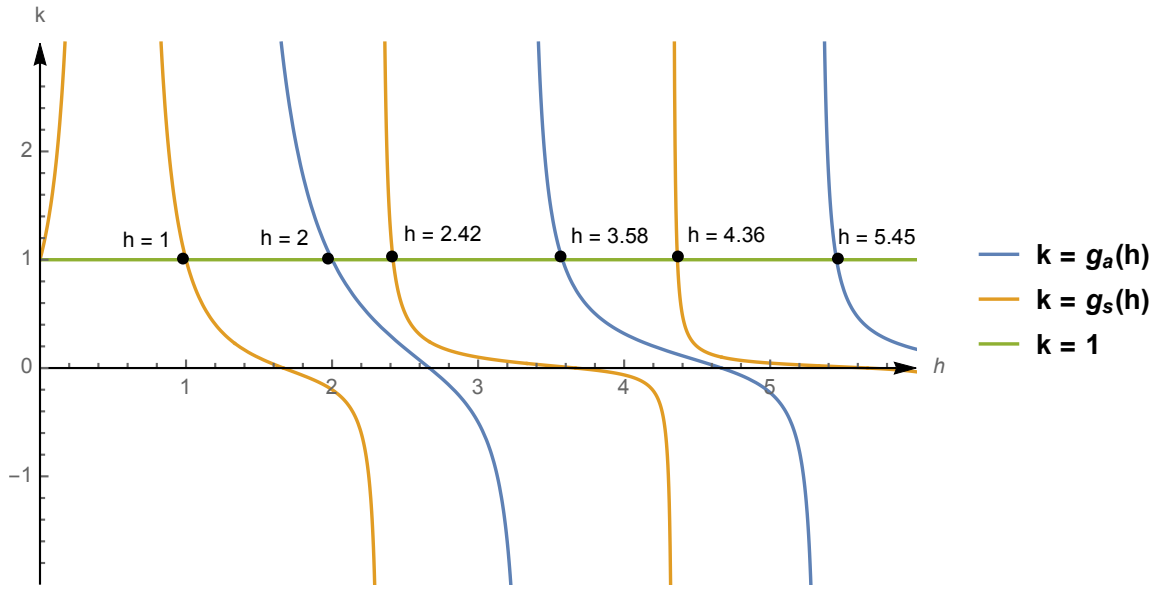

Figure 2.14: The dimensions of bilinear operators in the $O(N)^5$ model.

The equation for the scaling dimensions in the symmetric sector is $g_s(h) = 1$, and one can check that $h = 0$ is a solution of this equation; it corresponds to a conserved charge. The asymptotic behavior of the eigenvalues is $h \to 2n + 1/3$, corresponding to operators $\psi_{abcde}\partial_t^{2n}\psi_{a'bcde}$.

In an analogous manner, we can compute the spectrum of operators for $q = 8$,

$$\begin{aligned}\int dt_3 dt_4 K(t_1, t_2; t_3, t_4) v(t_3, t_4) &= g_a(h) v(t_1, t_2) \\ &= -\frac{21}{8\pi \cot(\frac{\pi}{8})} \int dt_3 dt_4 \frac{\text{sign}(t_1 - t_3)\text{sign}(t_3 - t_4)\text{sign}(t_2 - t_4)}{|t_1 - t_3|^{\frac{1}{4}} |t_3 - t_4|^{\frac{7}{4} - h} |t_2 - t_4|^{\frac{1}{4}}}\end{aligned} \tag{2.6.14}$$

where $g_a(h)$ is given by (2.6.10) with $q = 8$. The scaling dimension is determined by the equation $g_a(h) = 1$. We can verify that there are no complex modes, that $g_a(h) = g_a(1 - h)$, and that there exists a solution at $h = 2$, see figure 2.15.

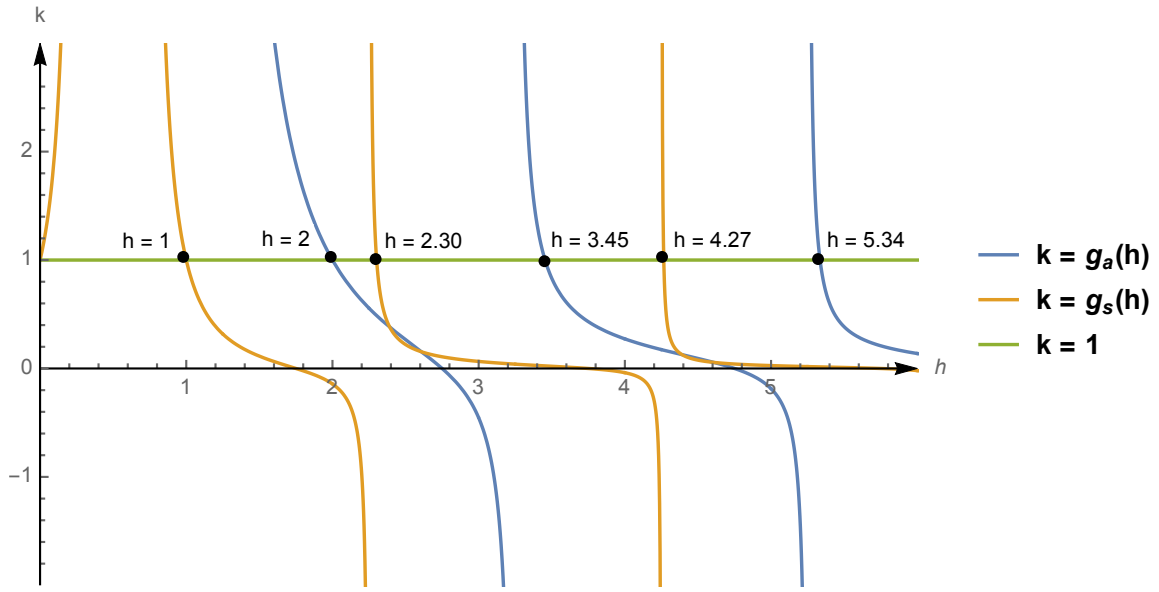

Figure 2.15: The dimensions of bilinear operators in the $O(N)^7$ model.

We can similarly examine the symmetric sector, where our ansatz is now,

$$v(t_1, t_2) = \frac{1}{|t_1 - t_2|^{1/4-h}}. \tag{2.6.15}$$

Performing the analogous calculations, we find that,

$$\begin{aligned}\int dt_3 dt_4 K(t_1, t_2; t_3, t_4) v(t_3, t_4) &= -\frac{3}{8\pi \cot(\frac{\pi}{8})} \int dt_3 dt_4 \frac{\text{sign}(t_1 - t_3)\text{sign}(t_2 - t_4)}{|t_1 - t_3|^{\frac{1}{4}} |t_3 - t_4|^{\frac{7}{4}-h} |t_2 - t_4|^{\frac{1}{4}}} \\ &= g_s(h) v(t_1, t_2) \ ,\end{aligned} \tag{2.6.16}$$

and $g_s(h)$ is obtained from (2.6.13) by setting $q = 8$.

2.7 $SO(N)^5$ invariant quartic operators

In this section we classify the $SO(N)^5$ invariant quartic operators in the theory (2.1.1) according to their transformational properties under the action of the discrete symmetry S_5 discussed in section 2.2.1. We will show that these operators do not transform nicely under the $A_5 \subset S_5$ symmetry which consists of the even permutations of the five $O(N)$ groups. In order to find the possible singlet quartic operators, we must find all the distinct ways the indices of the four fermions may be contracted. We pictorially represent the quartic operators of the theory in table 2.4. We represent each fermion as a vertex and the index contractions are represented by edges connecting the distinct vertices. We can denote the number of edges connecting each vertex to the others by three integers ρ_a, ρ_b, and ρ_c. To find the possible quartic operators in this theory we consider all possible combinations of integers ρ_a, ρ_b, and ρ_c that satisfy the relations that the number of edges at each vertex is five ($\rho_a + \rho_b + \rho_c = 5$) and that a fully connected quartic operator must not have more than four strands shared between two nodes ($5 > \rho_a \geq \rho_b \geq \rho_c \geq 0$). We find the following triples: $(4,1,0)$, $(3,2,0)$, $(3,1,1)$, and $(2,2,1)$. Each triplet corresponds to the construction of a quartic term displayed in table 2.4, and they are of the following form: $\psi^{a_1b_1c_1d_1e_1}\psi^{a_2b_2c_1d_1e_2}\psi^{a_1b_1c_2d_2e_2}\psi^{a_2b_2c_2d_2e_1}$ corresponding to $(2,2,1)$ in row 1, $\psi^{a_1b_1c_1d_1e_1}\psi^{a_2b_2c_2d_2e_1}\psi^{a_1b_1c_1d_1e_2}\psi^{a_2b_2c_2d_2e_2}$ corresponding to $(4,1,0)$ in row 2, $\psi^{a_1b_1c_1d_1e_1}\psi^{a_2b_2c_2d_1e_1}\psi^{a_1b_1c_1d_2e_2}\psi^{a_2b_2c_2d_2e_2}$ corresponding to $(3,2,0)$ in row 3, and corresponding to $(3,1,1)$ in row 4 is $\psi^{a_1b_1c_1d_1e_1}\psi^{a_2b_2c_2d_1e_2}\psi^{a_1b_1c_1d_2e_2}\psi^{a_2b_2c_2d_2e_1}$.

Now we can find the irreducible representations of S_5 of each of the possible quartic operators and show that none transform nicely under A_5. We use character theory to

do this. Let us first note that S_5 is a symmetric group consisting of 120 permutations of five elements. The conjugacy classes of S_5 are included in the top row of table 2.4 and include:

1. No change, which we denote as 1 in the top row of table 2.4.
2. Interchanging two elements, which we denote as (12).
3. Cycling three elements, which we denote as (123).
4. Cycling four elements, which we denote as (1234).
5. A cyclic permutation of all five elements, which we denote as (12345).
6. Interchanging two pairs of elements, which we denote as (12)(34).
7. Interchanging two elements and cycling the remaining three elements, which we denote as (12)(345).

We must consider the number of fixed points (the character) of each of the operators under the action of each of the conjugacy classes of S_5. In terms of our quartic operators, we may think of a conjugacy class acting by interchanging some number of $O(N)$ groups/colors. For example, the conjugacy class (12)(345) can be thought of as the relabeling $a \leftrightarrow b$ and $c \to d \to e \to c$ in the quartic operator. There are 20 such relabelings in this example, since there are $\binom{5}{3} = 10$ ways to choose the set of three and 2 ways to order each cycle. The negative values represent the exchange of an odd number of vertices of the operator under the conjugacy class. By calculating the inner products of the characters of the operators with the characters of the irreducible representation, we can find the correct group decomposition [72].

As an illustration, we include a detailed computation of the character of the quartic operator in row 2 of table 2.4: $\psi^{a_1 b_1 c_1 d_1 e_1}\psi^{a_2 b_2 c_2 d_2 e_1}\psi^{a_1 b_1 c_1 d_1 e_2}\psi^{a_2 b_2 c_2 d_2 e_2}$. Let

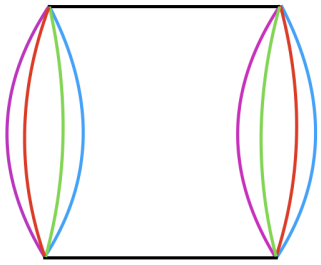

Figure 2.16: We can exchange the black line for any of the other four colors. Thus, there are five possible diagrams of this type. This diagram corresponds to type $(4,1,0) = \psi^{a_1b_1c_1d_1e_1}\psi^{a_2b_2c_2d_2e_1}\psi^{a_1b_1c_1d_1e_2}\psi^{a_2b_2c_2d_2e_2}$.

us note that there are five different diagrams of this type, see figure 2.16, since the only degree of freedom here is the choice of the top/bottom rung, and we have five indices to choose from. Therefore, the character for the column 1 is five. Now, let us find the character for the (12) column. We let (12) correspond to $a \leftrightarrow b$. We find that our operator is invariant only when neither a nor b is the top/bottom rung. There are only three diagrams of this type, so the character of column (12) is three. Next, we let (123) correspond to $a \to b \to c \to a$. The invariant diagrams are those that have d or e as the top/bottom rung. Thus, the character of column (123) is two. We let (1234) correspond to $a \to b \to c \to d \to a$. Now there is only one invariant diagram: the one with c as the top/bottom rung. Finally, we let (12)(34) correspond to $a \leftrightarrow b$ and $c \leftrightarrow d$. The single invariant diagram here is again the one with c as the top/bottom rung. So, the character for both (1234) and (12)(34) is one. The remaining two columns, (12345) corresponding to $a \to b \to c \to d \to e \to a$ and (12)(345) corresponding to $a \leftrightarrow b$ and $c \to d \to e \to a$, leave none of the five diagrams invariant and have character equal to zero.

Now that we have the characters for this quartic operator, we can find its decomposition in terms of S_5 irreducible representation. To do this, we must refer to the character table of the S_5 irreducible representations, see table 2.3. We define the character vector of our quartic operator Q (row 2 in table 2.3),

$$\chi_Q = \langle 5, 3, 2, 1, 0, 1, 0 \rangle . \tag{2.7.1}$$

We define the inner product of two characters as,

$$\langle \chi_i, \chi_j \rangle = \frac{1}{|G|} \sum_{g \in G} |g| \chi_{i,g} \chi_{j,g}, \tag{2.7.2}$$

where $|G|$ is the order of the group, g is the conjugacy class, and $|g|$ is the order of the conjugacy class. We take the inner product of χ_Q with itself to determine how many irreducible representations of S_5 make up Q,

$$\langle \chi_Q, \chi_Q \rangle = \frac{1}{|S_5|} \left(5^2 \cdot 1 + 3^2 \cdot 10 + 2^2 \cdot 20 + 1^2 \cdot 30 + 0^2 \cdot 24 + 1^2 \cdot 15 + 0^2 \cdot 20 \right) = 2, \tag{2.7.3}$$

where we have used that $|S_5| = 120$. Since $\langle \chi_Q, \chi_Q \rangle$ is equal to the sum of two squares $(1^2 + 1^2)$, we determine that our operator Q consists of two irreducible representations of S_5. To find which ones, we must take the inner product of χ_Q with χ_i where

$i = \mathbf{1} \ldots \mathbf{7}$ indicates the irreducible representation as defined in table 2.3.

$$\begin{aligned}
\langle \chi_Q, \chi_{\mathbf{1}} \rangle &= \frac{1}{|S_5|} (5 \cdot 1 + 3 \cdot 10 + 2 \cdot 20 + 1 \cdot 30 + 1 \cdot 15) = 1 \\
\langle \chi_Q, \chi_{\mathbf{2}} \rangle &= \frac{1}{|S_5|} (5 \cdot 1 - 3 \cdot 10 + 2 \cdot 20 - 1 \cdot 30 + 1 \cdot 15) = 0 \\
\langle \chi_Q, \chi_{\mathbf{3}} \rangle &= \frac{1}{|S_5|} (5 \cdot 1 \cdot 4 - 3 \cdot 10 \cdot 2 + 2 \cdot 20 \cdot 1) = 0 \\
\langle \chi_Q, \chi_{\mathbf{4}} \rangle &= \frac{1}{|S_5|} (5 \cdot 1 \cdot 4 + 3 \cdot 10 \cdot 2 + 2 \cdot 20 \cdot 1) = 1 \\
\langle \chi_Q, \chi_{\mathbf{5}} \rangle &= \frac{1}{|S_5|} (5 \cdot 1 \cdot 5 + 3 \cdot 10 \cdot 1 - 2 \cdot 20 \cdot 1 - 1 \cdot 30 \cdot 1 + 1 \cdot 15 \cdot 1) = 0 \\
\langle \chi_Q, \chi_{\mathbf{6}} \rangle &= \frac{1}{|S_5|} (5 \cdot 1 \cdot 6 - 1 \cdot 15 \cdot 2) = 0 \\
\langle \chi_Q, \chi_{\mathbf{7}} \rangle &= \frac{1}{|S_5|} (5 \cdot 1 \cdot 5 - 3 \cdot 10 \cdot 1 - 2 \cdot 20 \cdot 1 + 1 \cdot 30 \cdot 1 + 1 \cdot 15 \cdot 1) = 0
\end{aligned} \tag{2.7.4}$$

Thus, we can conclude that our operator Q can be decomposed into $\mathbf{1} \bigoplus \mathbf{4}$.

This computation was done for the possible quartic operators of $O(N)^5$; their character tables and irreducible representations of S_5 are summarized in table 2.4.

2.8 Appendix: Subchromatic interactions

We consider subchromatic interactions in this section, meaning the rank of the tensor for a size q interaction term is $< (q-1)$. Specifically, we consider a rank three, $q = 8$ Hamiltonian, and a rank four, $q = 8$ Hamiltonian. The MST interaction is no longer unique in both cases. The paper [73] finds that, for an order q and rank r MST

Irreducible Representation	1 1	10 (1 2)	20 (1 2 3)	30 (1 2 3 4)	24 (1 2 3 4 5)	15 (1 2) (3 4)	20 (1 2) (3 4 5)
1	1	1	1	1	1	1	1
2	1	-1	1	-1	1	1	-1
3	4	-2	1	0	-1	0	1
4	4	2	1	0	-1	0	-1
5	5	1	-1	-1	0	1	1
6	6	0	0	0	1	-2	0
7	5	-1	-1	1	0	1	-1

Table 2.3: The character table of the irreducible representations of S_5. The number above each conjugacy class in the first row is the order of that class. Here, **1** is the trivial representation, **2** is the sign representation, **3** is the product of the standard and sign representation, **4** is the standard representation, **5** is the irreducible five dimensional representation, **6** is the exterior square of the standard representation, and **7** is the product of the sign and the irreducible five dimensional representation.

operators	1	(1 2)	(1 2 3)	(1 2 3 4)	(1 2 3 4 5)	(1 2) (3 4)	(1 2) (3 4 5)	irreps
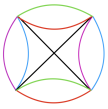	15	3	0	-1	0	-1	0	$\mathbf{4} \oplus \mathbf{6} \oplus \mathbf{5}$
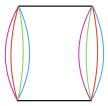	5	3	2	1	0	1	0	$\mathbf{1} \oplus \mathbf{4}$
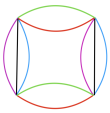	10	4	1	0	0	2	1	$\mathbf{1} \oplus \mathbf{4} \oplus \mathbf{5}$
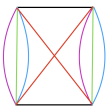	10	2	1	0	0	-2	-1	$\mathbf{4} \oplus \mathbf{6}$

Table 2.4: Character Table for Quartic Operators. **1** is the trivial representation, **4** is the standard representation, **6** is the exterior square of the standard representation, and **5** is the irreducible 5 dimensional representation.

interaction, the melonic diagrams dominate with the quantity

$$\lambda^2 = g^2 N^{r(q-2)/2} \tag{2.8.1}$$

held constant in the large N limit.

2.8.1 Rank three, $q = 8$

We write an MST interaction for the rank three, $q = 8$ interaction, which contains a set of N^3 Majorana fermions ψ^{abc} with the anti-commutation relation,

$$\{\psi^{abc}, \psi^{a'b'c'}\} = \delta^{aa'}\delta^{bb'}\delta^{cc'}. \tag{2.8.2}$$

The interaction term corresponding to the MST interaction depicted in figure 2.17 is,

$$H_{8,\text{rank3}} \sim g\psi^{a_1b_1c_1}\psi^{a_1b_2c_2}\psi^{a_2b_1c_2}\psi^{a_2b_3c_3}\psi^{a_3b_4c_3}\psi^{a_3b_2c_4}\psi^{a_4b_3c_4}\psi^{a_4b_4c_1}. \tag{2.8.3}$$

The Hermitian Hamiltonian is $H = H_{8,\text{rank3}} + H^\dagger_{8,\text{rank3}}$, and in the classical approximation where we neglect the delta terms (2.8.2), the interaction changes sign under any interchange of two $O(N)$ groups. When we take (2.8.2) into account, we no longer find that $H \to -H$ under the permutation of any two $O(N)$ groups. This is due to the sextic terms that appear during anticommutation. We note that this model does not possess the spectral mirror symmetry property characteristic of the SYK model. The large N limit of this theory must be taken while holding g^2N^9 fixed [73].

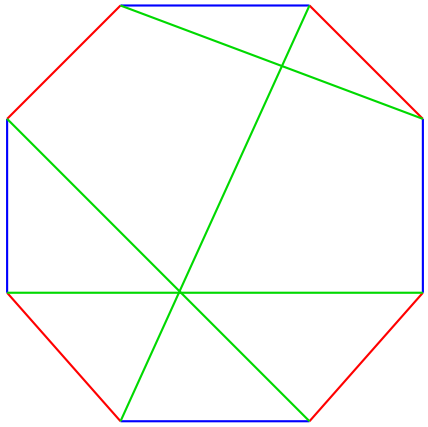

Figure 2.17: A graphical representation of a rank three, $q = 8$ MST interaction.

Group Permutation	Index relabeling
$O(N)_a$ and $O(N)_b$	$c_3 \leftrightarrow c_4$.
$O(N)_b$ and $O(N)_c$	$a_3 \leftrightarrow a_4$, $b_1 \leftrightarrow b_2$, $c_1 \leftrightarrow c_2$.
$O(N)_a$ and $O(N)_c$	$a_1 \leftrightarrow a_2$, $a_3 \leftrightarrow a_4$, $b_3 \leftrightarrow b_4$, $c_1 \leftrightarrow c_2$, $c_3 \leftrightarrow c_4$.

Table 2.5: Group permutations that send H to $-H$ in the classical approximation of the rank three, $q = 8$ MST interaction (2.8.3).

This interaction has $O(N)^3$ symmetry, and here we study the spectrum of the Hermitian rank three, $q = 8$ model with $O(2) \times O(3)^2$ symmetry. Here we have 18 Majorana fermions with $2^9 = 512$ states. We let the Majorana fermions be the gamma matrices of $SO(18)$, see figure 2.18. This energy spectrum is not symmetric about any shift in energy.

2.8.2 Rank four, $q = 8$

We begin by writing an MST interaction for the rank four, $q = 8$ interaction. This model contains a set of N^4 Majorana fermions ψ^{abcd} with the usual anti-commutation

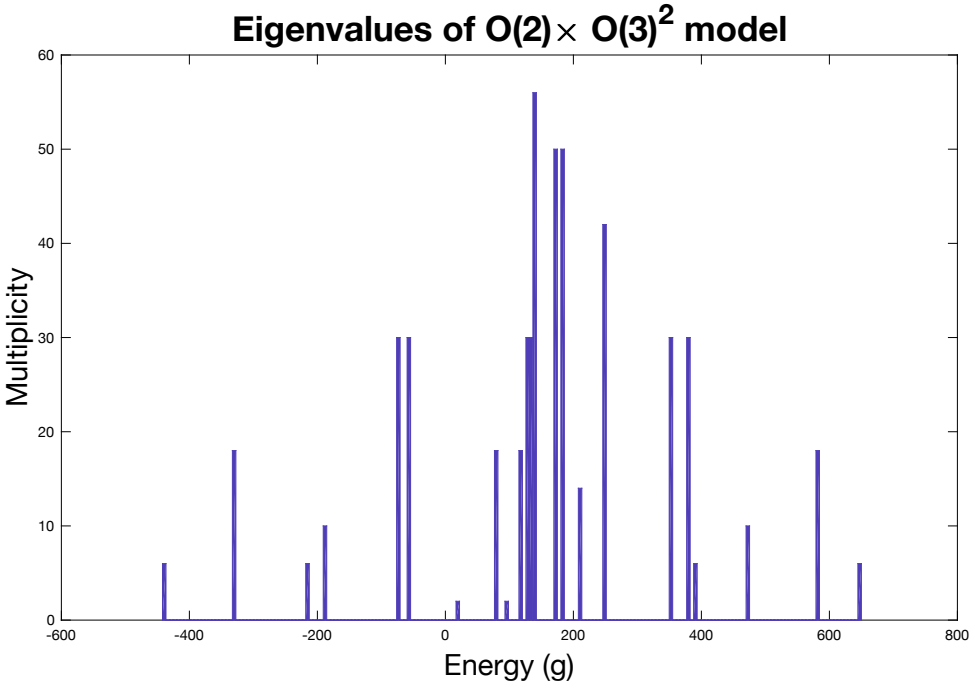

Figure 2.18: Energy spectrum of the rank three, $q = 8$ model with $O(2) \times O(3)^2$ model.

relation,

$$\{\psi^{abcd}, \psi^{a'b'c'd'}\} = \delta^{aa'}\delta^{bb'}\delta^{cc'}\delta^{dd'}. \tag{2.8.4}$$

The interaction term corresponding to figure 2.19 below is,

$$H_{8,\text{rank4}} \sim ig\psi^{a_1b_1c_1d_1}\psi^{a_1b_2c_2d_2}\psi^{a_2b_1c_3d_2}\psi^{a_2b_3c_4d_3}\psi^{a_3b_4c_3d_3}\psi^{a_3b_2c_1d_4}\psi^{a_4b_3c_2d_4}\psi^{a_4b_4c_4d_1}. \tag{2.8.5}$$

This Hamiltonian is Hermitian, and as in the $q = 6$ MST interaction, we may consider the action of the time reversal operator, T, on (2.8.5). Similar to the $q = 6$ MST interaction, this interaction does not possess time reversal symmetry because of the i needed to make the Hamiltonian real,

$$TiT^{-1} = -i, \quad T\psi^{abc}T^{-1} = \psi^{abc}, \quad TH_8T^{-1} = -H_8. \tag{2.8.6}$$

From (2.8.6), we see that the eigenvalues come in pairs with opposite energies, and so this interaction has an $E \to -E$ symmetry. The large N limit of this theory must be taken while holding g^2N^{12} fixed [73].

This interaction has $O(N)^4$ symmetry. We can study the spectrum of the $q = 8$ model with $O(2)^3 \times O(3)$ symmetry. Here we have 24 Majorana fermions with $2^{12} = 4096$ states. We let the Majorana fermions be the gamma matrices of $SO(24)$, see figure 2.20.

The spectral form factor (SFF) for the $O(2)^4$ and the $O(2)^3 \times O(3)$ models are very similar to those calculated for the rank five MST $q = 6$ model. As expected,

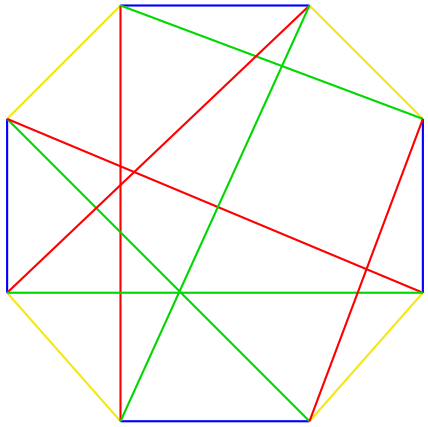

Figure 2.19: A graphical representation of a rank four, $q = 8$ MST interaction.

we do not see a dip-ramp-plateau structure as we can only examine small N due to computability constraints.

Interestingly, working at the classical level where we neglect quantum corrections due to (2.8.4), we find that H_8 is neither invariant nor equal to $-H_8$ under permutation of two of the $O(N)$ groups. This was checked numerically with the assumption that there are only four distinct types of index relabeling in our case of the rank four tensor. These relabelings correspond to the conjugacy classes of S_4, and the number of ways to relabel corresponds to the order of each conjugacy class. The first kind of index relabeling are cycles of size four, for example, we can allow $a_1 \to a_2 \to a_4 \to a_3 \to a_1$. For each index, there are six possible size four cycles. The second kind of relabeling are cycles of size three, for example, we can allow $b_2 \to b_3 \to b_1 \to b_2$. For each index, we have eight possible size three cycles. The third kind of relabeling we have is a pair swap; there are three distinct pair swaps for each index and an example is $c_1 \leftrightarrow c_3$ and $c_2 \leftrightarrow c_4$. The last type of relabeling is a single swap, and there are six possibilities for each index; an example of a single

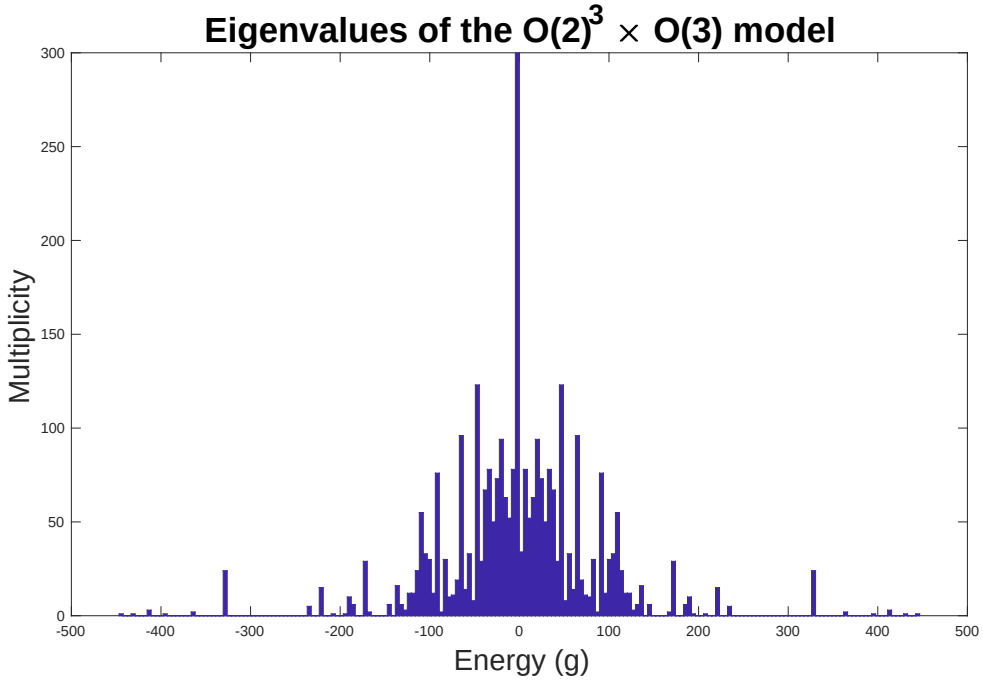

Figure 2.20: Energy spectrum of the rank four, $q = 8$ model with $O(2)^3 \times O(3)$ model. There are 1440 zero energy states; not all are displayed.

swap is $d_2 \leftrightarrow d_3$. Therefore, for each index we have 24 possible relabeling options, including the option of taking no action. We can exchange any two indices, and loop though all possibilities of index relabelings to find that none return the original terms in the Hamiltonian.

In summary, we find that the rank three, $q = 8$ model is invariant under time reversal, and at the classical level has an $O(N)$ group pair swap symmetry that sends $H \to -H$. We do not find either of these properties in the rank four, $q = 8$ model. Additionally, we find that the spectrum of the rank three model is asymmetric, in contrast to that of the rank four model (where the spectral symmetry can be seen through the action of the time reversal operator that sends $H \to -H$).

Chapter 3

Prismatic quantum mechanics with complex fermions

3.1 Introduction

This chapter is based on ongoing work [46]. As discussed in the previous chapters, we know that by suitably choosing the tensor (MST) or SYK interaction, one can produce models with a novel large N limit where the dominant Feynman diagrams are so-called 'melons,' [3, 21, 28, 44, 73–78]. Without the need of introducing quenched disorder, tensor models provide a playground for the $NAdS_2/NCFT_1$ correspondence more similar to its higher dimensional cousins. Regardless of the bulk interpretation, it is interesting to search for possible tensor models with a stable nearly conformal fixed point. While bosonic models are much more natural in $d > 1$, the negative

bare dimension of a boson in $1d$ makes it less desirable than fermionic models.[a] The simplest fermionic tensor model one can write down consists of a real anticommuting ψ^{abc}: $H = g\psi^{abc}\psi^{ab'c'}\psi^{a'bc'}\psi^{a'b'c}$, and it has a stable nearly conformal fixed point in the IR [3]. Fixing the number of $O(N)$ indices, the next interaction that is dominant in the large N limit would be the so-called 'prismatic' interaction

$$O_6 = \psi^{a_1b_1c_1}\psi^{a_1b_2c_2}\psi^{a_2b_1c_2}\psi^{a_3b_3c_1}\psi^{a_3b_2c_3}\psi^{a_2b_3c_3}, \tag{3.1.1}$$

which vanishes due to anticommuting fermions. To avoid that, one can either consider the bosonic version, which has been studied extensively in [74], or consider the complex fermion model.[b]

In our paper, we study a $q = 6$ complex prismatic rank-3 tensor model along with its random counterpart, a $q = 6$ complex fermionic model with a Wishart-Laguerre random coupling. We will call this the $q = 6$ WL-SYK model. To find this WL coupling, we start by constructing the disordered version of our prismatic tensor model. We integrate out the auxiliary field to find a cSYK-like model with a key difference in the coupling term: the random Gaussian coupling is changed to be a product of two Gaussians, $J_{ijkl}J^{\dagger}_{ijkl}$. The tensor model of primary interest to us is the one with $U(1)$ preserving interactions,

$$S = \int dt \left(i\bar{\psi}^{abc}\partial_t\psi^{abc} - \bar{\chi}^{abc}\chi^{abc} + \frac{g}{6}(\psi^{a_1b_1c_1}\psi^{a_1b_2c_2}\psi^{a_2b_1c_2}\bar{\chi}^{a_2b_2c_1} + h.c.)\right), \tag{3.1.2}$$

[a] Known bosonic tensor models in $1d$ are either unstable or have operators with negative scaling dimensions [74].

[b] When working with real fermions, it is natural to consider the 8-fermion interaction, which we shall report elsewhere.

where a complex fermionic auxiliary field is introduced to give rise to the melonic dominance at the price of including an additional field. The disordered (WL-SYK) version of the model,

$$S = \int dt \sum_i \left(\bar{\psi}^i \partial_t \psi^i - \bar{\chi}^i \chi^i + \sum_{1 \leq j \leq k \leq l \leq N} (C_{ijkl} \bar{\chi}^i \psi^j \psi^k \psi^l + h.c.) \right), \tag{3.1.3}$$

shares the same Schwinger-Dyson equations for 2-point and 4-point correlators, and can be naturally viewed as a fermionic version of [79].

Here, we briefly note some differences between the $q = 4$ cSYK model and our $q = 6$ WL-SYK model. For the $q = 4$ cSYK model, the compressibility is found to be a small positive value, $K \approx 1.04$ [36], whereas in our $q = 6$ model we find that K is negative. In contrast to the $q = 4$ cSYK model, we find that our Hamiltonian does not preserve charge conjugation symmetry. In particular, our Hamiltonian is odd under charge conjugation, and the spectrum is symmetric around $E = 0$ as a result. We also find that there is a gap between separating the ground state from the first excited state, which is supported by the exponential decay in the correlation functions.

The paper is organized as follows. In section 3.2 we define the prismatic tensor model along with the analogous random model in section 3.3, and we discuss the continuous and discrete symmetries of both models. In section 3.4, we analyze the large N behavior of the models, working out the conformal solutions and the spectrum of bilinear operators. In section 3.5 we study exact diagonalization results and compute the charge compressibility of our random model.

3.2 Prismatic tensor model

In this section we introduce the unique $O(N)^3$ symmetric prismatic tensor interaction that preserves the $U(1)$ symmetry,

$$\mathcal{L} = i\bar{\psi}^{abc}\partial_t\psi^{abc} + \frac{g}{6}(\psi^{a_1b_1c_1}\psi^{a_1b_2c_2}\psi^{a_2b_1c_2}\bar{\psi}^{a_3b_3c_1}\bar{\psi}^{a_3b_2c_3}\bar{\psi}^{a_2b_3c_3} + h.c.). \tag{3.2.1}$$

This interaction is called prismatic, because the graph (where each vertex represents a fermion and each colored edge represents a shared index between two fermions) looks like a prism, see figure 3.2. At the classical level, where we ignore the anti-commutation relations, we find that the Hamiltonian,

$$H = \frac{g}{6}(\psi^{a_1b_1c_1}\psi^{a_1b_2c_2}\psi^{a_2b_1c_2}\bar{\psi}^{a_3b_3c_1}\bar{\psi}^{a_3b_2c_3}\bar{\psi}^{a_2b_3c_3} + h.c.), \tag{3.2.2}$$

is invariant under the exchange of any pair of $O(N)$ groups. For example, we can swap $O_a(N) \leftrightarrow O_c(N)$ such that $\psi^{abc} \leftrightarrow \psi^{cba}$, and so we have,

$$H_{a\leftrightarrow c} = \frac{g}{6}(\psi^{a_1b_1c_1}\psi^{a_2b_2c_1}\psi^{a_2b_1c_2}\bar{\psi}^{a_1b_3c_3}\bar{\psi}^{a_3b_2c_3}\bar{\psi}^{a_3b_3c_2} + h.c.). \tag{3.2.3}$$

We can exchange indices $a_1 \leftrightarrow a_2$ and $c_1 \leftrightarrow c_2$ to find the original terms in the Hamiltonian,

$$H_{a\leftrightarrow c} = \frac{g}{6}(\psi^{a_2b_1c_2}\psi^{a_1b_2c_2}\psi^{a_1b_1c_1}\bar{\psi}^{a_2b_3c_3}\bar{\psi}^{a_3b_2c_3}\bar{\psi}^{a_3b_3c_1} + h.c.). \tag{3.2.4}$$

Through making an even number of exchanges, we find that $H = H_{a\leftrightarrow c}$, and this is also the case with the other possible $O(N)$ group permutations. Thus we find that there is a discrete S_3 symmetry associated with permuting $O(N)$ groups. In addition to this discrete $O(N)$ swapping symmetry, we also find that charge conjugation, where $\psi^{abc} \leftrightarrow \bar{\psi}^{abc}$, maps $H \to -H$ as seen in figure 3.1.

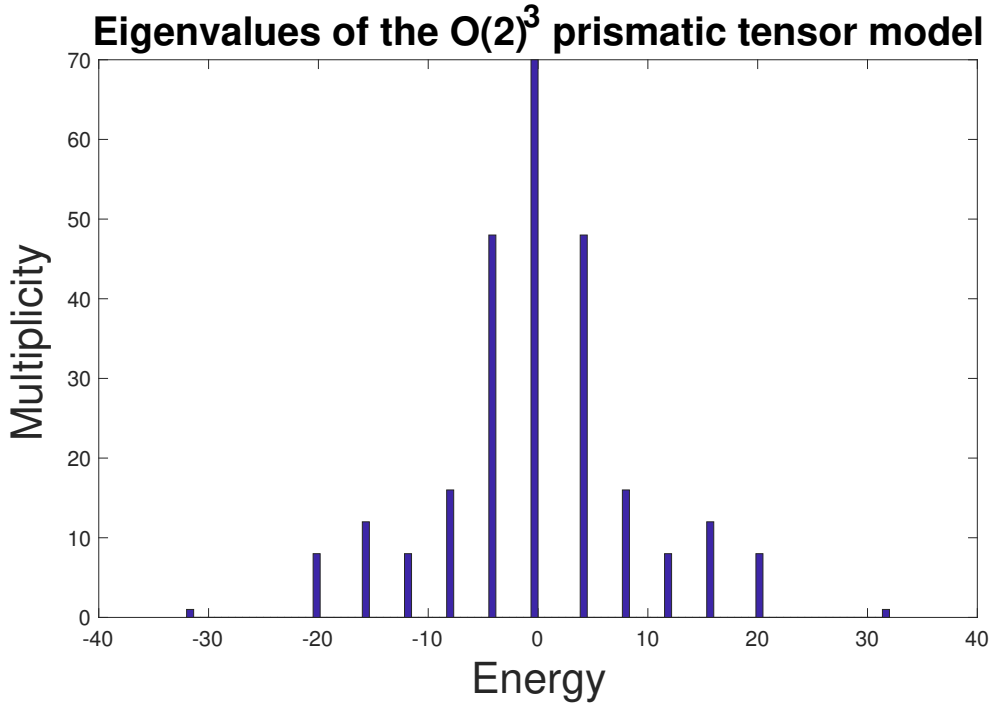

Figure 3.1: The full spectrum of the $O(2)^3$ prismatic tensor model, see equation (3.2.2).

By introducing an auxiliary field χ^{abc}, whose bare propagator is merely a contact term, we can rewrite the model with tetrahedron interaction,

$$\mathcal{L} = i\bar{\psi}^{abc}\partial_t\psi^{abc} - \bar{\chi}^{abc}\chi^{abc} + \frac{g}{6}(\psi^{a_1b_1c_1}\psi^{a_1b_2c_2}\psi^{a_2b_1c_2}\bar{\chi}^{a_2b_2c_1} + h.c.). \tag{3.2.5}$$

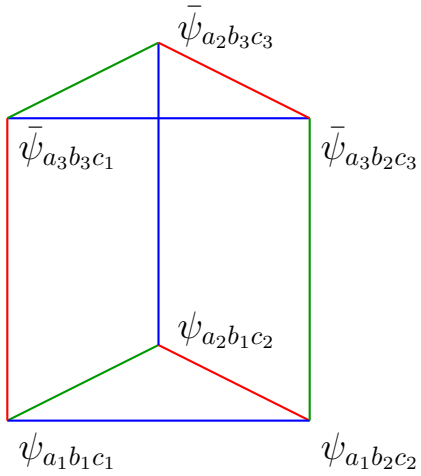

Figure 3.2: The graph that corresponds to the prismatic tensor interaction.

This model has a scaling symmetry in the IR and in addition to the $U(1)$ symmetry,

$$U(1) : \psi^{abc} \to e^{i\alpha}\psi^{abc},\ \chi^{abc} \to e^{-3i\alpha}\chi^{abc}, \quad \text{Scaling} : \psi^{abc} \to \lambda\psi^{abc},\ \chi^{abc} \to \lambda^{-3}\chi^{abc}. \tag{3.2.6}$$

3.3 Random model

In this section we consider the random version of the prismatic model introduced in section 3.2.

$$\mathcal{L} = -\bar{\psi}^i\partial_t\psi^i + \frac{J_{ijkl}}{3!}\psi^i\psi^j\psi^k\bar{\chi}^l + \frac{\bar{J}_{ijkl}}{3!}\bar{\psi}^i\bar{\psi}^j\bar{\psi}^k\chi^l + \bar{\chi}^i\chi^i, \tag{3.3.1}$$

where J_{ijkl} is a complex random variable, with the indices i, j, and k fully anti-symmetric. To construct J_{ijkl}, we start with a complex random variable T_{ijkl} such

that $\langle T_{ijkl}\bar{T}_{i'j'k'l'}\rangle \sim \delta_{i,i'}\delta_{j,j'}\delta_{k,k'}\delta_{l,l'}$. We let J_{ijkl} be equal to,

$$\sum_{\sigma\in S_3} \text{sign}(\sigma)\left(a_1 T_{\sigma(i),\sigma(j),\sigma(k),l} + a_2 T_{l,\sigma(i),\sigma(j),\sigma(k)} + a_3 T_{\sigma(i),l,\sigma(j),\sigma(k)} + a_4 T_{\sigma(i),\sigma(j),l,\sigma(k)}\right). \tag{3.3.2}$$

We find that there is one degree of freedom in J_{ijkl}, as

$$\begin{aligned}&\langle \bar{J}_{ijkl}J_{i'j'k'l'}\rangle \sim 6\left(a_1^*a_1 + a_2^*a_2 + a_3^*a_3 + a_4^*a_4\right)\left(\delta_{i,i'}\delta_{j,j'}\delta_{k,k'}\delta_{l,l'} + \dots\right) + \\ &2\left(a_1^*a_2 + a_1a_2^* - a_1^*a_3 + a_2^*a_3 - a_1a_3^* + a_2a_3^* + a_1^*a_4 - a_2^*a_4 + a_3^*a_4 + a_1a_4^* - a_2a_4^* + a_3a_4^*\right) \\ &\left(\delta_{i,l'}\delta_{j,j'}\delta_{k,k'}\delta_{l,i'} + \dots\right).\end{aligned} \tag{3.3.3}$$

Upon normalizing J, we may define

$$\kappa = \frac{2(a_2(a_3 - a_4 + 1) + a_3(a_4 - 1) + a_4)}{3\left(a_2^2 + a_3^2 + a_4^2 + 1\right)}, \tag{3.3.4}$$

where without loss of generality, we set $a_1 = 1$, and $a_i \in \mathbb{R}$. The κ admits range between -1 and $\frac{1}{3}$. We let the random variable obey,

$$\langle \bar{J}_{ijkl}J_{i'j'k'l'}\rangle = \frac{J^2}{6N^3}\left(\delta_{i,i'}\delta_{j,j'}\delta_{k,k'}\delta_{l,l'} + \dots + \kappa\delta_{i,l'}\delta_{j,j'}\delta_{k,k'}\delta_{l,i'} + \dots\right). \tag{3.3.5}$$

We integrate out the random coupling, to obtain a bilocal action that describes the theory:

$$\begin{aligned} S = &- \int dt \left(\bar{\psi} \partial_t \psi + \bar{\chi} \chi \right) \\ &- J^2 \int dt dt' \left(\psi^i \psi^j \psi^k \bar{\chi}^l(t) \bar{\psi}^i \bar{\psi}^j \bar{\psi}^k \chi^l(t') + 3\kappa \psi^i \psi^j \psi^k \bar{\chi}^l(t) \bar{\psi}^l \bar{\psi}^j \bar{\psi}^k \chi^i(t') \right) . \end{aligned} \tag{3.3.6}$$

The model has $U(1)$ symmetry with

$$\psi \to e^{i\alpha} \psi, \quad \chi \to e^{-3i\alpha} \chi, \tag{3.3.7}$$

and in the IR, the second line in (3.3.6) dominates. The model has enhanced diffeomorphism symmetry, and becomes nearly conformal. There is also an additional scaling symmetry:

$$\psi \to \lambda \psi, \quad \chi \to \lambda^{-3} \chi, \tag{3.3.8}$$

and as a result, we expect that there is a $h = 1$ operator in the conformal spectrum of the model.

3.4 Conformal solution

In this section, we consider the conformal solution, where the off-diagonal correlator is set to zero. We denote $G_\psi(t) = \frac{1}{N} \langle \bar{\psi}^i(t) \psi^i(0) \rangle$ and $G_\chi(t) = \frac{1}{N} \langle \bar{\chi}^i(t) \chi^i(0) \rangle$. The conformal solution turns out to be tricky, and so we will explain it in detail. We note that the interaction in (3.3.1) needs to be marginal in the infrared, so it is necessary that $3\Delta_\psi + \Delta_\chi = 1$. Since we have introduced the auxiliary field, χ, we

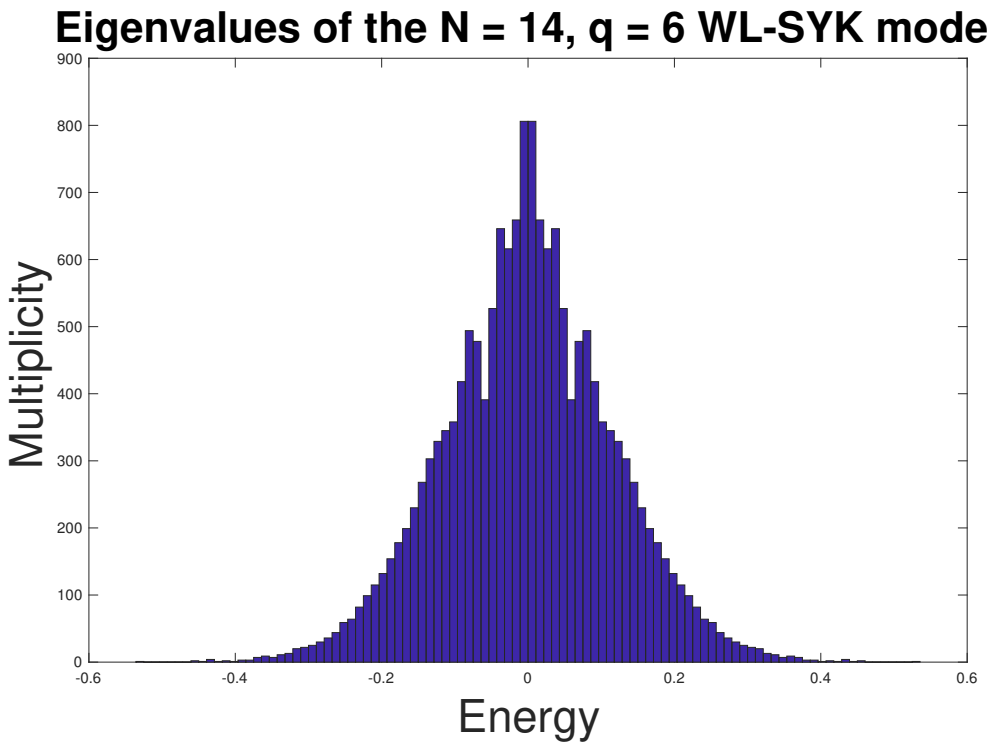

Figure 3.3: The full spectrum of the $N = 14$, $q = 6$ WL-SYK model, see equation (3.3.1).

have a tetrahedral interaction and thus we have melonic dominance. We can write the Schwinger-Dyson equations,

$$G_\psi(t) = \langle \bar{\psi}\psi \rangle = \frac{\text{sign}(t)}{\partial_t - \Sigma_\psi(t)}, \quad G_\chi(t) = \langle \bar{\chi}\chi \rangle = \frac{\text{sign}(t)}{1 - \Sigma_\chi(t)}, \tag{3.4.1}$$

$\Sigma_\psi(t) =$  $= 3\lambda^2 G_\psi(t)^2 G_\chi(t), \quad \Sigma_\chi(t) =$ 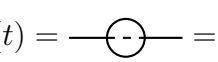 $= \lambda^2 G_\psi(t)^3.$ (3.4.2)

The dashed lines represent the χ propagator, and $\lambda^2 = g^2 N^3$ for the tensor model and $\lambda^2 = J^2$ for the WL-SYK model. In the IR limit, we can drop the free terms,

and make the following ansatz:

$$G_\psi(t) = \frac{b_\psi \text{sign}(t)}{|t|^{2\Delta_\psi}}, \quad G_\chi(t) = \frac{b_\chi \text{sign}(t)}{|t|^{2\Delta_\chi}}. \tag{3.4.3}$$

Note that the unitarity bound requires $0 \leq \Delta_\psi \leq \frac{1}{3}$, and in order for the conformal approximation to be valid, we need $\frac{1}{6} < \Delta_\psi \leq \frac{1}{3}$.

The ansatz (3.4.3) assumes a particular symmetry of the correlator: $G(t) = -G(-t)$. Such an assumption relies on the charge conjugation symmetry. Indeed, if the ground state is charge conjugation invariant, for $t > 0$,

$$G(t) = \langle \bar{\psi}(t)\psi(0)\rangle = \langle \psi(t)\bar{\psi}(0)\rangle = \langle \psi(0)\bar{\psi}(-t)\rangle = -G(-t). \tag{3.4.4}$$

However, the model (3.3.1) explicitly breaks the charge conjugation symmetry by the mass term of χ. Nevertheless, in the IR, this term is absent. We take the Fourier transform of (3.4.3), and work in dimension $d = 1$.

$$\begin{aligned} G_\psi(p) &= \int dt \, \frac{e^{ipt}\text{sign}(t) b_\psi}{|t|^{2\Delta_\psi}} \\ &= 2ib_\psi |p|^{2\Delta_\psi - 1} \cos(\Delta_\psi \pi)\Gamma(1 - 2\Delta_\psi)\text{sign}(p). \end{aligned} \tag{3.4.5}$$

Then we can use the relationship $G_{\psi/\chi} = -1/\Sigma_{\psi/\chi}$ to get an expression for $\Sigma_{\psi/\chi}$ in momentum space. Finally, we can Fourier transform back to position space to get

the following expression:

$$\begin{aligned}\Sigma_\psi(t) &= -\int \frac{dp}{2\pi} \frac{-e^{ipt}}{2ib_\psi |p|^{2\Delta_\psi - 1}\cos(\Delta_\psi \pi)\Gamma(1-2\Delta_\psi)\text{sign}(p)} \\ &= \frac{|t|^{2\Delta_\psi - 2}\Gamma(2-2\Delta_\psi)\text{sign}(t)\tan(\Delta_\psi \pi)}{2\pi b_\psi \Gamma(1-2\Delta_\psi)} \\ &= \frac{|t|^{2\Delta_\psi - 2}(1-2\Delta_\psi)\text{sign}(t)\tan(\Delta_\psi \pi)}{2\pi b_\psi}.\end{aligned} \tag{3.4.6}$$

We have similar equations for $\Sigma_\chi(t)$ except with b_χ instead of b_ψ, and Δ_χ instead of Δ_ψ. Simplifying by combining (3.4.2) and (3.4.6), and by using the relationship $\Delta_\chi = 1 - 3\Delta_\psi$, we get:

$$\lambda^2 b_\psi^3 b_\chi = \frac{(1-2\Delta_\psi)\tan(\Delta_\psi \pi)}{6\pi}, \tag{3.4.7}$$

$$\lambda^2 b_\psi^3 b_\chi = \frac{(6\Delta_\psi - 1)\tan(\pi(1-3\Delta_\psi))}{2\pi}. \tag{3.4.8}$$

Now we combine equations (3.4.7) and (3.4.8), and simplify the ratios of gamma functions to get our final transcendental equation for the scaling dimension of ψ in dimension $d = 1$:

$$\begin{aligned}1 &= \frac{\Gamma(2-2\Delta_\psi)\Gamma(6\Delta_\psi - 1)}{3\,\Gamma(6\Delta_\psi)\Gamma(1-2\Delta_\psi)} \\ &= \frac{(1-2\Delta_\psi)\tan(\Delta_\psi \pi)}{3\,(6\Delta_\psi - 1)\tan(\pi(1-3\Delta_\psi))}.\end{aligned} \tag{3.4.9}$$

We can solve (3.4.9) numerically to get the allowed values of Δ_ψ, see figure 3.4. Our first solution is at $\Delta_\psi \approx 0.311$ and $\Delta_\chi \approx 0.068$, as shown in figure 3.4.

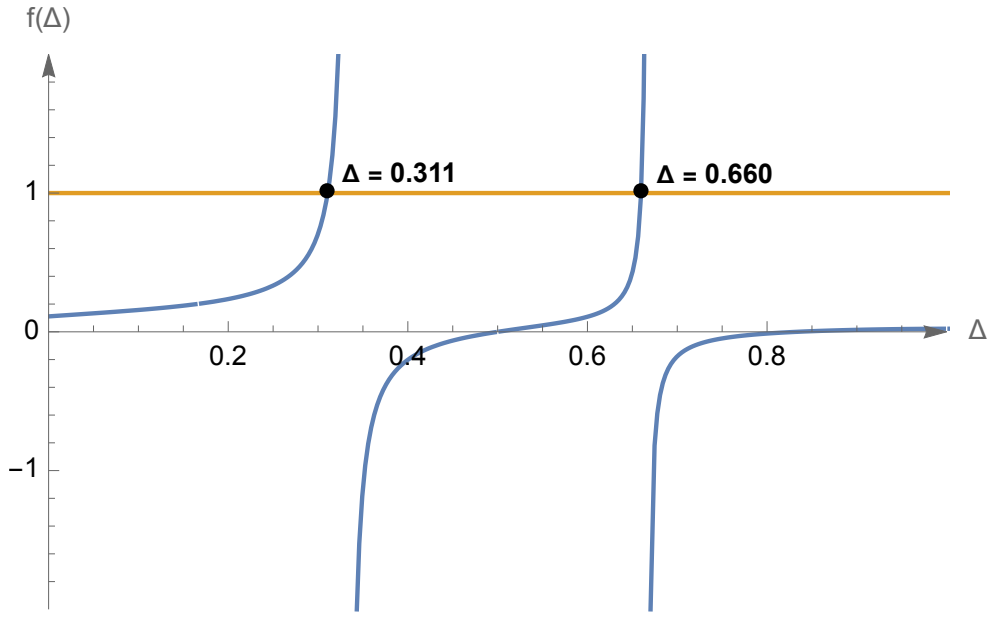

Figure 3.4: The numerical solution to equation (3.4.9). Here we simplified notation such that $\Delta = \Delta_\psi$. Note that $\Delta_\psi = 1/6$ is not a solution here.

There is another solution in the IR if we assume the bare kinetic term of χ, which produces a shift in momentum space, is not negligible. On dimensional grounds, it necessarily implies $\Delta_\chi = \frac{1}{2}$, and $\Delta_\psi = \frac{1}{6}$. We now show that is consistent. We rewrite the momentum space equation,

$$\frac{1}{-iw - \Sigma_\psi(w)} = -G_\psi(-w), \quad \frac{1}{-1 - \Sigma_\chi(w)} = -G_\chi(-w), \tag{3.4.10}$$

and we note that when $\Delta_\chi = \frac{1}{2}$, $\Sigma_\chi(w) \sim \mathcal{O}(1)$, and the bare term is not negligible, whereas $\Sigma_\psi(w) \sim \mathcal{O}\left(|w|^{\frac{2}{3}}\right)$, and the kinetic term is of a higher order in the IR.

Therefore we may solve,

$$\Sigma_\psi(w)G_\psi(w) = -1, \quad (1+\Sigma_\chi(w))G_\chi(w) = -1. \tag{3.4.11}$$

We now consider the following conformal ansatz,

$$G_\psi(t) = \frac{b_\psi \text{sign}(t)}{|t|^{2\Delta_\psi}}, \quad G_\chi(t) = a\delta(t) + \frac{b_\chi \text{sign}(t)}{|t|^{2\Delta_\chi}}. \tag{3.4.12}$$

We take the Fourier transform of (3.4.12) to get,

$$G_\psi(p) = 2ib_\psi |p|^{2\Delta_\psi - 1}\cos(\Delta_\psi \pi)\Gamma(1-2\Delta_\psi)\text{sign}(p), \tag{3.4.13}$$

$$G_\chi(p) = a + 2ib_\chi |p|^{2\Delta_\chi - 1}\cos(\Delta_\chi \pi)\Gamma(1-2\Delta_\chi)\text{sign}(p). \tag{3.4.14}$$

Next, we find the self energy in position space. The expression for $\Sigma_\psi(t)$ is exactly the same as in equation (3.4.6). We write the expression for $\Sigma_\chi(t)$ below:

$$\begin{aligned}\Sigma_\chi(t) &= \int \frac{dp}{2\pi}\left(e^{-ipt} - e^{-ipt}/G_\chi(p)\right) \\ &= \delta(t) - \int \frac{dp}{2\pi} e^{-ipt}\left(a + 2ib_\chi |p|^{2\Delta_\chi - 1}\cos(\Delta_\chi\pi)\Gamma(1-2\Delta_\chi)\text{sign}(p)\right)^{-1}.\end{aligned}$$

We simplify the above expression for $\Sigma_\chi(t)$ by setting $\Delta_\chi = 1/2$, and so $\cos(\Delta_\chi\pi)\Gamma(1-2\Delta_\chi) \to \pi/2$.

$$\begin{aligned}
\Sigma_\chi(t) &= \delta(t) - \int \frac{dp}{2\pi} e^{-ipt} \left(a + i\pi b_\chi \text{sign}(p)\right)^{-1} \\
&= \delta(t) - \frac{1}{a^2 + b_\chi^2\pi^2} \int \frac{dp}{2\pi} e^{-ipt} \left(a - i\pi b_\chi \text{sign}(p)\right) \\
&= \delta(t) - \frac{a\,\delta(t)}{a^2 + b_\chi^2\pi^2} + \frac{1}{a + b_\chi^2\pi^2} \int \frac{dp}{2\pi} e^{-ipt} \left(i\pi b_\chi \text{sign}(p)\right) \\
&= \delta(t) - \frac{a}{a^2 + b_\chi^2\pi^2} \left(\delta(t) - \frac{b_\chi \text{sign}(t)}{a\,|t|}\right).
\end{aligned} \tag{3.4.15}$$

Now we may express the self energy using equation (3.4.2) along with expression (3.4.15),

$$\Sigma_\chi(t) = \lambda^2 \frac{b_\psi^3 \text{sign}(t)}{|t|^{6\Delta_\psi}} = \delta(t) - \frac{a}{a^2 + b_\chi^2\pi^2} \left(\delta(t) - \frac{b_\chi \text{sign}(t)}{a\,|t|}\right), \tag{3.4.16}$$

$$\Sigma_\psi(t) = 3\lambda^2 \frac{b_\psi^2}{|t|^{4\Delta_\psi}} \left(a\delta(t) + \frac{b_\chi \text{sign}(t)}{|t|^{2\Delta_\chi}}\right) = \frac{|t|^{2\Delta_\psi - 2}(1 - 2\Delta_\psi)\text{sign}(t)\tan(\Delta_\psi\pi)}{2\pi b_\psi}. \tag{3.4.17}$$

We allow $\Delta_\chi = 1/2$ and $\Delta_\psi = 1/6$ to simplify,

$$\Sigma_\chi(t) = \lambda^2 \frac{b_\psi^3 \text{sign}(t)}{|t|} = \delta(t) - \frac{a}{a^2 + b_\chi^2\pi^2} \left(\delta(t) - \frac{b_\chi \text{sign}(t)}{a\,|t|}\right), \tag{3.4.18}$$

$$\Sigma_\psi(t) = 3\lambda^2 \frac{b_\psi^2}{|t|^{2/3}} \left(a\delta(t) + \frac{b_\chi \text{sign}(t)}{|t|}\right) = \frac{\text{sign}(t)}{3\sqrt{3}\pi b_\psi |t|^{5/3}}. \tag{3.4.19}$$

We can find the constraints on the coefficients by solving equations (3.4.18) and (3.4.19), and we note that the $\delta(t)$ term in equation (3.4.19) does not contribute in

dimensional regularization, and so we neglect it while solving for the constraints. The constraints are,

$$\frac{a}{a^2+b_\chi^2\pi^2}=1, \quad \lambda^2 b_\psi^3=\frac{b_\chi}{a^2+b_\chi^2\pi^2}, \quad 3\lambda^2 b_\psi^3 b_\chi=\frac{1}{3\sqrt{3}\pi}. \tag{3.4.20}$$

We can solve the above system of equations to find the values for a, b_χ, b_ψ,

$$a=\frac{9\sqrt{3}-\pi}{9\sqrt{3}}, \quad b_\chi^2=\frac{9\sqrt{3}-\pi}{\pi(9\sqrt{3})^2}, \quad b_\psi^3=\frac{\lambda^{-2}}{\sqrt{\pi(9\sqrt{3}-\pi)}}. \tag{3.4.21}$$

Now we may write the expressions for $G_\psi(t)$ and $G_\chi(t)$, combining equations (3.4.12) and (3.4.21),

$$G_\psi(t)=\left(\frac{\lambda^{-2}}{\sqrt{\pi(9\sqrt{3}-\pi)}}\right)^{1/3}\frac{\text{sign}(t)}{|t|^{1/3}}, \tag{3.4.22}$$

$$G_\chi(t)=\frac{9\sqrt{3}-\pi}{9\sqrt{3}}\delta(t)+\frac{\sqrt{9\sqrt{3}-\pi}}{9\sqrt{3\pi}}\frac{\text{sign}(t)}{|t|}, \tag{3.4.23}$$

where we let $\Delta_\psi=1/6$ and $\Delta_\chi=1/2$. The finite temperature solutions are included below,

$$G_\psi(\tau)=\frac{\lambda^{-\frac{2}{3}}}{(\pi(9\sqrt{3}-\pi))^{\frac{1}{6}}}\left[\frac{\pi}{\beta\sin\frac{\pi\tau}{\beta}}\right]^{\frac{1}{3}}\text{sign}(\tau), \tag{3.4.24}$$

$$G_\chi(\tau)=\sqrt{\frac{9\sqrt{3}-\pi}{\pi(9\sqrt{3})^2}}\left[\frac{\pi}{\beta\sin\frac{\pi\tau}{\beta}}\right]\text{sign}(\tau)+\left(1-\frac{\pi}{9\sqrt{3}}\right)\frac{\beta\delta(\tau)}{\pi}. \tag{3.4.25}$$

3.4.1 Spectrum of bilinears

In this section, for ease of notation, we let $\Delta = \Delta_\psi$, and so $\Delta_\chi = 1 - 3\Delta$. We consider the $U(1)$ neutral sector first, examining the matrix elements $\left\langle \mathcal{O}^n_\psi(t_0)\bar{\psi}^{abc}(t_1)\psi^{abc}(t_2)\right\rangle$, $\left\langle \mathcal{O}^n_\chi(t_0)\bar{\psi}^{abc}(t_1)\psi^{abc}(t_2)\right\rangle$, and $\left\langle \mathcal{O}^n_\psi(t_0)\bar{\chi}^{abc}(t_1)\chi^{abc}(t_2)\right\rangle$. We can also consider bilinear operators in the $U(1)$ charged sector, like the matrix element $\left\langle \mathcal{O}^n_{\psi\chi}(t_0)\psi^{abc}(t_1)\chi^{abc}(t_2)\right\rangle$. Throughout this section, we use the following relations and notations as used in reference [3] to simplify our expressions,

$$\begin{aligned} l^{\pm}_{x,y} &= \beta(1-x, x+y-1) \pm \left(\beta(1-y, x+y-1) - \beta(1-x, 1-y)\right), \\ \int du\, &\frac{\text{sign}(u-t_1)\text{sign}(u-t_2)}{|u-t_1|^a|u-t_2|^b} = l^+_{a,b}\frac{1}{|t_{12}|^{a+b-1}}, \\ \int du\, &\frac{\text{sign}(u-t_2)}{|u-t_1|^a|u-t_2|^b} = l^-_{a,b}\frac{\text{sign}(t_{12})}{|t_{12}|^{a+b-1}}. \end{aligned} \tag{3.4.26}$$

where $\beta(x,y) = \Gamma(x)\Gamma(y)/\Gamma(x+y)$ and $t_{12} = t_1 - t_2$.

3.4.1.1 $U(1)$ neutral sector

To find the spectrum of bilinears, we would like to solve the following integral eigenvalue equation:

$$g(h)v(t_0,t_1,t_2) = \int dt_3 dt_4 K(t_1,t_2;t_3,t_4)v(t_0,t_3,t_4), \tag{3.4.27}$$

where the kernel $K(t_1,t_2;t_3,t_4)$ is given by a 2×2 matrix with entries corresponding to each four point interaction of (3.2.5).

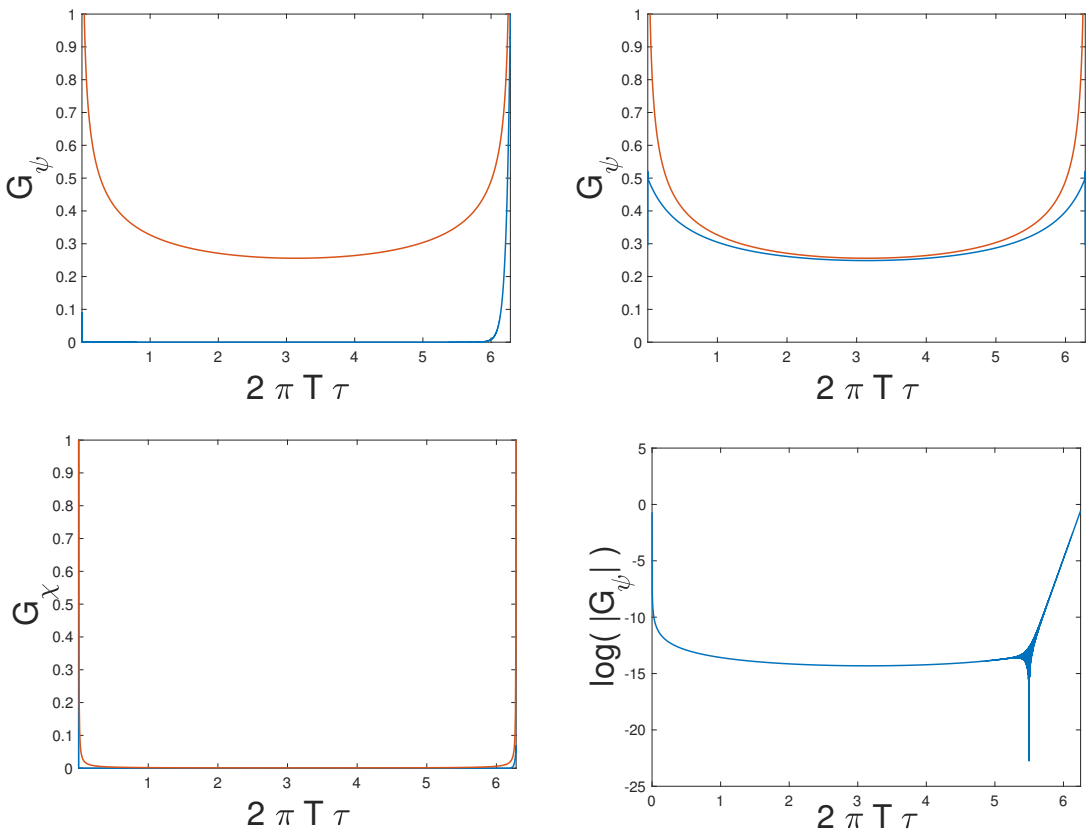

Figure 3.5: Left column: The numerical solutions of the SD equations for G_ψ (top) and G_χ (bottom) with no allowed off diagonal correlators (3.4.1) and (3.4.2) with $\beta\lambda = 120$ in blue, compared to the finite temperature solutions found in equations (3.4.24) and (3.4.25), in red. The reason why the solutions in blue and red do not agree, particularly for G_ψ, is because the conformal solution is unstable and is likely not the real solution when we numerically solve the SD equations. Top right: The SD solution with an added constraint such that the ground state is in the $Q = 0$ charge sector. Bottom right: The log plot of G_ψ with no symmetry constraints enforced. The linear portion indicates the exponential decay of the Green's function.

$$K = \left[\begin{array}{cc} \text{ 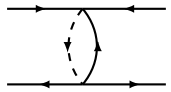 } & \text{ 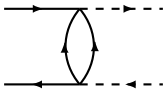 } \\ \text{ 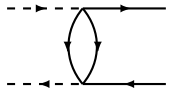 } & \text{no contributing diagram} \end{array} \right] \tag{3.4.28}$$

$$= \begin{bmatrix} 6\lambda^2 G_\psi(t_{13}) G_\psi(t_{24}) G_\psi(t_{34}) G_\chi(t_{34}) & -3\lambda^2 G_\psi(t_{14}) G_\psi(t_{23}) G_\psi(t_{34})^2 \\ 3\lambda^2 G_\chi(t_{14}) G_\chi(t_{23}) G_\psi(t_{34})^2 & 0 \end{bmatrix},$$

where the top left entry is $\bar{\psi}\psi \to \bar{\psi}\psi$, the top right is $\bar{\psi}\psi \to \bar{\chi}\chi$, and the bottom left is $\bar{\chi}\chi \to \bar{\psi}\psi$. The bottom right contribution to $\bar{\chi}\chi \to \bar{\chi}\chi$ is not allowed given the interaction term, and so its kernel element is zero. From the previous section, we know the propagators have the form,

$$\begin{aligned} G_\psi(t) &= \frac{b_\psi \text{sign(t)}}{|t|^{2\Delta}}, \\ G_\chi(t) &= a\delta(t) + \frac{b_\chi \text{sign(t)}}{|t|^{2\Delta_\chi}} = a\delta(t) + \frac{b_\chi \text{sign(t)}}{|t|^{2-6\Delta}}. \end{aligned}$$

In the second line, we used the relationship $\Delta_\chi = 1 - 3\Delta$. We can find the kernel elements in the antisymmetric or symmetric sector. In the antisymmetric sector, the conformal vectors have the form,

$$\begin{aligned} v_{\bar{\psi}\psi}(t_0, t_1, t_2) &= \frac{\text{sign}(t_{12})}{|t_{12}|^{2\Delta - h}}, \\ v_{\bar{\chi}\chi}(t_0, t_1, t_2) &= \frac{\text{sign}(t_{12})}{|t_{12}|^{2-6\Delta - h}}, \end{aligned} \tag{3.4.29}$$

where above we have used $SL(2)$ invariance to send t_0 to infinity. First, let us calculate the contribution from the $\bar{\psi}\psi \to \bar{\chi}\chi$ diagram. We need to integrate,

$$\begin{aligned} &-3\lambda^2 \int dt_3 dt_4 G_\psi(t_{14}) G_\psi(t_{23}) G_\psi(t_{34})^2 v_{\bar{\chi}\chi}(t_0, t_3, t_4) \\ &= -3\lambda^2 \int dt_3 dt_4 \frac{b_\psi^4 \text{sign}(t_{14})\text{sign}(t_{23})\text{sign}(t_{34})}{|t_{14}|^{2\Delta}|t_{23}|^{2\Delta}|t_{34}|^{2-2\Delta-h}} \\ &= 3\lambda^2 b_\psi^4 l^+_{2\Delta,2-2\Delta-h} l^-_{1-h,2\Delta} \frac{\text{sign}(t_{12})}{|t_{12}|^{2\Delta-h}}. \end{aligned} \tag{3.4.30}$$

Next we will evaluate the $\bar{\psi}\psi \to \bar{\psi}\psi$ diagram.

$$\begin{aligned} &6\lambda^2 \int dt_3 dt_4 G_\psi(t_{13}) G_\psi(t_{24}) G_\psi(t_{34}) G_\chi(t_{34}) v_{\bar{\psi}\psi}(t_0, t_3, t_4) \\ &= 6\lambda^2 \int dt_3 dt_4 \frac{b_\psi^3 b_\chi \text{sign}(t_{13})\text{sign}(t_{24})\text{sign}(t_{34})}{|t_{13}|^{2\Delta}|t_{24}|^{2\Delta}|t_{34}|^{2-2\Delta-h}} \\ &= -6\lambda^2 b_\psi^3 b_\chi l^+_{2\Delta,2-2\Delta-h} l^-_{1-h,2\Delta} \frac{\text{sign}(t_{12})}{|t_{12}|^{2\Delta-h}}. \end{aligned} \tag{3.4.31}$$

For the $\bar{\chi}\chi \to \bar{\psi}\psi$ diagram, we will have contributions from the contact term in the $\bar{\chi}\chi$ propagator.

$$\begin{aligned} &3\lambda^2 \int dt_3 dt_4 G_\chi(t_{14}) G_\chi(t_{23}) G_\psi(t_{34})^2 v_{\bar{\psi}\psi}(t_0, t_3, t_4) \\ &= 3\lambda^2 \int dt_3 dt_4 (a\delta(t_{14}) + \frac{b_\chi \text{sign}(t_{14})}{|t_{14}|^{2-6\Delta}})(a\delta(t_{23}) + \frac{b_\chi \text{sign}(t_{23})}{|t_{23}|^{2-6\Delta}}) \frac{b_\psi^2 \text{sign}(t_{34})}{|t_{34}|^{6\Delta-h}} \\ &= -3\lambda^2 a^2 b_\psi^2 \frac{\text{sign}(t_{12})}{|t_{12}|^{6\Delta-h}} - 3\lambda^2 b_\psi^2 b_\chi^2 l^+_{2-6\Delta,6\Delta-h} l^-_{1-h,2-6\Delta} \frac{\text{sign}(t_{12})}{|t_{12}|^{2-6\Delta-h}}. \end{aligned} \tag{3.4.32}$$

Now we can solve for $g(h)$ and get that, in the antisymmetric case,

$$\begin{aligned} g(h)_{(1,1)} &= -6\lambda^2 b_\psi^3 b_\chi l^+_{2\Delta,2-2\Delta-h} l^-_{1-h,2\Delta}, \\ g(h)_{(1,2)} &= 3\lambda^2 b_\psi^4 l^+_{2\Delta,2-2\Delta-h} l^-_{1-h,2\Delta}, \\ g(h)_{(2,1)} &= -3\lambda^2 a^2 b_\psi^2 - 3\lambda^2 b_\psi^2 b_\chi^2 l^+_{2-6\Delta,6\Delta-h} l^-_{1-h,2-6\Delta}. \end{aligned} \tag{3.4.33}$$

We can find the eigenvalues of $g(h)$ and set one of them equal to 1 to find the scaling dimensions of the bilinears. This is equivalent to the condition,

$$\det = \begin{bmatrix} g(h)_{(1,1)} - 1 & g(h)_{(1,2)} \\ g(h)_{(2,1)} & -1 \end{bmatrix} = 0. \tag{3.4.34}$$

Thus, we find the following constraint for h and can see that it is symmetric under $h \to 1 - h$.

$$1 = -6\lambda^2 b_\psi^3 b_\chi l^+_{2\Delta,2-2\Delta-h} l^-_{1-h,2\Delta} - 9\lambda^4 b_\psi^6 l^+_{2\Delta,2-2\Delta-h} l^-_{1-h,2\Delta} \left(a^2 + b_\chi^2 l^+_{2-6\Delta,6\Delta-h} l^-_{1-h,2-6\Delta}\right). \tag{3.4.35}$$

In the antisymmetric case, we verify that $h = 2$ is a solution, see figure 3.6.

Similarly, we can consider the symmetric sector with conformal vectors,

$$\begin{aligned} v_{\bar\psi\psi}(t_0, t_1, t_2) &= \frac{1}{|t_{12}|^{2\Delta-h}}, \\ v_{\bar\chi\chi}(t_0, t_1, t_2) &= \frac{1}{|t_{12}|^{2-6\Delta-h}}. \end{aligned} \tag{3.4.36}$$

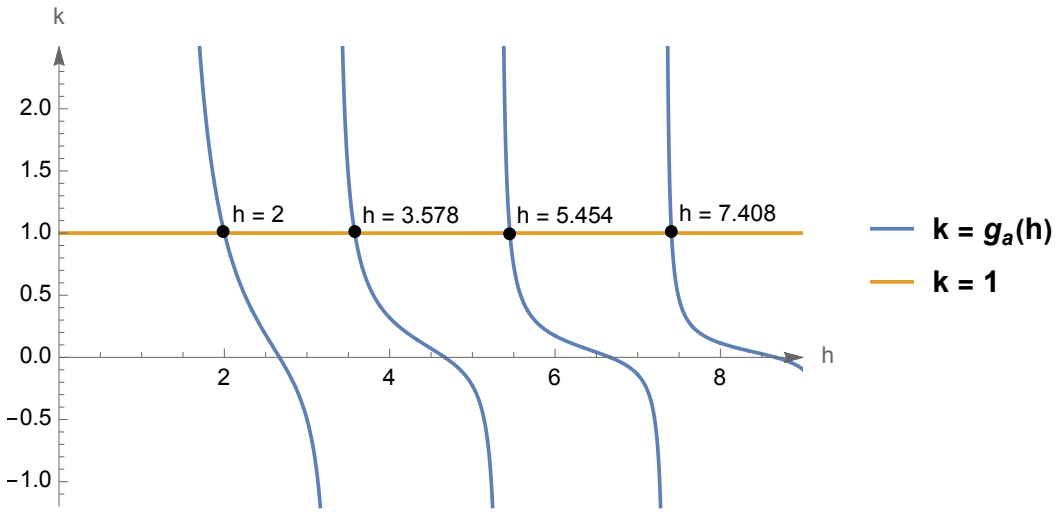

Figure 3.6: The dimensions of $U(1)$ neutral bilinear operators in the antisymmetric sector of the prismatic tensor model. We note that $h = 2$ is the first solution.

We find that the corresponding $g(h)$ matrix elements for the symmetric case are,

$$\begin{aligned} g(h)_{(1,1)} &= 6\lambda^2 b_\psi^3 b_\chi l^+_{2\Delta,1-h} l^-_{2-2\Delta-h,2\Delta}, \\ g(h)_{(1,2)} &= -3\lambda^2 b_\psi^4 l^+_{2\Delta,1-h} l^-_{2-2\Delta-h,2\Delta}, \\ g(h)_{(2,1)} &= 3\lambda^2 a^2 b_\psi^2 + 3\lambda^2 b_\psi^2 b_\chi^2 l^+_{2-6\Delta,1-h} l^-_{6\Delta-h,2-6\Delta}. \end{aligned} \tag{3.4.37}$$

In this case, the constraint on h is,

$$1 = 6\lambda^2 b_\psi^3 b_\chi l^+_{2\Delta,1-h} l^-_{2-2\Delta-h,2\Delta} - 9\lambda^4 b_\psi^6 l^+_{2\Delta,1-h} l^-_{2-2\Delta-h,2\Delta} \left(a^2 + b_\chi^2 l^+_{2-6\Delta,1-h} l^-_{6\Delta-h,2-6\Delta}\right). \tag{3.4.38}$$

Here, we expect and verify that there is a solution at $h = 1$, see figure 3.7.

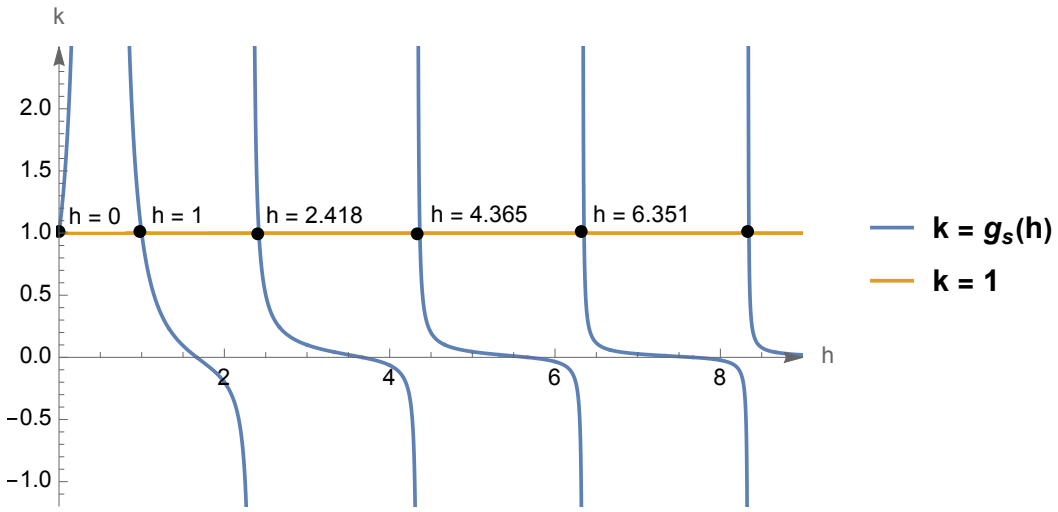

Figure 3.7: The dimensions of $U(1)$ neutral bilinear operators in the symmetric sector of the prismatic tensor model. We note that $h = 0$ and $h = 1$ are both solutions.

3.4.1.2 $U(1)$ charged sector

Now we consider the charged bilinear operator $\mathcal{O}^n_{\psi\chi}$ since, unlike the other charged operator $\mathcal{O}^n_{\bar{\psi}\chi}$, it has melonic contributions at large N. The kernel element for the channel $\psi\chi \to \psi\chi$ takes the form,

$$K = 3\lambda^2 G_\psi(t_{14}) G_\chi(t_{23}) G_\psi(t_{34})^2. \tag{3.4.39}$$

The conformal vectors for the symmetric and antisymmetric sectors are as follows,

$$\begin{aligned} v^a_{\psi\chi}(t_0, t_1, t_2) &= \frac{\text{sign}(t_{12})}{|t_{12}|^{1-2\Delta-h}}, \\ v^s_{\psi\chi}(t_0, t_1, t_2) &= \frac{1}{|t_{12}|^{1-2\Delta-h}}. \end{aligned} \tag{3.4.40}$$

Let us now calculate the contribution from this $\psi\chi \to \psi\chi$ diagram in the antisymmetric sector. We must integrate,

$$\begin{aligned}
&3\lambda^2 \int dt_3 dt_4 G_\psi(t_{14}) G_\chi(t_{23}) G_\psi(t_{34})^2 v^a_{\psi\chi}(t_0, t_3, t_4) \\
&\quad = 3\lambda^2 \int dt_3 dt_4 \left(a\delta(t_{23}) + \frac{b_\chi \text{sign}(t_{23})}{|t_{23}|^{2-6\Delta}} \right) \frac{b_\psi^3 \text{sign}(t_{14}) \text{sign}(t_{34})}{|t_{14}|^{2\Delta} |t_{34}|^{1+2\Delta-h}} \\
&\quad = 3\lambda^2 b_\psi^3 \left(a\, l^+_{2\Delta,1+2\Delta-h} \frac{1}{|t_{12}|^{4\Delta-h}} - b_\chi\, l^+_{2\Delta,1+2\Delta-h} l^-_{4\Delta-h,2-6\Delta} \frac{\text{sign}(t_{12})}{|t_{12}|^{1-2\Delta-h}} \right).
\end{aligned} \tag{3.4.41}$$

We note that in this case we have mixing between the symmetric and antisymmetric sectors. We now compute the $\psi\chi \to \psi\chi$ diagram in the symmetric sector.

$$\begin{aligned}
&3\lambda^2 \int dt_3 dt_4 G_\psi(t_{14}) G_\chi(t_{23}) G_\psi(t_{34})^2 v^s_{\psi\chi}(t_0, t_3, t_4) \\
&\quad = 3\lambda^2 \int dt_3 dt_4 \left(a\delta(t_{23}) + \frac{b_\chi \text{sign}(t_{23})}{|t_{23}|^{2-6\Delta}} \right) \frac{b_\psi^3 \text{sign}(t_{14})}{|t_{14}|^{2\Delta} |t_{34}|^{1+2\Delta-h}} \\
&\quad = 3\lambda^2 b_\psi^3 \left(a\, l^-_{1+2\Delta-h,2\Delta} \frac{\text{sign}(t_{12})}{|t_{12}|^{4\Delta-h}} + b_\chi\, l^+_{2-4\Delta-h,2\Delta} l^-_{1+2\Delta-h,2-6\Delta} \frac{1}{|t_{12}|^{1-2\Delta-h}} \right).
\end{aligned} \tag{3.4.42}$$

Let us express K in terms of the basis of conformal vectors $v^a_{\psi\chi}$ and $v^s_{\psi\chi}$,

$$K = \begin{bmatrix} -3\lambda^2 b_\psi^3 b_\chi\, l^+_{2\Delta,1+2\Delta-h} l^-_{4\Delta-h,2-6\Delta} & 3\lambda^2 b_\psi^3 a\, l^+_{2\Delta,1+2\Delta-h} \\ 3\lambda^2 b_\psi^3 a\, l^-_{1+2\Delta-h,2\Delta} & 3\lambda^2 b_\psi^3 b_\chi\, l^+_{2-4\Delta-h,2\Delta} l^-_{1+2\Delta-h,2-6\Delta} \end{bmatrix}. \tag{3.4.43}$$

We find the constraint on h by solving,

$$\det \begin{bmatrix} -3\lambda^2 b_\psi^3 b_\chi \, l^+_{2\Delta,1+2\Delta-h} l^-_{4\Delta-h,2-6\Delta} - 1 & 3\lambda^2 b_\psi^3 a \, l^+_{2\Delta,1+2\Delta-h} \\ 3\lambda^2 b_\psi^3 a \, l^-_{1+2\Delta-h,2\Delta} & 3\lambda^2 b_\psi^3 b_\chi \, l^+_{2-4\Delta-h,2\Delta} l^-_{1+2\Delta-h,2-6\Delta} - 1 \end{bmatrix} = 0. \tag{3.4.44}$$

We plot equation (3.4.44) as a function of the imaginary part of $h = \frac{1}{2} + is$ in figure 3.8, and we find a unique complex mode at $h \approx \frac{1}{2} + 1.074i$. This complex mode implies that the nearly conformal fixed point is unstable. Furthermore, from the dual AdS_2 perspective, this mode corresponds to a scalar with mass below the Breitenlohner-Freedman stability bound, since the m^2 of the scalar field dual to the operator of dimension h is equal to [15, 80, 81],

$$\begin{aligned} m^2 &= h(h-1) \\ &= -\frac{1}{4} - s^2 \\ &= m^2_{BF} - s^2. \end{aligned} \tag{3.4.45}$$

where in the second line we have used that h is in the form of $h = \frac{1}{2} + is$.

Since the conformal solutions have a complex mode, we can conclude that the full solutions require relaxing the constraints on the allowed correlators. We do not expect to find a continuum of states in our spectrum, and indeed find an $\mathcal{O}(1)$ gap between the ground state and first excited state in our exact diagonalization computations.

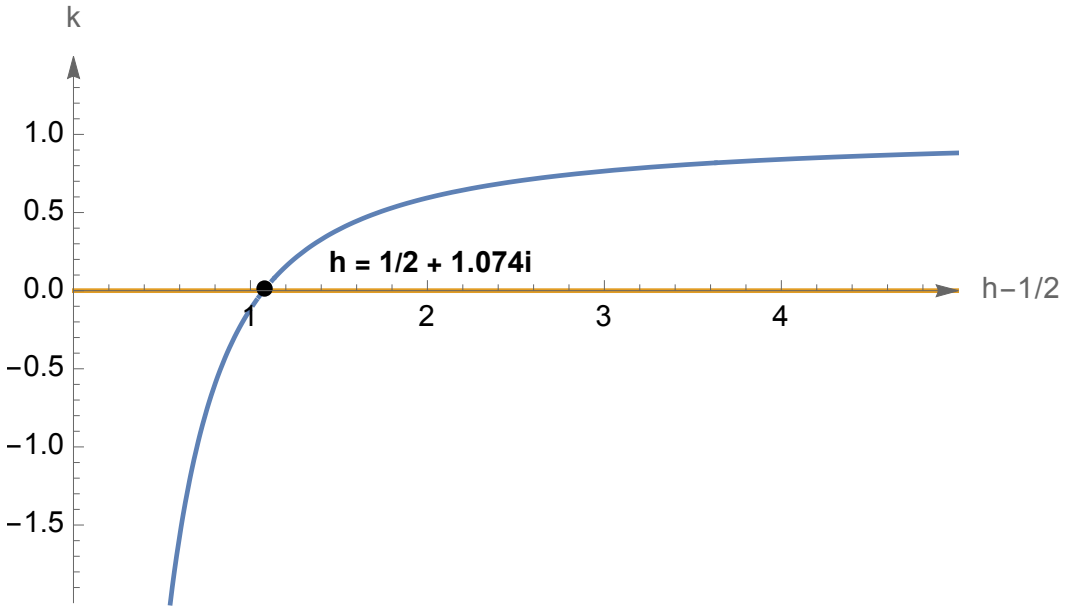

Figure 3.8: We find a unique complex mode in the $U(1)$ charged sector at $h \approx \frac{1}{2} + 1.074i$.

3.4.2 Finite temperature solutions

Let us now consider the solutions to the Schwinger-Dyson equation at finite temperature $1/\beta$,

$$\Sigma_\psi(t)/J^2 = 3G_\psi^2(t)G_\chi(\beta - t), \quad \Sigma_\chi(t)/J^2 = G_\psi^3(\beta - t), \tag{3.4.46}$$

$$\frac{1}{-iw - \Sigma_\psi(w)} = -G_\psi(-w), \quad \frac{1}{-1 - \Sigma_\chi(w)} = -G_\chi(-w). \tag{3.4.47}$$

For a given solution, the boundary condition requires:

$$G_\psi(0^+) - G_\psi(0^-) = \frac{1}{N}\{\bar{\psi}^i, \psi^i\} = 1, \quad G_\psi(0^+) + G_\psi(0^-) = \frac{1}{N}[\bar{\psi}^i, \psi^i] = 2Q/N, \tag{3.4.48}$$

where Q is the $U(1)$ charge. Therefore, at finite temperature, we expect

$$G_\psi(0) + G_\psi(\beta) = 1, \quad G_\psi(0) - G_\psi(\beta) = 2Q/N. \tag{3.4.49}$$

The low temperature numerical solution to the Schwinger-Dyson equation, which is not conformal (see figure 3.5), suggests that

$$G_\psi(0) = 0, \quad G_\psi(\beta) = 1. \tag{3.4.50}$$

That in turn suggests that the ground state has charge $-\frac{N}{2}$, which is exactly the oscillator vacuum. That is consistent with the exact diagonalization analysis. In fact, we may add a chemical potential term to our model to shift the ground state away from the $Q = -\frac{N}{2}$ sector.

3.5 Exact diagonalization results

We construct the Hamiltonian

$$\begin{aligned} H &= 36 \sum_{i,j<k<l,j'<k'<l'} J_{ijkl} J_{ij'k'l'} [\bar{\psi}^j \bar{\psi}^k \bar{\psi}^l, \psi^{l'} \psi^{k'} \psi^{j'}] \\ &= \sum_{i,j,k,l,j',k',l'} J_{ijkl} J_{ij'k'l'} [\bar{\psi}^j \bar{\psi}^k \bar{\psi}^l, \psi^{l'} \psi^{k'} \psi^{j'}], \end{aligned} \tag{3.5.1}$$

where the real random coefficients J_{ijkl} are constructed through

$$J_{ijkl} = \frac{1}{24} \sum_{\sigma \in \mathrm{S}_4} T_{\sigma(ijkl)}, \tag{3.5.2}$$

where T_{ijkl} is only non zero when $i < j < k < l$, and for a given such set of $\{i, j, k, l\}$, they are drawn from the distribution

$$\langle T_{ijkl} T_{i'j'k'l'} \rangle = \frac{6J^2}{N^3}, \tag{3.5.3}$$

for some coupling J. Such a Hamiltonian corresponds to the Lagrangian

$$\mathcal{L} = -\bar{\psi}^i \partial_t \psi^i + J_{ijkl} \left(\psi^i \psi^j \psi^k \bar{\chi}^l + \bar{\psi}^i \bar{\psi}^j \bar{\psi}^k \chi^l \right) + \bar{\chi}^i \chi^i. \tag{3.5.4}$$

since we can integrate out χ^i to obtain

$$\chi^i = J_{jkli} \psi^j \psi^k \psi^l, \tag{3.5.5}$$

and rewrite the Lagrangian to be

$$-\bar{\psi}^i \partial_t \psi^i + J_{ijkl} J_{ij'k'l'} \psi^j \psi^k \psi^l \bar{\psi}^{l'} \bar{\psi}^{j'} \bar{\psi}^{k'}, \tag{3.5.6}$$

whose Hamiltonian is given by

$$H = J_{ij'k'l'} J_{ijkl} [\bar{\psi}^{l'} \bar{\psi}^{j'} \bar{\psi}^{k'}, \psi^j \psi^k \psi^l], \tag{3.5.7}$$

where we take the normal ordering of the operators. The Lagrangian can be re-written in terms of T_{ijkl}, and we obtain,

$$\begin{aligned}\mathcal{L} = &- \bar{\psi}^i \partial_t \psi^i + \bar{\chi}^i \chi^i + \\ &+ \frac{1}{4} \sum_{i<j<k<l} T_{ijkl} \left(\psi^i \psi^j \psi^k \bar{\chi}^l - \psi^i \psi^j \psi^l \bar{\chi}^k - \psi^i \psi^l \psi^k \bar{\chi}^j - \psi^l \psi^j \psi^k \bar{\chi}^i + h.c. \right).\end{aligned} \tag{3.5.8}$$

Now we integrate out T_{ijkl}, which gives an action

$$S = \int dt \left(-\bar{\psi}^i \partial_t \psi^i + \bar{\chi}^i \chi^i \right) + \int dt dt' \frac{1}{32} \times \frac{6J^2}{N^3} \sum_{i<j<k<l} I^{ijkl}(t) \bar{I}^{ijkl}(t'), \tag{3.5.9}$$

where

$$I^{ijkl}(t) = \left(\psi^i \psi^j \psi^k \bar{\chi}^l - \psi^i \psi^j \psi^l \bar{\chi}^k - \psi^i \psi^l \psi^k \bar{\chi}^j - \psi^l \psi^j \psi^k \bar{\chi}^i + h.c. \right). \tag{3.5.10}$$

Note since J_{ijkl} is real, we need to consider also correlators between $\psi^i \psi^i$ and $\psi^i \bar{\chi}^i$, etc. For a solution with no mixed correlator, the action takes a simple form

$$S = \int dt \left(-\bar{\psi}^i \partial_t \psi^i + \bar{\chi}^i \chi^i \right) + \frac{J^2}{16N^3} \int dt dt' \bar{\psi}^i(t) \psi^i(t') \bar{\psi}^j(t) \psi^j(t') \bar{\psi}^k(t) \psi^k(t') \chi^l(t) \bar{\chi}^l(t') \tag{3.5.11}$$

Introducing the Lagrange multipliers, we obtain the large N action similar to what we had before. Note for the Hamiltonian, the ground state energy is given by

$$\langle 0|H|0\rangle = -6 \sum_{i,j,k,l} J_{ijkl}^2. \tag{3.5.12}$$

We substitute the definition of J to obtain,

$$\begin{aligned} E_0 &\sim -\frac{3J^2}{2N^3}\binom{N}{4} \\ &\sim -\frac{NJ^2}{16} + \frac{3J^2}{8} - \frac{11J^2}{16N} + \frac{3J^2}{8N^2}. \end{aligned} \tag{3.5.13}$$

We find very good agreement ($< 0.5\%$ discrepancy) between the ground state energy for small N, displayed in figure 3.9, and the predicted energy from equation (3.5.13). At large N, this is close to the numerical ED result, which is $E_0/N \sim -0.057J^2$, see figure 3.9. We can also look at one fermion states $\bar{\psi}^i|0\rangle$. It's helpful to note that

$$\{\bar{\chi}^i, \chi^i\} = 3J_{ijkl}J_{ijk'l'}\{\bar{\psi}^l\bar{\psi}^k, \psi^{k'}\psi^{l'}\} + 3J_{ijkl}J_{ij'k'l'}\bar{\psi}^l\psi^{j'}\psi^{l'}\bar{\psi}^j. \tag{3.5.14}$$

Also note that

$$H\bar{\psi}^I|0\rangle = 6J_{ijkl}J_{ijkI}\bar{\psi}^l|0\rangle + E_0\bar{\psi}^I|0\rangle. \tag{3.5.15}$$

The expectation value of the first excited state energy is given by

$$E_1 \sim E_0 + \frac{J^2}{16} + \ldots \tag{3.5.16}$$

Thus, we expect the energy gap in our spectrum should be close to $J^2/16$. We find a large discrepancy between the energy gap prediction and the exact diagonalization results for $N = 12$, 13, and 14. Perhaps a larger sample size is needed here.

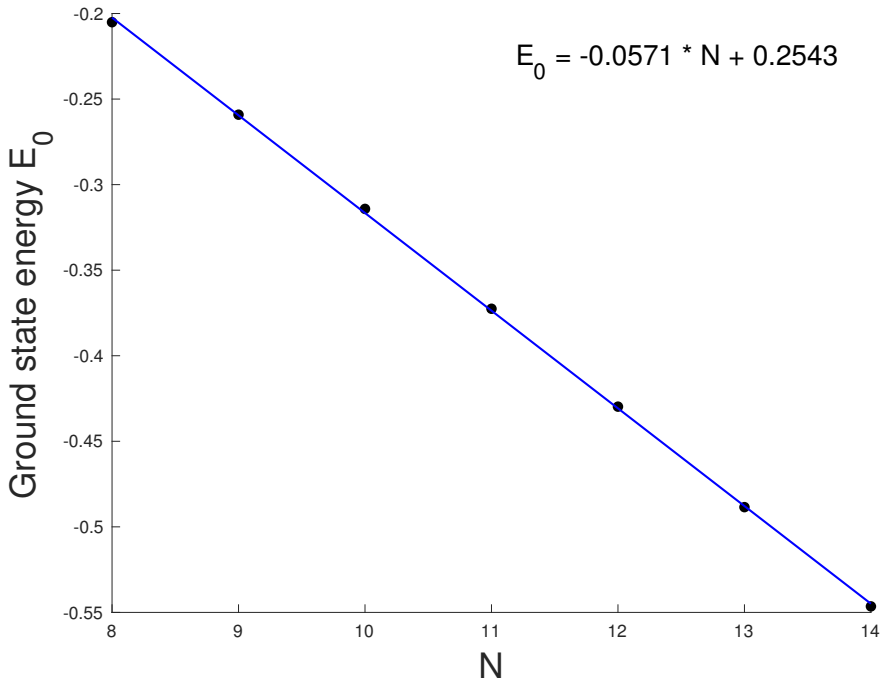

Figure 3.9: Plot of the ground state energy, E_0, versus N.

3.5.1 Entropy

We can compute the entropy of our model via exact diagonalization results. From the full spectrum, we can compute the partition function Z, the free energy F, and the average energy $\langle E \rangle$ as follows,

$$Z = \sum_n e^{-\beta E_n}, \quad F = -\beta \log Z, \quad \text{and} \quad \langle E \rangle = \frac{\sum_n E_n \, e^{-\beta E_n}}{Z}, \tag{3.5.17}$$

where E_n are the eigenvalues of our model (3.5.7).

Using the above equations (3.5.17), the entropy density is found via,

$$\frac{S}{N} = \frac{\beta\langle E\rangle}{N} - \frac{\beta F}{N}. \tag{3.5.18}$$

The entropy density is shown in figure 3.10. We can see that in the high temperature regime, the entropy density tends towards a $\log 2$ limit.

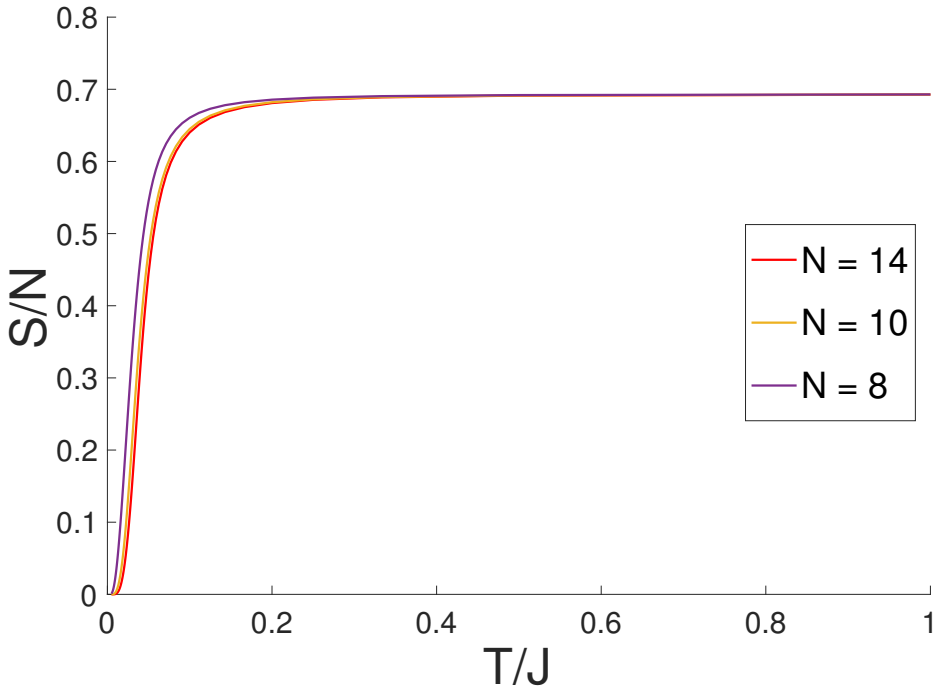

Figure 3.10: Plot of the entropy density derived from the exact diagonalization results with $N = 8$, 10, and 14.

3.5.2 Charge compressibility

The global $U(1)$ charge Q is defined as follows,

$$Q = \sum_i \frac{1}{2}\left[\psi_i^\dagger, \psi_i\right] = \sum_i \psi_i^\dagger \psi_i - \frac{N}{2}. \tag{3.5.19}$$

We numerically compute the charge compressibility by quadratically fitting the plot of the ground state energy within each charge sector versus the charge sector according to the equation,

$$E_0(Q) = E_0 + Q^2(2NK)^{-1}. \tag{3.5.20}$$

Here, $E_0(Q)$ is the ground state within a specific charge sector, and E_0 is the ground state energy. The fits are displayed in figure 3.11, and the average value of K from the best fit parameters is ≈ -12.6755.

In our model, the ground state is in the $-\frac{N}{2}$ charge sector. We find that by adding a chemical potential term, μ, to our Hamiltonian,

$$H = H_0 + \mu Q, \tag{3.5.21}$$

we are able to shift the ground state energy from the $Q = -\frac{N}{2}$ sector to the $Q = 0$ sector. Here, μ is chosen such that the oscillator vacuum is annihilated by the Hamiltonian. Further, we add a term quadratic in Q, which keeps the ground state in the $Q = 0$ sector, and also gives a positive charge compressibility.

$$H = H_0 + \mu Q + \gamma Q^2. \tag{3.5.22}$$

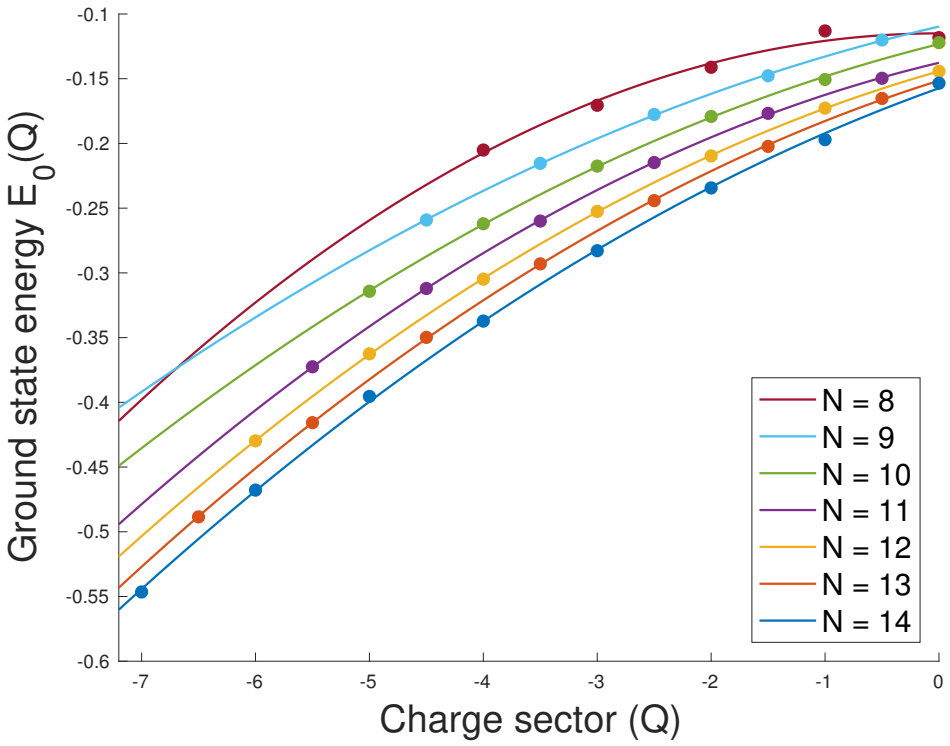

Figure 3.11: Plot of the ground state energy, E_0, versus Q for several values of N with no chemical potential term added to the Hamiltonian. We can find the approximate charge compressibility K of our system by fitting the data to a quadratic form. We find that $\langle K \rangle \approx -12.6$.

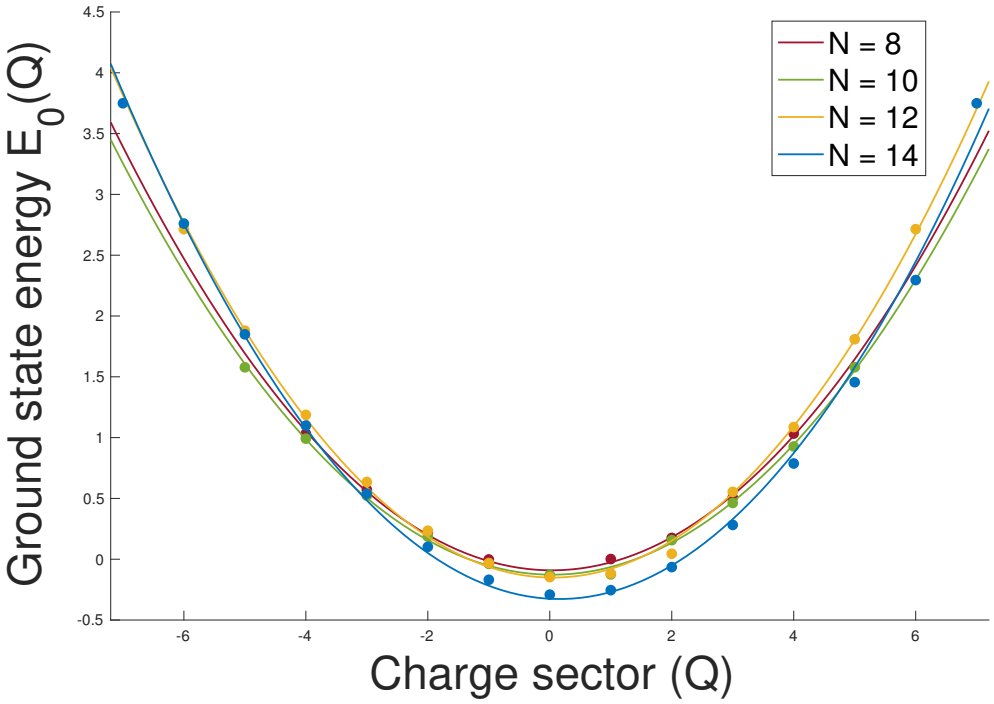

Figure 3.12: Plot of the ground state energy, E_0, versus Q for several values of N with Hamiltonian (3.5.22). We can find the approximate charge compressibility K of our system by fitting the data to a quadratic form. We find that $\langle K \rangle \approx 0.769$.

We find that the charge compressibility is $K \approx 0.769$ as shown in figure 3.12, using the model (3.5.22) with $\mu = \gamma$.

3.6 Appendix: The dynamical χ model

Here, we study the model from equation (3.2.5) where the auxiliary field χ is promoted to a dynamic field. The scaling dimension is again determined by,

$$1 = \frac{(1 - 2\Delta_\psi)\tan(\Delta_\psi \pi)}{3\,(6\Delta_\psi - 1)\tan(\pi(1 - 3\Delta_\psi))} \tag{3.6.1}$$

as solved in equation (3.4.9) in section 3.4.

The first solution is at $\Delta_\psi \approx 0.311$ and $\Delta_\chi \approx 0.068$, see figure 3.4. Similarly, the constants b_ψ and b_χ satisfy the same condition provided in equation (3.4.7),

$$\lambda^2 b_\psi^3 b_\chi = \frac{(1-2\Delta_\psi)\tan(\Delta_\psi \pi)}{6\pi} \tag{3.6.2}$$

Using the conformal ansatz that,

$$G_\psi(t) = \frac{b_\psi \text{sign}(t)}{|t|^{2\Delta_\chi}}, \quad G_\chi(t) = \frac{b_\chi \text{sign}(t)}{|t|^{2\Delta_\psi}}, \tag{3.6.3}$$

where $\Delta_\chi = 1-3\Delta_\psi$. We evaluate the $U(1)$ neutral sector bilinear spectrum following the same procedure as section 3.4 to find the following constraint equations,

$$1 = -6\lambda^2 b_\psi^3 b_\chi l^+_{2\Delta,2-2\Delta-h} l^-_{1-h,2\Delta} - 9\lambda^4 b_\psi^6 b_\chi^2 l^+_{2\Delta,2-2\Delta-h} l^-_{1-h,2\Delta} l^+_{2-6\Delta,6\Delta-h} l^-_{1-h,2-6\Delta}, \tag{3.6.4}$$

$$1 = 6\lambda^2 b_\psi^3 b_\chi l^+_{2\Delta,1-h} l^-_{2-2\Delta-h,2\Delta} - 9\lambda^4 b_\psi^6 b_\chi^2 l^+_{2\Delta,1-h} l^-_{2-2\Delta-h,2\Delta} l^+_{2-6\Delta,1-h} l^-_{6\Delta-h,2-6\Delta}. \tag{3.6.5}$$

Here, equation (3.6.4) comes from the antisymmetric sector and equation (3.6.5) comes from the symmetric sector. The plots of equations (3.6.4) and (3.6.5) are displayed in figures 3.13, 3.14, and 3.15. The antisymmetric sector contains the $h = 2$ mode and has no complex modes. Curiously, we see a solution before $h = 2$, see figure 3.13.

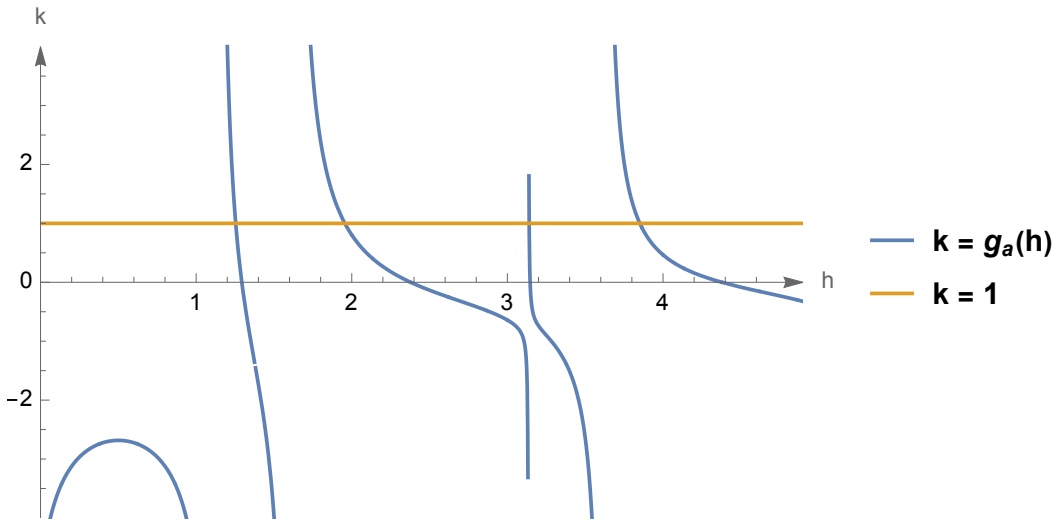

Figure 3.13: The scaling dimension Δ_ψ in the antisymmetric sector of the dynamic χ model. We a solution before the $h = 2$ mode at $h \approx 1.2$. The next few solutions are at $h \approx 3.14, 3.85, 5.80, 7.76, \ldots$

3.7 Appendix: Chaos properties of the $q = 6$ WL-SYK model

We briefly consider the chaotic properties of our $q = 6$ WL-SYK model. We compute the spectral form factor (SFF), the level spacings ratio $\langle r \rangle$, and plot the level spacings distribution for the $N = 14$, $q = 6$ WL-SYK model. Below, we briefly review the definition of these quantities. The spectral form factor $g(t, \beta)$ is defined as,

$$g(t, \beta) = |Tr(e^{-\beta H - iHt})|^2 / Tr(e^{-\beta H})^2, \tag{3.7.1}$$

and a dip ramp plateau structure in the SFF plot is characteristic of a chaotic system. The level spacings distribution is the probability density function (pdf) of the spacing

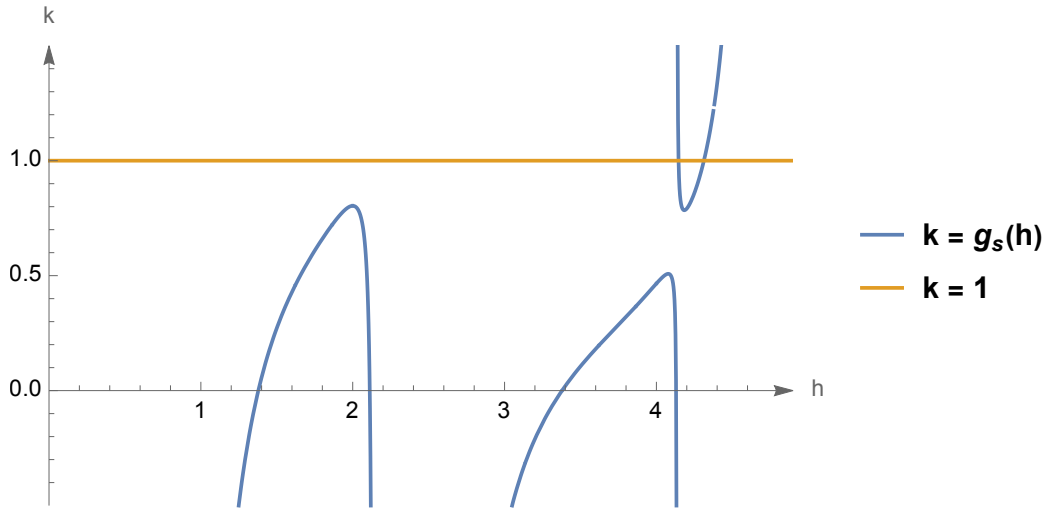

Figure 3.14: The scaling dimension Δ_ψ in the symmetric sector of the dynamic χ model. We are missing the solutions at $h = 0$ and $h = 1$. The first few solutions are at $h \approx 4.11, 4.31, 6.41, 8.46, 10.48, \ldots$

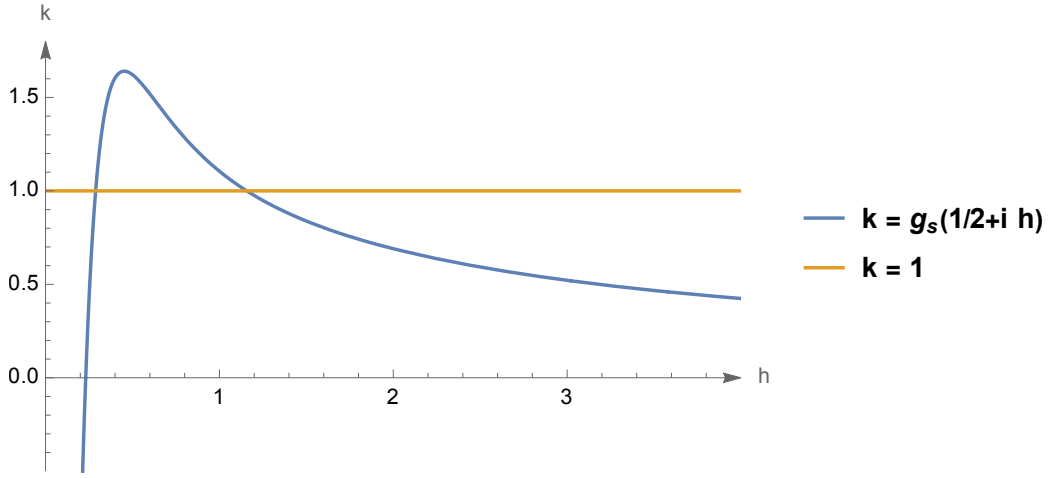

Figure 3.15: Plot of (3.6.5) as a function of the imaginary part of $h = \frac{1}{2} + is$. There are two solutions at $h = \frac{1}{2} + 0.285i$ and $h = \frac{1}{2} + 1.157i$. These correspond to the two missing $h = 0$ and $h = 1$ modes from the symmetric sector.

between the eigenvalues, and the level spacings ratio, r, is equal to,

$$r = \frac{s_i}{s_i - 1}, \text{ where } s_i = \lambda_{i+1} - \lambda_i. \tag{3.7.2}$$

The mean spacings ratio is equal to $\langle r \rangle \approx 0.386$ for the Poisson ensemble, and $\langle r \rangle \approx 0.536$, $\langle r \rangle \approx 0.603$, and $\langle r \rangle \approx 0.676$ for the Gaussian orthogonal ensemble (GOE), the Gaussian unitary ensemble (GUE), and the Gaussian symplectic ensemble (GSE) respectively [40].

We find that our model has the dip ramp plateau structure characteristic of a chaotic system for small inverse temperature β, see figure 3.16. However, our model has $\langle r \rangle \approx 0.453$, which is between that of the Poisson distribution and the Wigner-Dyson ensembles. We can see this intermediate behavior in the level spacings distribution, see figure 3.16. Presumably, with larger N we will see the $\langle r \rangle$ value and the level spacings plot approach those of a Wigner-Dyson ensemble.

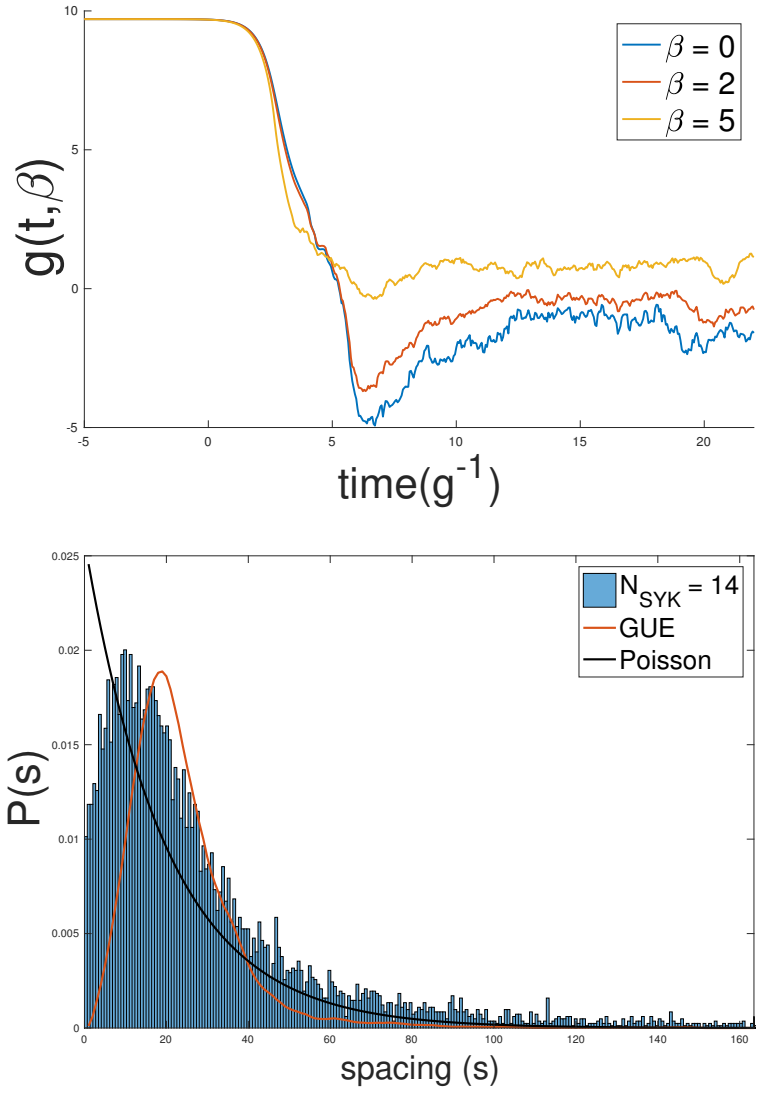

Figure 3.16: Top: The SFF for the $N = 14$, $q = 6$ WL-SYK model at three different values of inverse temperature β. We see the dip ramp plateau structure characteristic of a chaotic system. Bottom: Plot of the level spacings distribution for the $N = 14$, $q = 6$ WL-SYK model. We can see that the distribution lies between that of the Poisson ensemble and the GUE.

Chapter 4

Many Body Scars as a Group Invariant Sector of Hilbert Space

4.1 Introduction

This chapter is based on [47] and [48]. The concept of many-body scar states has recently emerged as a novel type of weak ergodicity breaking [82–101]. These states are typically found in the bulk of the spectrum and thus play a role at high temperatures. The scars are special because they have low (area-law) entanglement entropy, do not thermalize, and lead to the exact 'revivals' of the initial state of the system initialized with scars. Therefore, the information stored in the system does not dissipate at finite temperature, holding promise for potential applications of such states in quantum information processing.

The current knowledge of the nature of this phenomenon is based on the identification of scars in a variety of systems, such as the AKLT spin chain [82], interacting fermionic models [83,88,90,91], the spin-1 XY model [89], frustrated spin systems [97], and a spin-$\frac{1}{2}$ domain-wall conserving model [98, 99]. In some cases [90, 94, 100], the scar states are related to the well-known η-pairing states of the Hubbard model, which form a family under the $SU(2)$ symmetry called pseudospin [102–104]. There has been experimental observation of the approximate revivals [105], yet a general understanding of the underlying structures leading to the existence of scars is not yet available.

The Hamiltonians exhibiting scars can be often brought to the form $H = H_0 + H_1$, such that H_1 breaks some of the symmetries of H_0 and has a special property that it annihilates a subsector of the Hilbert space $\mathbb{S}$ consisting of eigenstates of H_0. In this chapter, we discuss how the symmetry properties of the Hilbert space can be used to construct scars systematically. We analyze a rich class of models where the scar subsector $\mathbb{S}$ is invariant under the action of a continuous group G, which is bigger than the symmetry of the full Hamiltonian. The requisite Hermitian operator H_1 must have the form $H_1 = \sum_j O_j T_j$, where T_j are generators of the symmetry group G and O_j is any operator s.t. the product $O_j T_j$ is Hermitian. For H_0, the simplest option is that it has symmetry G, i.e. $[H_0, T_j] = 0$, but the most general condition is that,

$$[H_0, C_G^2] = W \cdot C_G^2, \tag{4.1.1}$$

where W is some operator and C_G^2 is the quadratic Casimir of the group G. Then the states invariant under G are eigenstates of H_0.

We find that, for any Hamiltonian of the form

$$H = H_0 + \sum_a O_a T_a, \tag{4.1.2}$$

the dynamics of the scar subsector $\mathbb{S}$ is governed by H_0 and is decoupled from the rest of the spectrum controlled by H. If the ergodic properties of H_0 and H are sufficiently different every state in the decoupled sector $\mathbb{S}$ will not thermalize with the rest of the system and will thus violate the eigenstate thermalization hypothesis (ETH) [106–108]. Because of the decoupling, the unitary time evolution starting from a state in the invariant sector cannot mix it with the rest of the system. In addition, if the energy gaps between the states from the invariant subsector have a common divisor [a], then the unitary time evolution of a state from the invariant sector will exhibit revivals: the initial state will return to itself after equal time intervals (this is similar to the recurrence time introduced in section 2.3 of chapter 2). Therefore the states in $\mathbb{S}$ possess all of the defining properties of the many-body scar states. To our knowledge, such general constructions have not been discussed previously, and we present their concrete examples.

The general class of models we study includes the famous Fermi-Hubbard model and its deformations. In this context we show that, in addition to the family of states which transform as spin-$N/2$ under the pseudospin symmetry (the η-pairing states), which were recently shown to be scar states in [90, 94, 100], there is another family of scar states. This second family, whose states may be explicitly written down as (4.2.6) or (4.3.6), is invariant under the $U(N)$ symmetry which acts on the degrees

[a] This happens, for example, when the energies of all states in $\mathbb{S}$ are integers in some units.

of freedom on all N lattice sites; it forms a multiplet of spin-$N/2$ under the $SU(2)$ which is the physical rotational symmetry in the Fermi-Hubbard and related models.

4.2 Specific constructions

The structure of the Hilbert space determines the existence and properties of the invariant subspace $\mathbb{S}$. We will focus on the Hilbert space of M fermionic oscillators

$$\{c_I, c_{I'}^\dagger\} = \delta_{II'}, \quad I, I' = 1, \ldots, M \ , \tag{4.2.1}$$

which has dimension 2^M and is acted on by $U(M)$. The Hilbert space forms a spinor representation of $O(2M)$, which acts on the $2M$ Majorana fermions, and we can choose G to be any of its subgroups. The choice of G provides an important handle on the dimension of the scar subspace: the smaller the group G, the bigger the invariant scar sector $\mathbb{S}$.

For $M = 2N$ one may interpret [109] this Hilbert space as that of a lattice model with N sites and two fermionic degrees of freedom per site (they may correspond to the two states of a spin-1/2 fermion). The Hilbert space and the structure of the invariant subspace $\mathbb{S}$ we consider are thus identical to that in a number of spin-1/2 models, such as Hubbard, Hirsch and their deformations. There are two useful ways this Hilbert space can be factorized [18, 110]: according to the representations of $U(N) \times SU(2)$ or according to the representations of $O(N) \times SO(4) = O(N) \times SU(2) \times SU(2)$ (the relevance of group $SO(4)$ was noted long ago in the context of Hubbard model [103, 104]). Choosing a singlet representation of $U(N)$ fixes the $(N+1)$-dimensional

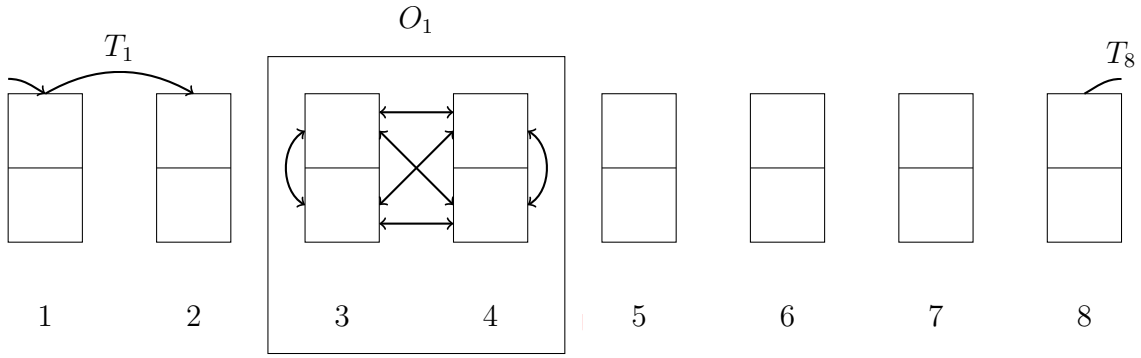

Figure 4.1: Schematic representation of the Hilbert space and model (4.2.4). Each line corresponds to a hopping T_i or some bilinear operator in terms of fermion operators. Figure is adapted from reference [47].

spin-$N/2$ representation of $SU(2)$ - the maximal representation of $SU(2)$ in the given Hilbert space. An analogous relation for orthogonal groups indicates that the $O(N)$ singlets transform in the $(N/2, 0)+(0, N/2)$ representation of $SO(4) \sim SU(2)\times SU(2)$, where we labeled the $SU(2)$ representations by their spin J. Thus, there are two sets of $(N+1)$ invariant $O(N)$ states; each one is invariant under one of the $SU(2)$ groups and transforms as spin-$N/2$ under the other.

We see that there are two natural choices for the subgroup of $U(2N)$: $G = U(N)$ or $G = O(N)$, both acting on the degrees of freedom on all N lattice sites. The lattice may be thought of as one-dimensional, as in figure 4.1, but the specific way the $U(N)$ or $O(N)$ indices are mapped to spatial lattice indices is not important for the purposes of finding scars. In particular, the lattice can be of arbitrary dimension, frustrated, and can have any boundary conditions.

The hopping term on this lattice is $T = \sum_{aa',\sigma} t_{aa'}\, c^\dagger_{a\sigma} c_{a'\sigma}$, where the first index of $c_{a\sigma}$ labels the sites, the second index the 'spin,' and $t_{aa'}$ is the hopping strength

Hermitian matrix. One can see that, for a general complex $t_{aa'}$, the hopping T is a generator of $SU(N)$ that acts on the indices a (see [18]). Adding the charge Q to the set of generators we would obtain generators of $U(N)$. For purely imaginary $t_{aa'}$ the hopping T is a generator of $SO(N)$, and for real $t_{aa'}$ the situation depends on the parity of N.

4.2.1 Vector Example

Following the prescription (4.1.2) we first have to choose H_0 that will control the scar subsector; it must satisfy (4.1.1). We will use the following integrable fermionic Hamiltonian [18],

$$\begin{aligned} H_0 &= 2\left(c^\dagger_{a\sigma}c^\dagger_{a\sigma'}c_{a'\sigma}c_{a'\sigma'} - c^\dagger_{a\sigma}c^\dagger_{a'\sigma}c_{a\sigma'}c_{a'\sigma'}\right) \\ &\quad +2(2-N)Q + N(2-N)\ , \\ \{c_{a\sigma}, c^\dagger_{a'\sigma'}\} &= \delta_{aa'}\delta_{\sigma\sigma'}, \quad a = 1,\dots,N\ ,\ \sigma = 1,\dots,2\ , \end{aligned} \tag{4.2.2}$$

where summation over repeated indices is implied. It may be viewed as a generalized Hubbard interaction term which has a continuous symmetry $O(N)\times O(2)$, in addition to the usual $U(1)$ symmetry with conserved charge $Q = \frac{1}{2}[c^\dagger_{a\sigma}, c_{a\sigma}]$. It is a special case, $N_2 = N_3 = 2$, of the $O(N_1)\times O(N_2)\times O(N_3)$ fermionic tensor model [3, 18]. While in general the tensor model is not integrable [21], for $N_3 = 2$ it is [18, 110], and all of the energies are integer. Because of the $O(N)\times O(2)$ symmetry we have $[H_0, C^2_{U(N)}] = W\cdot C^2_{U(N)} \neq 0$ and $[H_0, C^2_{O(N)}] = 0$ in agreement with (4.1.1) which ensures the group-invariant states from $\mathbb{S}$ are eigenstates of this H_0.

The singlets in $\mathbb{S}$ have several quantum numbers [110], which can be used to distinguish them (none of them are conserved by the full Hamiltonian (4.2.4)). This includes particle number Q and one of the $SU(2)$ charges,

$$Q_2 = -i\left(c^\dagger_{a1}c_{a2} - c^\dagger_{a2}c_{a1}\right) = c^\dagger_{a\sigma}\sigma^2_{\sigma\sigma'}c_{a\sigma'} \ . \tag{4.2.3}$$

To control the energies of the singlets and the period of revivals, we can add $\alpha Q + \beta Q_2$ to H_0. Adding also the hopping terms results in the Hamiltonian $H_T = T + H_0 + \alpha Q + \beta Q_2$ which remains integrable. If T is a generator of $SO(N)$ (imaginary amplitude) the problem can be solved analytically and T simply splits each of the $O(N)$ representations analogously to Zeeman splitting.

The full example Hamiltonian we will study numerically ($N = 8$, $\alpha = \beta = 1$, periodic boundary conditions) reads[b]

$$H = H_T + 4\sum_{a=1}^{N} O^T_a T_a + 32\sum_{a=1}^{N} O^Q_a(Q_a - 1), \text{ where} \tag{4.2.4}$$

$$O^T_a = \sum_{a_{1,2}=(a+2),\sigma,\sigma'}^{(a+3)} \left[q^1_{a_{1,2},\sigma,\sigma'}c^\dagger_{a_1\sigma}c^\dagger_{a_2\sigma'} + q^2_{a_{1,2},\sigma,\sigma'}c^\dagger_{a_1\sigma}c_{a_2\sigma'} + \text{h.c.}\right],$$

$$O^Q_a = \sum_{\sigma=1}^{2}\left[c^\dagger_{a+1\sigma}c^\dagger_{a-1\sigma} + \text{h.c.}\right] \ , \quad Q_a = \sum_{\sigma=1}^{2} c^\dagger_{a\sigma}c_{a\sigma} \ .$$

$T_a = 8e^{i\sqrt{2}\pi}\sum_\sigma c^\dagger_{a\sigma}c_{a+1\sigma}$ is a translation-invariant nearest-neighbor hopping and a generator of $SU(N)$. The operator O^T_a acts on sites $a+2$ and $a+3$ which ensures that $O^T_a T_a$ is Hermitian and local. The coefficients $q^{1,2}_{a_{1,2},\sigma,\sigma'}$ are random complex numbers

[b]The Hamiltonian $H = H_0 + OT$ has the same properties with respect to the presence of the many-body scar states.

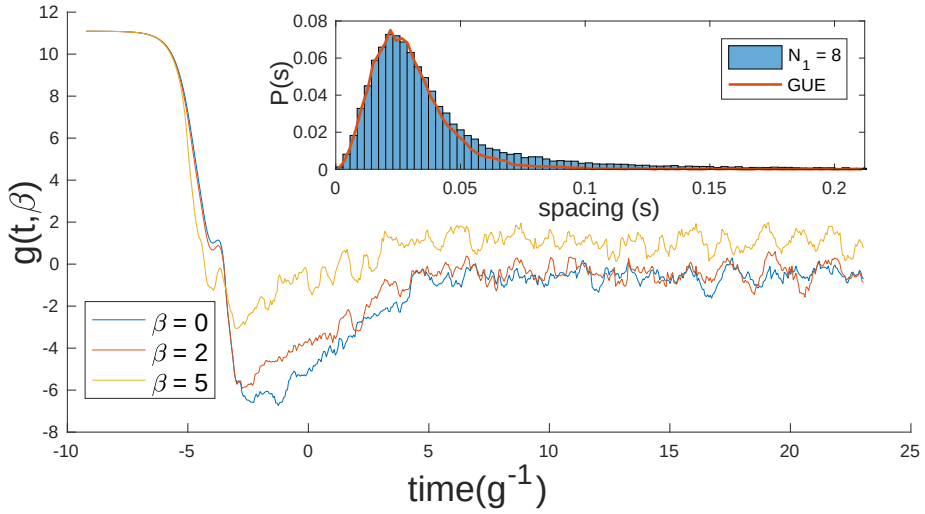

Figure 4.2: Histogram of the nearest neighbor eigenvalue spacings (inset, shown for the even Q sector) and the spectral form factor (shown for the full spectrum) for the model in (4.2.4).

and this choice of the (arbitrary according to (4.1.2)) operator O is intended to break the symmetries of H_0 and to make the bulk of the spectrum ergodic. Operators $(Q_a - 1)$ complement T_a to form the set of $U(N)$ generators and the full Hamiltonian is of the form (4.1.2) for $G = U(N)$.

Most states in the Hilbert space will be mixed by the randomness built into O while the effective Hamiltonian for the $U(N)$-invariant states in $\mathbb{S}$ remains $H_{\mathbb{S}} = H_0$. The only remaining symmetry of H relates the sectors with odd and even Q, both described by the gaussian unitary ensemble (GUE) (see figure 4.2 for the exact numerical results). The time-reversal symmetry is broken by the operator $c^\dagger_{a\sigma} c_{a\sigma}$ in O_a.

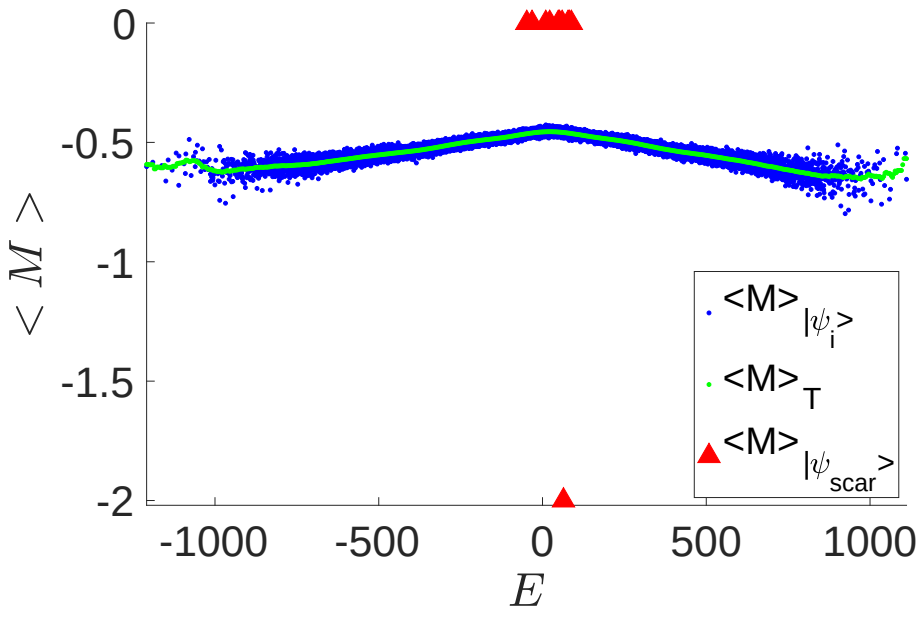

Figure 4.3: Eigenstate (blue dots) and window-averaged (green line) expectation values for $\mathcal{M} = -2c_{11}^{\dagger}c_{11}c_{12}^{\dagger}c_{12}$. $SU(8)$-singlet states are shown in red triangles.

The probability distribution $P(r_k)$ of the level spacings (inset of figure 4.2) agrees well with the GUE overlay. It contains information about the correlation functions of close eigenvalues, whereas the spectral form factor, $g(t,\beta) = |\mathrm{Tr}(e^{-\beta H - iHt})|^2/\mathrm{Tr}(e^{-\beta H})^2$, also contains information about longer range correlations. The main elements of the spectral form factor (SFF) for a random matrix is a dip ramp plateau structure (for a discussion of their physics, see [22]). The presence of this structure in our system is another evidence of quantum chaos and ergodicity in its bulk spectrum.

A more detailed characterization of ergodicity is provided in figure 4.3 where we test the eigenstate thermalization hypothesis (ETH), which conjectures that for any measurable local operator $\mathcal{M}$, its expectation value in an eigenstate must be

approximately the same as the window-average over the nearby states at the same energy. We observe that the conjecture holds for most states in the spectrum while it is clearly violated for the eleven $SU(8)$ singlet states $\{|n_U\rangle\}$ that do not thermalize. The situation when the bulk of the spectrum (dimension $2^{2N} - N - 3$) is ergodic while an exponentially small subset of states is not (there are $N + 3$ $SU(N)$ singlets in our Hilbert space), corresponds by definition to the violation of the strong formulation of ETH (the weak formulation allows for a few 'outlier' states) [106–108].

The singlet states violating strong ETH also clearly stand out in the time evolution. Consider two initial states ψ_0^s, made exclusively of singlet eigenstates of H and ψ_0^g, composed of the same number of generic states. In both cases we can write $|\psi_0^{s/g}\rangle = \sum c_n |\psi_n\rangle$, where $|\psi_n\rangle$ is an eigenstate of H with energy E_n. We are interested in the squared projection of the time-evolved state on the initial wavefunction $f(\tau) = |\langle\psi_0|e^{-iHt}|\psi_0\rangle|^2 = \sum_{n,m} |c_n c_m|^2 e^{-i(E_n - E_m)\tau}$. It should relatively quickly go to zero if the states are generic without particular correlations between energies E_n. Exact numerical results confirming this are shown in the right panel of figure 4.4. A vanishing overlap with the initial state indicates that the information stored initially has fully dissipated through thermalization. This phenomenon is closely related to the dip seen in the SFF in figure 4.2.

For the singlet states, all of the energies E_n are integer, which means that there exists a (greatest) common divisor for all of the energy gaps between singlet states $E_n - E_m$: $\omega = \gcd(E_n - E_m)$. After the time $T = k\frac{2\pi}{\omega}$, $k \in \mathbb{Z}$ all of the exponents in $f(\tau)$ are equal to 1. This constructive interference results in 'revivals' of the (information stored in the) initial state with period t_r^1. In our numerical example

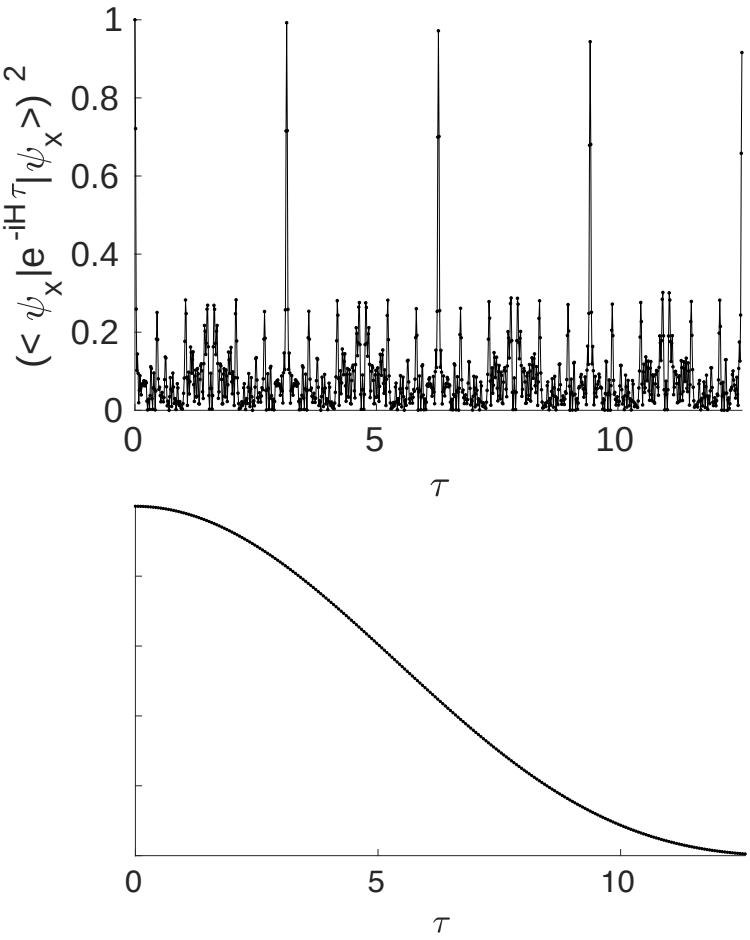

Figure 4.4: Time dependence of the fidelity $f(\tau)$ for vector model with $N = 8$. The initial state is a linear combination of 50 eigenstates of H and $\alpha = \sum_{n=1}^{11} |c_n|^2 = 0.95$. Top: the initial state is dominated by 11 singlet states. The fidelity demonstrates oscillations with the period $T \approx 3.14$ and amplitude $A \approx \alpha^2$. Bottom: the initial state is dominated by 11 generic high-energy states, the fidelity is quickly decaying.

$\omega = 2$, and thus we observe the revivals with period π, as shown in the left panel of figure 4.4. Note that, in this calculation 5 percent of generic states were admixed to the initial state, but ideal revivals to $f(\tau) = 1$ would be observed otherwise. The higher-frequency 'revivals' with smaller amplitude are due to the energy differences

that are shared only by a subset of the singlet states. The energies of singlets are controlled by $H_0 + \alpha Q + \beta Q_2$; therefore, the period of the revivals is a function of the parameters α and β. While a pure state is coherently oscillating in our case, we note that an interesting construction of environment-assisted, non-stationary dynamics for mixed states was discussed in the literature recently [111].

Two of the scar states are tensor products of Bell-like states formed on each site:

$$|S_1\rangle = \bigotimes_a \frac{|0_{a1}1_{a2}\rangle + i\,|1_{a1}0_{a2}\rangle}{\sqrt{2}} = \prod_a \frac{c^\dagger_{a1} + ic^\dagger_{a2}}{\sqrt{2}}\,|0\rangle \tag{4.2.5}$$
$$|S_2\rangle = \bigotimes_a \frac{|0_{a1}1_{a2}\rangle - i\,|1_{a1}0_{a2}\rangle}{\sqrt{2}} = \prod_a \frac{c^\dagger_{a1} - ic^\dagger_{a2}}{\sqrt{2}}\,|0\rangle \ ,$$

These states can be easily created in experiment and we provide the corresponding gate sequences in figure 4.5. The energies of these states are given by $E_{S_1} = E_0 + \alpha N + \beta N = N(\alpha + \beta + 2 - N)$ and $E_{S_2} = E_0 + \alpha N - \beta N = N(2 + \alpha - \beta - N)$. Initializing a system to an arbitrary superposition of these two states may be the most accessible experimental demonstration of revivals.

The complete set of $N + 1$ states invariant under the $U(N)$ symmetry [110] can be constructed by acting repeatedly on the state $|S_1\rangle$ with the bilinear operator $\zeta = c^\dagger_{ab}(\sigma^3 - i\sigma^1)_{bb'}c_{ab'}$ (this is a 'rotated' version of the zeta-operator in [104]):

$$|n_U\rangle = \frac{\zeta^n}{2^n\sqrt{\frac{N!n!}{(N-n)!}}}\,|S_1\rangle \ , \tag{4.2.6}$$

with $n = 0, \ldots, N$.

Another basis for this family of states is given in equation (4.3.6). One can see that these states have the maximal possible spin-$N/2$ with respect to the index σ, i.e. they transform as a $(N+1)$-dimensional representation of $SU(2)_\sigma$, which is the physical spin in the Fermi-Hubbard model. There is only one family which has the maximal spin. Consequently, it is quite robust under the action of any perturbation that preserves this spin. Namely, any spin-preserving perturbation will map this representation to itself which means these states will continue to violate strong ETH while the revivals may disappear as a result of changing their energies.

If instead of a complex hopping strength we chose a purely imaginary one (or a real hopping strength and bipartite lattice), then the hopping terms are generators of $SO(N)$. As it was explained in the introduction, the Hilbert space may be decomposed [110] according to representations of $O(N) \times SO(4)$. There are $2N+2$ singlet states that could be organized in two sets. One of these sets is $|n_U\rangle$, for which the $O(N) \times SU(2)$ symmetry is further enhanced to $U(N)$. The other set of $N+1$ states is

$$|n_O\rangle = \frac{\eta^n}{\sqrt{\frac{N!n!}{(N-n)!}}} |0\rangle \ , \qquad \eta = \sum_{a=1}^{N} c_{a1}^\dagger c_{a2}^\dagger \ , \tag{4.2.7}$$

with $n = 0, \ldots, N$. These states are invariant under $G = O(N) \times SU(2)$ and also $\widetilde{U}(N) \times SU(2)$, where the $\widetilde{SU}(N)$ subgroup of $\widetilde{U}(N)$ is generated by spin flip hopping terms along with spin-preserving hopping terms with imaginary amplitude. They transform as spin-$N/2$ under the pseudospin symmetry. They are equivalent to the exact eigenstates of the Hubbard model originally identified using the celebrated η-pairing [102] and recently demonstrated to be many-body scar states [90, 100] (to

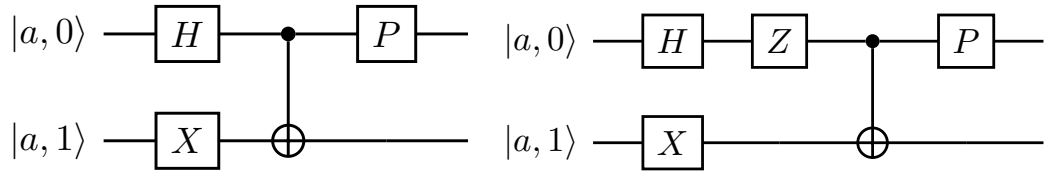

Figure 4.5: Left panel: Circuit diagram of W_a for construction of $|S_1\rangle$ states (4.2.5). H is the Hadamard gate, X is the Pauli-X gate, the line spanning the two sites represents the CNOT gate from qubit 0 to target qubit 1, and P is the phase gate. Right panel: Circuit diagram of $\tilde{W}_a$ gates needed to construct the singlet state $|S_2\rangle$.

obtain (4.2.7) we need to transform from the real hopping amplitude used in [102] to our imaginary one).

Let us emphasize that the Hamiltonian H does not respect all the symmetries possessed by the two scar sectors. In particular, it breaks translation invariance while both $|n_O\rangle$ and $|n_U\rangle$ are manifestly invariant under lattice translations. Thus, the scars appear in the enhanced symmetry sectors of Hilbert space, in accordance with our general arguments.

Let us note that our construction of H_1 is similar to that in [94], in that hopping T is used to annihilate $\mathbb{S}$. Similarly to [100], [94] has discussed one of the two $SU(2)$ families of scar sectors in the context of the Hubbard model, although the $O(N)$ invariance of these states was not pointed out explicitly.

4.3 Construction of group invariant states

The two states $|S_{1,2}\rangle$ (4.2.5) with zero entanglement entropy may be expressed as a product state with the use of the gates W_a and $\tilde{W}_a$ (see figure 4.5):

$$|S_1\rangle = \prod_{a=1}^{N} W_a |0\rangle , \quad |S_2\rangle = \prod_{a=1}^{N} \tilde{W}_a |0\rangle . \tag{4.3.1}$$

We will briefly review the construction of state $|S_1\rangle$ via well known gates that act on either one or two qubits at a time. First we will define the Hadamard gate, H; it acts on a single qubit at a time, sending $|0\rangle \to \frac{|0\rangle+|1\rangle}{\sqrt{2}}$ and $|1\rangle \to \frac{|0\rangle-|1\rangle}{\sqrt{2}}$. The Pauli gate, X, acts on a single qubit at a time, sending $|0\rangle \to |1\rangle$ and $|1\rangle \to |0\rangle$. It is also known as the bit-flip gate. The phase gate, P, leaves $|0\rangle$ invariant and sends $|1\rangle \to i\,|1\rangle$. The CNOT gate acts on two qubits at a time. It performs the 'not' operation on the second qubit only when the first is $|1\rangle$. We start with the state $|0_{a1}0_{a2}\rangle$ and apply the Hadamard gate to the first qubit,

$$H_1\ |0_{a1}0_{a2}\rangle = \frac{|0_{a1}0_{a2}\rangle + |1_{a1}0_{a2}\rangle}{\sqrt{2}}. \tag{4.3.2}$$

Applying the Pauli-X gate to the second qubit of the output, we find

$$X_2\, H_1\ |0_{a1}0_{a2}\rangle = \frac{|0_{a1}1_{a2}\rangle + |1_{a1}1_{a2}\rangle}{\sqrt{2}}. \tag{4.3.3}$$

After applying the CNOT gate, we have the following,

$$\mathrm{CNOT}_1\, X_2\, H_1\ |0_{a1}0_{a2}\rangle = \frac{|0_{a1}1_{a2}\rangle + |1_{a1}0_{a2}\rangle}{\sqrt{2}}. \tag{4.3.4}$$

Finally, we find $|S_1\rangle$ after applying the phase gate on the first qubit of the output,

$$|S_1\rangle = P_1 \,\mathrm{CNOT}_1 \, X_2 \, H_1 \, |0_{a1} 0_{a2}\rangle = \frac{|0_{a1} 1_{a2}\rangle + i \, |1_{a1} 0_{a2}\rangle}{\sqrt{2}}. \tag{4.3.5}$$

We can perform similar computations to build $|S_2\rangle$.

Let us also present another, rotated basis for the family of states (4.2.6), which are $U(N)$ invariant and transform as spin-$N/2$ under the rotational $SU(2)$ symmetry:

$$|\tilde{n}_U\rangle = \frac{\left(\sum_a c^\dagger_{a1} c_{a2}\right)^n}{2^n \sqrt{\frac{N! n!}{(N-n)!}}} \, |\tilde{S}_2\rangle \,, \tag{4.3.6}$$

with $n = 0, \ldots, N$. Here

$$|\tilde{S}_1\rangle = \prod_{a=1}^{N} c^\dagger_{a1} \, |0\rangle \;\; , \qquad |\tilde{S}_2\rangle = \prod_{a=1}^{N} c^\dagger_{a2} \, |0\rangle \;\; . \tag{4.3.7}$$

We note that these states are singlets under the pseudospin symmetry. For the Hamiltonian H_0 in (4.2.1), the states $|\tilde{n}_U\rangle$ are not eigenstates, while the states $|n_U\rangle$ given in (4.2.6) are. However, for the Fermi-Hubbard and Heisenberg models, which respect the $SU(2)$ rotational symmetry, both $|\tilde{n}_U\rangle$ and $|n_U\rangle$ are eigenstates.

As shown in section 4.2.1, some singlet states in the vector model are related to the η-pairing states discovered by Yang [102]. We can extend this construction to the matrix model that was discussed in [18]. We start with the vacuum state $|0\rangle$ that is naturally a singlet state, because it is annihilated by any hopping. Then in order to build any other singlet state we can act with the creation operator and pair the index

with the use of the δ - pairing or ϵ - pairing. Namely, we introduce

$$(J_+)_{aa'} = c^\dagger_{ab} c^\dagger_{a'b}, \quad (K_+)_{a_1 \ldots a_{N_1}} = \epsilon_{b_1 \ldots b_{N_2}} \prod_{i=1}^{N_{1/2}} c^\dagger_{a_i b_i}. \tag{4.3.8}$$

These operators automatically are singlets under the action of $SO_b(N)$. Then the singlet states could be constructed out of the products and sums of the operators J_+, K_+ by contracting indices with the use of $\delta_{aa'}$ or $\epsilon_{a_1 \ldots a_N}$.

The states with a small number of fermions could be built with the use of only the operator matrix J_+. We introduce $\mathcal{M}_n = \sum_a \left(J_+^n\right)_{aa}$, which is a singlet under the action of $SO_a(N) \times SO_b(N)$. For example, acting with $\mathcal{M}_n$ and their products we can build singlet states as

$$|s_1\rangle = \mathcal{M}_2 |0\rangle, \quad |s_2\rangle = \mathcal{M}_3 |0\rangle, \quad |s_3\rangle = \mathcal{M}_3 \mathcal{M}_4 \mathcal{M}_2^2 |0\rangle, \ \ldots \tag{4.3.9}$$

When the number of fermions is larger than N, we can use K_+ to build singlet states. For example, when N is even we can have

$$|s_\epsilon\rangle = (K_+)_{a_1 a_1 \ldots a_{N/2} a_{N/2}} |0\rangle. \tag{4.3.10}$$

For $N = 2$ the operator $(K_+)_{aa}$ is the η-operator from [102].

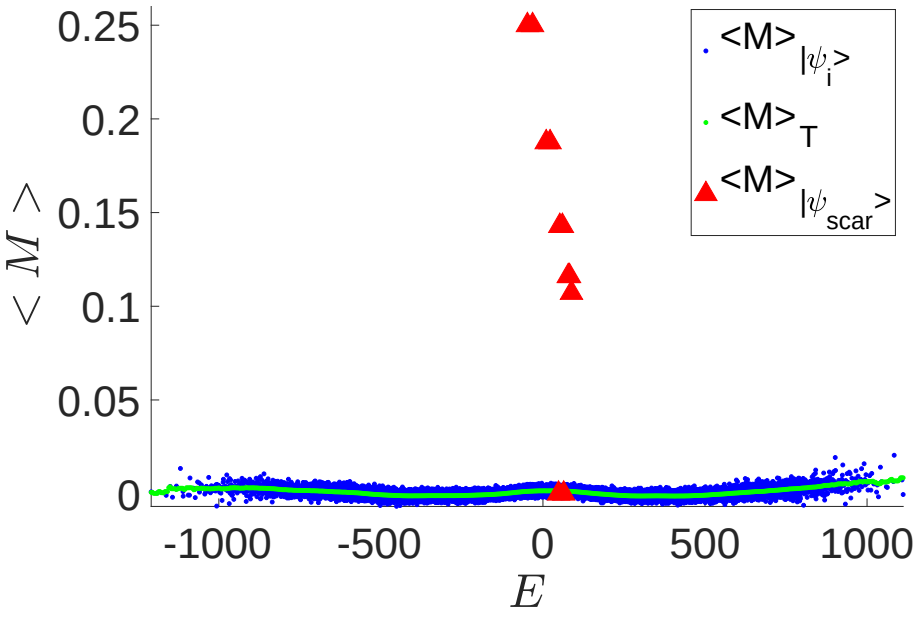

Figure 4.6: Correlator $G_U = \langle c^\dagger_{11} c_{12} c^\dagger_{42} c_{41} \rangle$ evaluated for every eigenstate of the vector model with $N = 8$. The value of G_U for this family of scar states is $G_U = \frac{1}{4} - \frac{n(N-n)}{2N(N-1)}$.

In general we are able to express the dimension of the singlet subspace as an integral [18]

$$\dim \mathbb{S}_O = \\ = \frac{4^{N_1 N_2}}{V_{N_1} V_{N_2}} \int_{-\pi}^{\pi} \prod_{i,j=1}^{N_1,N_2} dx_i dy_j \left(\cos x_i + \cos y_j\right)^2 \times \\ \times \prod_{i \neq i'}^{N_1} \left(\cos x_i - \cos x_{i'}\right)^2 \prod_{i \neq i'}^{N_2} \left(\cos y_i - \cos y_{i'}\right)^2 , \tag{4.3.11}$$

where V_{N_1,N_2} are the dimensions of the $SO(N)$ groups, which are equal to

$$V_{N_1} = \int_{-\pi}^{\pi} \prod_{i}^{N_1} dx_i \times \prod_{i \neq i'}^{N_1} (\cos x_i - \cos x_{i'})^2 . \tag{4.3.12}$$

4.4 Two-dimensional tJU model

We illustrate the concepts discussed above using the example of a perturbed tJU model on a 2D rectangular bipartite lattice. Here, we use the standard notation for the fermion numbers at site i:

$$n_{i\uparrow} = c^{\dagger}_{i\uparrow} c_{i\uparrow} , \quad n_{i\downarrow} = c^{\dagger}_{i\downarrow} c_{i\downarrow} , \quad n_i = n_{i\uparrow} + n_{i\downarrow} . \tag{4.4.1}$$

The total fermion number is expressed as, $Q = \sum_{i=1}^{N} n_i$. In addition, we can define the spin operator at site i as,

$$\vec{S}_i = \frac{1}{2} c^{\dagger}_{i\alpha} \vec{\sigma}_{\alpha\beta} c_{i\beta}, \tag{4.4.2}$$

where $\vec{\sigma}$ are the Pauli matrices.

The Hamiltonian of the standard tJU model [112–114] combines the Hubbard and Heisenberg interactions

$$\begin{aligned} H^{tJU} = t \sum_{\langle ij \rangle \sigma} c^{\dagger}_{i\sigma} c_{j\sigma} + J \sum_{\langle ij \rangle} \vec{S}_i \cdot \vec{S}_j + \\ + U \sum_i n_{i\uparrow} n_{i\downarrow} - \mu Q \end{aligned} \tag{4.4.3}$$

and can be viewed as a generalization of Hubbard or t-J models relevant for high-T_c superconductivity [115].

The $H_0 + OT$ decomposition of this model can be performed with respect to the $U(N)$ group, which gives us the $|\tilde{n}_U\rangle$ family of group-invariant scars as seen in (4.3.6). To construct this decomposition, we must introduce several useful generators of $SU(N)$. The generators of $SU(N)$ include the spin-independent hopping terms with generally complex amplitudes:

$$T_{ij} = \lambda c^\dagger_{i\sigma} c_{j\sigma} + \text{h.c.}, \quad \lambda \in \mathbb{C}. \tag{4.4.4}$$

We may now define a nearest-neighbor hopping with real amplitude,

$$T'_{\langle i,j\rangle} = c^\dagger_{i\sigma} c_{j\sigma} + h.c. \tag{4.4.5}$$

As $T'_{\langle i,j\rangle}$ is a Hermitian, spin-independent hopping term, it is a linear combination of T_{ij}, and thus belongs to the $SU(N)$ algebra and will annihilate the $SU(N)$ singlets.

Next, we define a set of generators of $U(N)$,

$$K_i = n_i - 1 \ , \qquad i = 1, \dots N \ . \tag{4.4.6}$$

In terms of the local magnetization M_i,

$$K_i^2 = 1 - M_i^2 \ , \tag{4.4.7}$$

where $M_i^2 = (n_{i\uparrow} - n_{i\downarrow})^2$. Lastly, we define a linear combination of $SU(N)$ generators,

$$C_{ij} = -\frac{1}{4}\left(E_{ij}E_{ji} + E_{ji}E_{ij} + K_iK_j\right), \tag{4.4.8}$$

where $E_{ij} = c_{ia}^\dagger c_{ja}$ are $SU(N)$ generators.

Now, we can express $\vec{S}_i \cdot \vec{S}_j$ in terms of the C_{ij} $SU(N)$ generators. Let us first expand $\vec{S}_i \cdot \vec{S}_j$,

$$\begin{aligned}
4\vec{S}_i \cdot \vec{S}_j &= \left(c_{i\uparrow}^\dagger c_{i\uparrow} - c_{i\downarrow}^\dagger c_{i\downarrow}\right)\left(c_{j\uparrow}^\dagger c_{j\uparrow} - c_{j\downarrow}^\dagger c_{j\downarrow}\right) + \left(c_{i\uparrow}^\dagger c_{i\downarrow} + c_{i\downarrow}^\dagger c_{i\uparrow}\right)\left(c_{j\uparrow}^\dagger c_{j\downarrow} + c_{j\downarrow}^\dagger c_{j\uparrow}\right) \\
&\quad - \left(c_{i\uparrow}^\dagger c_{i\downarrow} - c_{i\downarrow}^\dagger c_{i\uparrow}\right)\left(c_{j\uparrow}^\dagger c_{j\downarrow} - c_{j\downarrow}^\dagger c_{j\uparrow}\right) \\
&= -c_{i\alpha}^\dagger c_{j\alpha} c_{j\beta}^\dagger c_{i\beta} - c_{j\alpha}^\dagger c_{i\alpha} c_{i\beta}^\dagger c_{j\beta} - c_{i\alpha}^\dagger c_{i\alpha} c_{j\beta}^\dagger c_{j\beta} + c_{i\alpha}^\dagger c_{i\alpha} + c_{j\alpha}^\dagger c_{j\alpha} \\
&= 1 - E_{ij}E_{ji} - E_{ji}E_{ij} - K_iK_j
\end{aligned}$$

And so we can simplify,

$$\vec{S}_i \cdot \vec{S}_j = \frac{1}{4} + C_{ij}. \tag{4.4.9}$$

Here, we decompose the tJU Hamiltonian (4.4.3) with respect to $U(N)$,

$$\begin{aligned}
H^{tJU} &= t\sum_{\langle ij\rangle\sigma} c_{i\sigma}^\dagger c_{j\sigma} + J\sum_{\langle ij\rangle} \vec{S}_i \cdot \vec{S}_j + U\sum_i n_{i\uparrow}n_{i\downarrow} - \mu Q \\
&= t\sum_{\langle ij\rangle} T'_{\langle i,j\rangle} + J\sum_{\langle ij\rangle}\left(\frac{1}{4} + C_{ij}\right) - \mu Q + U\sum_i\left(n_{i\uparrow}n_{i\downarrow} - \frac{n_{i\uparrow}+n_{i\downarrow}}{2} + \frac{n_{i\uparrow}+n_{i\downarrow}}{2}\right) \\
&= t\sum_{\langle ij\rangle} T'_{\langle i,j\rangle} + \frac{J}{4}N_1^{nn} + J\sum_{\langle ij\rangle} C_{ij} + Q\left(\frac{U}{2} - \mu\right) - \frac{UN}{2} + \frac{U}{2}\sum_i\left(1 - (n_{i\uparrow} - n_{i\downarrow})^2\right) \\
&= t\sum_{\langle ij\rangle} T'_{\langle i,j\rangle} + \frac{J}{4}N_1^{nn} + J\sum_{\langle ij\rangle} C_{ij} + Q\left(\frac{U}{2} - \mu\right) - \frac{UN}{2} + \frac{U}{2}\sum_i K_i^2,
\end{aligned}$$

where in the third line we let N_1^{nn} denote the numbers of nearest-neighbor pairs in a particular lattice. Rearranging, we have

$$H^{tJU} = \frac{J}{4}N_1^{nn} + Q\left(\frac{U}{2} - \mu\right) - \frac{UN}{2} + t\sum_{\langle ij\rangle} T'_{\langle ij\rangle} + J\sum_{\langle ij\rangle} C_{ij} + \frac{U}{2}\sum_i K_i^2 \ , \tag{4.4.10}$$

where we have used the $H_0 + OT$ decomposition of individual terms (4.4.5), (4.4.7), (4.4.9). The first line of equation (4.4.10) is H_0 and acts on the invariant states with a constant while the second OT line only consists of terms proportional to group generators that annihilate the invariant states.

We recall that a group G-invariant states become scars in a model that can be written as $H_0 + \sum_k O_k T_k$ where T_k are generators of G. Note that a generator of any subgroup of G is also a generator of G and can also appear as T_k in the decomposition. The standard tJU model (4.4.3) conserves the total physical spin. Therefore the states $|\tilde{n}_U\rangle$ form a separate symmetry sector of this model. To make them true scars we break the total spin conservation by adding a perturbation. It is a symmetry-breaking term of the OT form for a rectangular lattice in two dimensions, where i labels the horizontal and j the vertical direction:

$$H_H^p = \sum_{i,j} r_{ij}(\tilde{M}_{ij} + \tilde{M}_{(i+1)j})S_{ij}^{\text{hor}} + q_{ij}(\tilde{M}_{ij} + \tilde{M}_{i(j+1)})S_{ij}^{\text{vert}} \ , \tag{4.4.11}$$

where $r_{ij}, q_{ij} \in [0,1]$ are real random numbers and

$$\begin{aligned} \tilde{M}_{ij} &= r_M c^\dagger_{ij\uparrow} c_{ij\uparrow} - q_M c^\dagger_{ij\downarrow} c_{ij\downarrow} \ , \\ S^{\rm hor}_{ij} &= \sum_\sigma c^\dagger_{(i+1)j\sigma} c_{ij\sigma} + \text{h.c.} \ , \\ S^{\rm vert}_{ij} &= \sum_\sigma c^\dagger_{i(j+1)\sigma} c_{ij\sigma} + \text{h.c.} \ , \end{aligned} \tag{4.4.12}$$

where r_M, q_M are also random numbers, that we chose to be $r_M = 1.426974$ and $q_M = 2.890703$.

The full Hermitian Hamiltonian we study numerically reads

$$H^{tJU}_h = H^{tJU} + \beta H^p_h + \gamma Q_2 \ , \tag{4.4.13}$$

where we added a term proportional to the $SU(2)_{spin}$ generator Q_2 (4.2.3). It acts as H_0 on $|\tilde{n}_U\rangle$ and splits them according to the index n: $Q_2 |\tilde{n}_U\rangle = (2n - N) |\tilde{n}_U\rangle$). Note that by increasing γ we can make the scar state with maximum Q_2, $|S_1\rangle$ (4.4.17), the ground state.

We may also consider a non-Hermitian perturbation to our model. One often describes an open system by a non-Hermitian Hamiltonian that results from a reduction of the Hermitian Hamiltonian of the full system to an open subsystem. The non-Hermitian Hamiltonian may not conserve the norm of the state which corresponds to the probability leaking out or into the open system. To illustrate that the invariant states remain stable and decoupled also in non-Hermitian systems with

Hamiltonian $H_0 + OT$, we consider the following non-Hermitian term.

$$H^p_{nH} = \sum_{i,j} (\tilde{M}_{ij} - \tilde{M}_{(i+1)j}) S^{\text{hor}}_{ij} + q_{ij} (\tilde{M}_{ij} - \tilde{M}_{i(j+1)}) S^{\text{vert}}_{ij} \ . \tag{4.4.14}$$

Thus, the full non-Hermitian Hamiltonian we consider is

$$H^{tJU}_{nh} = H^{tJU}_h + \beta_1 H^p_{nh}, \tag{4.4.15}$$

where for numerical investigations we set $\beta_1 = 0.4\beta$. In both the Hermitian and the non-Hermitian cases, the part of the full Hamiltonian that acts with a constant on the invariant states is

$$E_0^{|\tilde{n}_U\rangle} = \frac{J}{4} N_1^{nn} + \left(\frac{U}{2} - \mu \right) Q - \frac{UN}{2} + \gamma Q_2. \tag{4.4.16}$$

The states in equation (4.2.6) are not the eigenstates of (4.4.16). Instead, the basis in the $SU(N)$-invariant subspace determined by the Hamiltonian (4.4.16) reads

$$\begin{aligned} |n_{tJU}\rangle = |n_U\rangle &= \frac{\zeta^n}{2^n \sqrt{\frac{N! n!}{(N-n)!}}} |S_1\rangle \ , \\ |S_1\rangle &= \prod_a \frac{c^\dagger_{a1} + i c^\dagger_{a2}}{\sqrt{2}} |0\rangle \ , \end{aligned} \tag{4.4.17}$$

where $\zeta = Q_3 - iQ_1$, as in (4.2.6).

Because both Hermitian and non-Hermitian models we consider have an exact $H_0 + OT$ decomposition, they have the family $|\tilde{n}_U\rangle$ as scars for any choices of the coupling constants.[c]

4.4.1 Numerical results

For the numerical experiment we use the $N_x \times N_y = 3 \times 3$ lattice and set $t = -0.4$, $J = 1$, $U = 8$, $\mu = 1.3$. For $\gamma = 1$ this corresponds to the g.s. filling of $\nu = \frac{Q}{2N} = 0.44(4)$, 11% below the half-filling which corresponds to the potentially high-T_c-relevant regime [116, 117]. For our simulation we instead choose $\gamma = 3.6$. At this value the half-filled $|S_1\rangle$ state (4.4.17) becomes the ground state. This simplifies the initialization of the system to the scar subspace in experiment. Because $|S_1\rangle$ is a product state, it can alternatively be created by application of a simple gate circuit on each site (see figure 4.5).

The level statistics parameters of $r = 0.5306$ ($r^{GOE} = 0.5359$) and $r_{nh} = 0.7378$ ($r^{Ginibre} \approx 0.74$) are close to the values of the corresponding random ensembles (defined in the introduction) and thus indicate that the bulk spectra of both systems are fully chaotic. This is further elaborated by the gap distribution (figure 4.9 and 4.11) and by the presence of the 'dip-ramp-plateau' structure in the spectral structure factor plot figure (4.9) typical for chaotic systems.

In the spectrum of the non-Hermitian Hamiltonian (4.4.15) (see figure 4.8) we observe that all the scar states remain at the real axis and are not effected by the non-

[c]The tJU model (4.4.3) has another $H_0 + OT$ decomposition, leading to a second family of group invariant scars. This family is not presented here; however, the details of the second family of scars is presented in [48].

Hermitian terms. The non-Hermitian spectrum also has a 'conjugation symmetry': for every state with energy $a + ib$ there is another state with energy $a - ib$. All the observables measured in any two such states (such as entanglement entropy) are also equal. For this reason we choose to plot such observables as a function of the real part of the energy eigenvalue: $\mathrm{Re}\, E$.

To demonstrate the violation of strong ETH we evaluate the 'magnetic' (4.4.21) off-diagonal long-range order (ODLRO) correlator characteristic of the $|\tilde{n}_U\rangle$ [47] states. We observe (see figure 4.12) that the corresponding expectation values are significantly different in the invariant states relative to all the generic states in the spectrum in both systems which allows us to conclude the invariant states are scars in this system.

One of the most striking and counterintuitive features of the scar states in the non-Hermitian Hamiltonian (4.4.15) is the stable and coherent time evolution of the scar subspace shown in figure 4.7. The system is initialized to a state that is a uniform mix of all the $2N+2 = 20$ scar states present in the system. This state is coming back to itself exactly after the time intervals $2\pi/\omega \approx 20.94$, where $\omega = 0.3$ is the greatest common divisor of all the gaps between the scar states. The norm of the state is preserved throughout, although the system is open (Hamiltonian is non-Hermitian) and the probability density would flow in or out of the system for an initial state that includes any admixture of a non-singlet generic states. As expected, stable revivals are also observed for the Hermitian Hamiltonian.

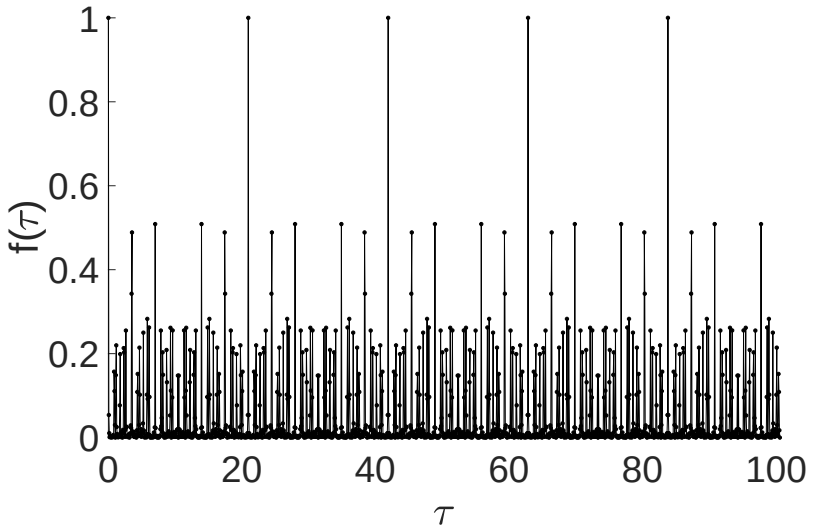

Figure 4.7: Time dependence of the squared overlap between the initial state and a time-evolved state for the non-Hermitian Hamiltonian (4.4.15).

4.4.1.1 Spectrum

The imaginary and real components of the eigenvalues of equation (4.4.15) are shown in figure 4.8. While the majority of the eigenvalues of the non-Hermitian Hamiltonian become complex the eigenvalues corresponding to the invariant scar states remain real and the same as in the system without a non-Hermitian term. This demonstrates the stability of the many-body scar states in suitably designed open systems.

The spectrum also exhibits the conjugation symmetry: for every eigenvalue $E = E_r + iE_{im}$ there is a partner state with $E = E_r - iE_{im}$.

4.4.1.2 Quantum chaos in the Hermitian Hamiltonian

The mean level spacings ratio, $\langle r \rangle$, is often used to quantify chaos as well as spectral transitions between Wigner-Dyson ensembles. The spacing ratio, r, is reviewed in the

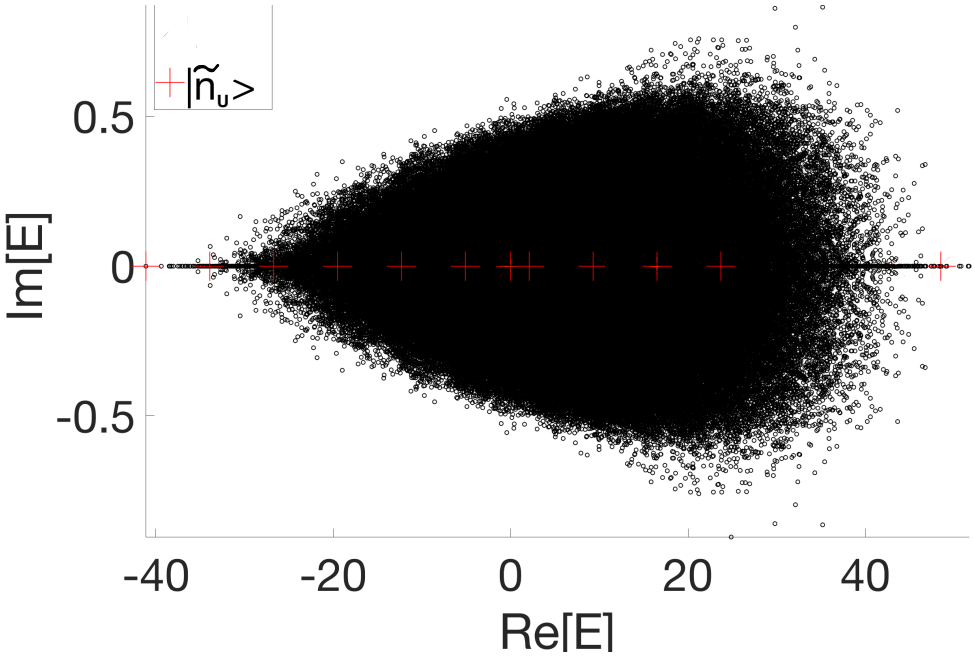

Figure 4.8: $N_x = 3$ $N_y = 3$ non-Hermitian tJU spectrum. All the particle number sectors are plotted together. Figure is adapted from reference [47].

introduction,

$$r = \frac{s_i}{s_{i-1}} \quad \text{where,} \quad s_i = \lambda_{i+1} - \lambda_i, \tag{4.4.18}$$

where λ_i is the i^{th} eigenvalue. See equation (4.4.20) for the definition for a non-Hermitian system. The analytic mean level spacings ratios are calculated in [40], and are $\langle r \rangle \approx 0.5359$, $\langle r \rangle \approx 0.6027$, and $\langle r \rangle \approx 0.6762$ for the GOE, GUE, and GSE respectively.

Based on the figures 4.9 and 4.10, we can conclude that our Hermitian models have a chaotic bulk; the SFF has a dip ramp plateau structure, and the level spacings plots and $\langle r \rangle$ values closely match those of the GOE.

4.4.1.3 Quantum chaos in the non-Hermitian Hamiltonian

The Ginibre symmetry classes are the non-Hermitian analogs to the Dyson symmetry classes. We can compute the level spacings of our non-Hermitian models and compare to those of the Ginibre random matrix analog. It is also possible to compute complex spacing ratios $\langle r \rangle$. For example, the Ginibre GUE (GinUE) $\langle r \rangle$ is numerically determined to be ≈ 0.74 [118].

The definition of a nearest neighbor for a non-Hermitian matrix is [119]:

$$d_\alpha = \min_\beta |E_\alpha - E_\beta| \,. \tag{4.4.19}$$

The r-value is defined as [118].

$$r_n = \left| \frac{d_n^{N_1} - d_n}{d_n^{N_2} - d_n} \right| \tag{4.4.20}$$

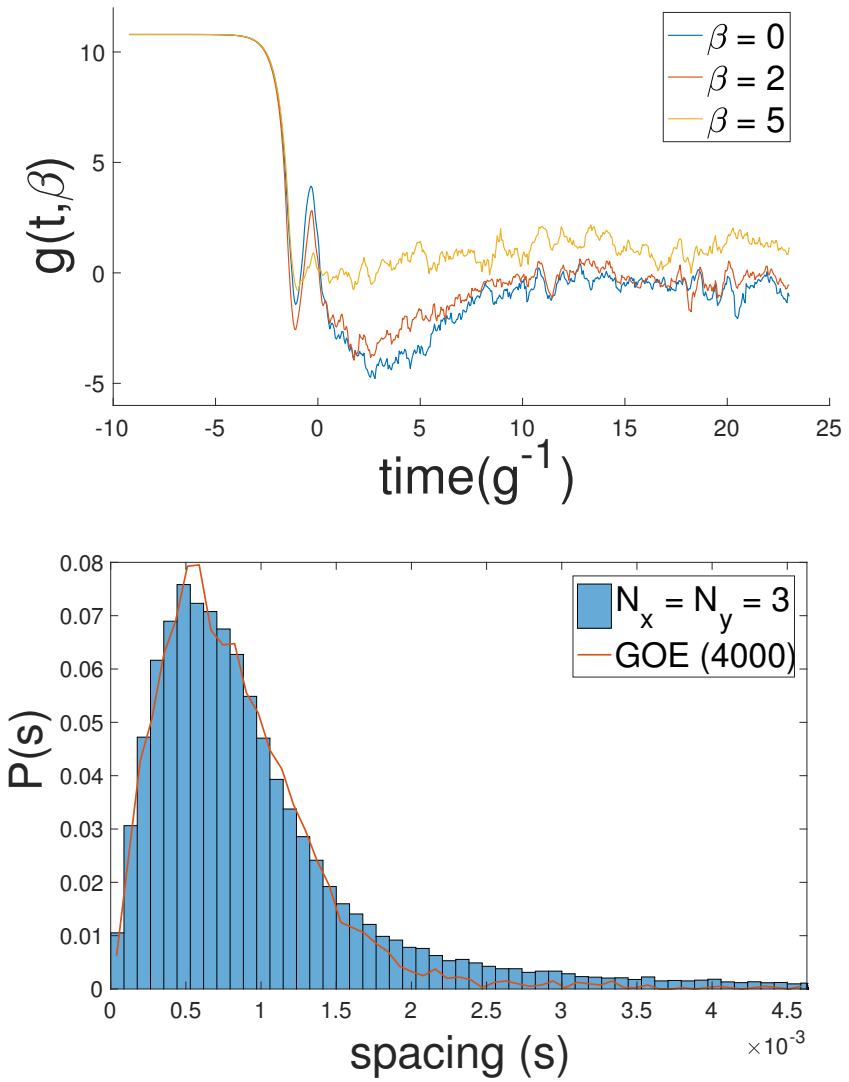

Figure 4.9: Quantum chaos for Hermitian tJU 3x3 $\gamma = 3.6$. Top: SFF. Bottom: Ps. This model has $\langle r \rangle = 0.5306$. $\langle r \rangle_{GUE} = 0.6027$ and $\langle r \rangle_{GOE} = 0.5359$ [40]. Large magnetic field $\gamma = 3.6$ causes the correlations at one corresponding frequency that results in the peak seen in the SFF plot soon after the dip. This peak is absent or much reduced for the moderate magnetic field $\gamma = 1$ (see figure 4.10)

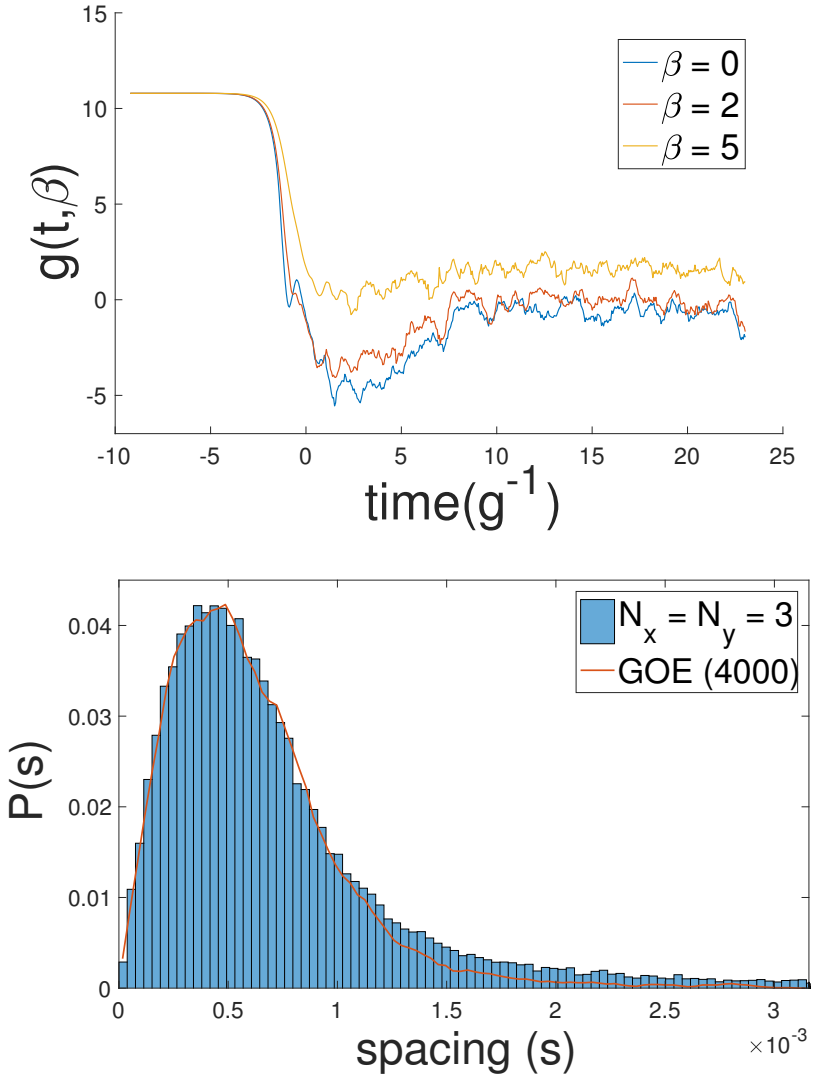

Figure 4.10: Quantum chaos for Hermitian tJU 3x3 $\gamma = 1$. Top: SFF. Bottom: Ps. This model has $\langle r \rangle = 0.5284$. $\langle r \rangle_{GUE} = 0.6027$ and $\langle r \rangle_{GOE} = 0.5359$.

where N_1 is the nearest neighbor and N_2 is the next nearest neighbor.

We can see from figure 4.11, that our non-Hermitian model shows evidence of a chaotic bulk. The level spacings plot fits closely to that of the Ginibre distribution, and the $\langle r \rangle$ value of our model is also close to the Ginibre value. The interpretation of the SFF for the non-Hermitian model is less straightforward, though we do see a dip ramp plateau structure when considering only the real part of the eigenvalues. The dip ramp plateau structure is less clear when considering only the magnitude or imaginary part of the eigenvalues.

4.4.1.4 ETH violation

The violation of strong ETH by the scar states is demonstrated in figure 4.12 for the Hermitian and the non-Hermitian Hamiltonians. We evaluate the expectation values for the operator that defines the off-diagonal long-range order of the scar family considered:

$$G_U = \langle c^\dagger_{x_1 y_1 \uparrow} c_{x_1 y_1 \downarrow} c^\dagger_{x_2 y_2 \downarrow} c_{x_2 y_2 \uparrow} \rangle \tag{4.4.21}$$

for $|\tilde{n}_U\rangle$ introduced in [47].

Because of the high symmetry of the invariant states, this correlator, when evaluated for scars, does not depend on the coordinates x_1, y_1, x_2, y_2 [47]. For the numerical evaluation we set the points 1 and 2 to be the most distant points in our system with open boundaries: $(x_1, y_1) = (1, 1)$ and $(x_2, y_2) = (3, 3)$.

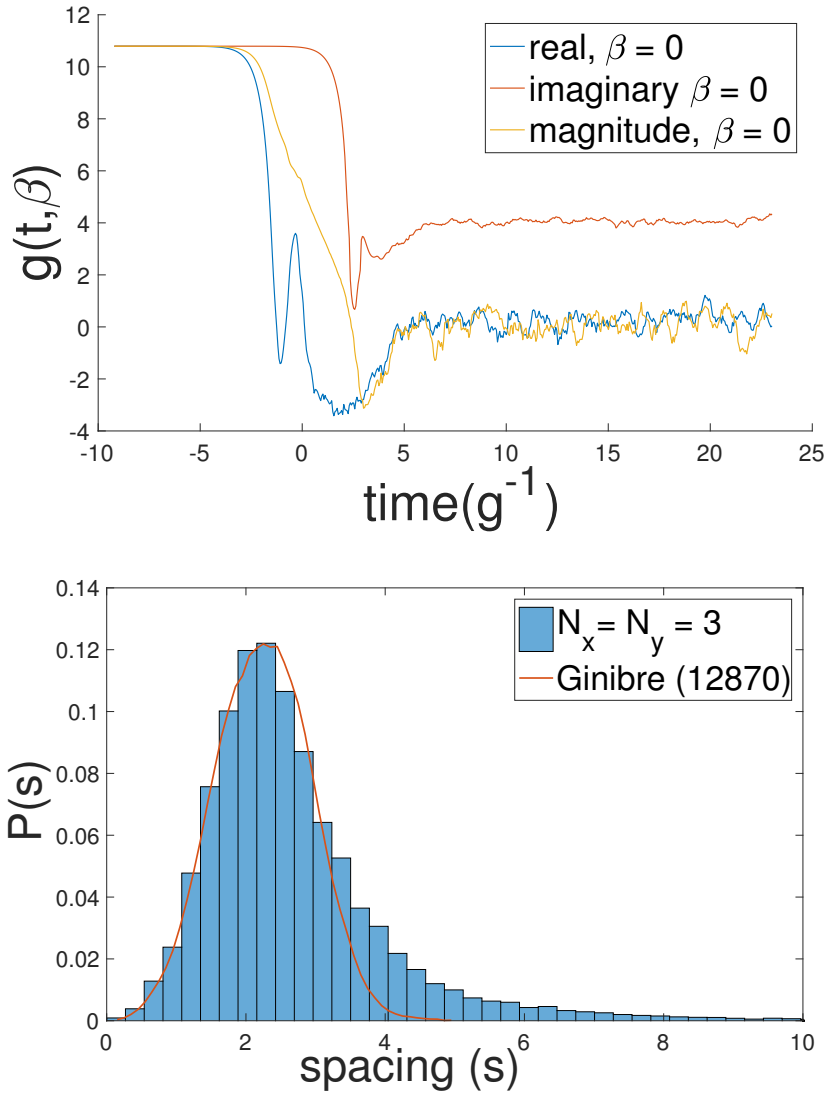

Figure 4.11: Top: SFF for non-Hermitian tJU 3x3, Bottom: Ps for non-Hermitian tJU 3x3. This model has $\langle r \rangle = 0.7378$. For reference, the Ginibre value $\langle r \rangle_{GinUE} \approx 0.74$ was supported numerically in [118].

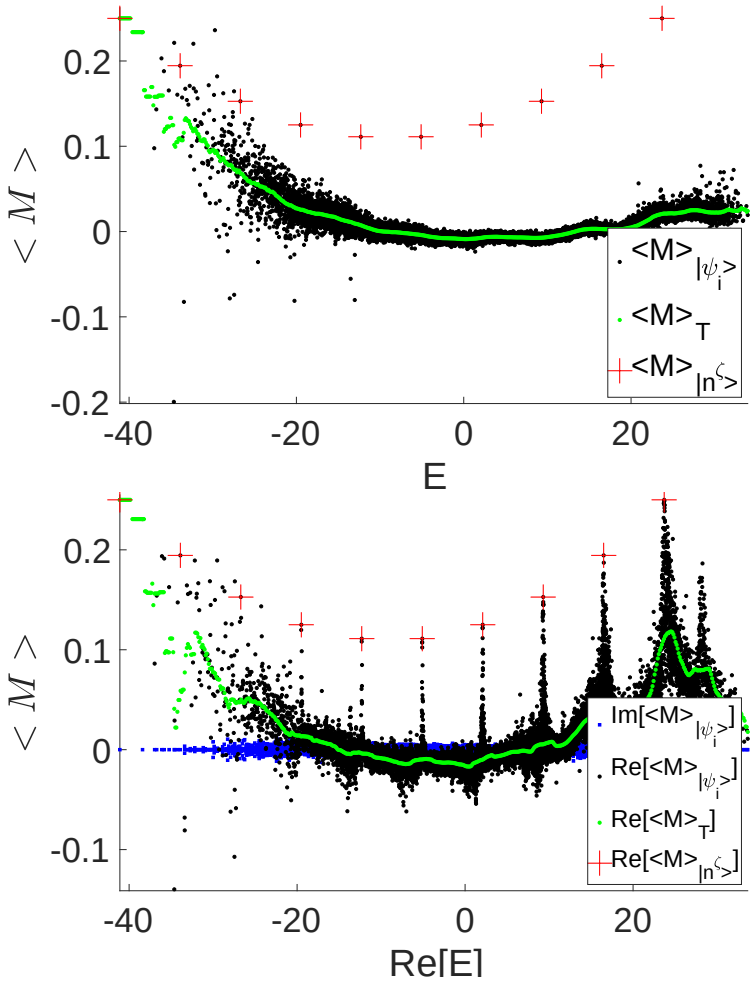

Figure 4.12: ETH violation by the scar states for the Hermitian Hamiltonian (4.4.13) (top) and ETH violation by the scar states for the non-Hermitian Hamiltonian (4.4.15) (bottom) for N_x=3 N_y=3. Shown is the expectation value $\langle\psi_i|M|\psi_i\rangle$ evaluated for every eigenstate ψ_i, with $Q = 9$ (half-filling) $M = G_U$. The green line is the micro-cononical (window) average.

The scar states are clearly away from the microcanonical average in both systems. A very strong magnetic field is present in both systems and couples to the states with non-zero magnetization. This results in the spikes seen in the data for the non-Hermitian system which is apparently more susceptible to the magnetic field.

4.5 Discussion

The presence of group invariant scar states $\mathbb{S}$ is a property of a Hilbert space once the conditions on the Hamiltonian outlined in this paper are satisfied. This universality explains why the scar states identified to date in different models with the same Hilbert space can be identical.

The group-invariance requirement is non-local, and the resulting scar states are invariant under lattice translations. As a consequence, the degrees of freedom on all of the sites become entangled which spreads the information over the whole system. This leads to the relative insensitivity of group-invariant states to local perturbations and protection of the quantum information [120]. The invariant scar states do not thermalize and form a closed, decoherence-free subspace, where non-commuting transformations can act and universal quantum computation may be performed [121]. This combination of properties makes the group-invariant scar states an interesting platform for robust quantum information processing.

The gauge/gravity duality [122–124] is a set of correspondences between conventional gauged models without gravity and higher-dimensional gravitational systems. In quantum mechanical models, gauge fields are non-dynamical, so the gauging is

equivalent to truncation of the Hilbert space to a group-invariant sector [2, 3, 18, 125–127]. It would be interesting to explore possible connections between the group-invariant scars and gauge/gravity duality.

The broad framework we presented allows for constructing a model that could be simply realized in experiment. An example Hamiltonian could be $B_y Q_2 + \sum_a (M_a + M_{a+1}) \left(c^\dagger_{a+1\sigma} c_{a\sigma} + \text{h.c.} \right)$, where $M_a = c^\dagger_{a1} c_{a1} - c^\dagger_{a2} c_{a2}$ is the magnetization at site a. The eigenstates include the translationally invariant $|n_U\rangle$ scars including $|S_1\rangle$ with $E_{S_1} = B_y N$ and $|S_2\rangle$ with $E_{S_2} = -B_y N$. In addition, we have demonstrated that the invariant scar subspace continues to undergo stable, coherent time evolution in a class of suitably designed open systems with non-Hermitian Hamiltonian. This greatly expands the realm of weak ergodicity breaking phenomena and will hopefully inspire new theoretical and experimental studies.

Bibliography

[1] S. Sachdev and J. Ye, "Gapless spin-fluid ground state in a random quantum Heisenberg magnet," *Phys. Rev. Lett.* **70** (May, 1993) 3339–3342, arXiv:cond-mat/9212030.

[2] E. Witten, "An SYK-like model without disorder," *Journal of Physics A: Mathematical and Theoretical* **52** (Oct, 2019) 474002, arXiv:1610.09758.

[3] I. R. Klebanov and G. Tarnopolsky, "Uncolored random tensors, melon diagrams, and the Sachdev-Ye-Kitaev models," *Phys. Rev.* **D95** (2017), no. 4 046004, arXiv:1611.08915.

[4] J. Maldacena and D. Stanford, "Comments on the Sachdev-Ye-Kitaev model," *Phys. Rev.* **D94** (2016), no. 10 106002, arXiv:1604.07818.

[5] R. Gurau, "Colored Group Field Theory," *Commun. Math. Phys.* **304** (2011) 69–93, arXiv:0907.2582.

[6] R. Gurau and V. Rivasseau, "The 1/N expansion of colored tensor models in arbitrary dimension," *Europhys. Lett.* **95** (2011) 50004, arXiv:1101.4182.

[7] R. Gurau, "The complete 1/N expansion of colored tensor models in arbitrary dimension," *Annales Henri Poincare* **13** (2012) 399–423, arXiv:1102.5759.

[8] V. Bonzom, R. Gurau, A. Riello, and V. Rivasseau, "Critical behavior of colored tensor models in the large N limit," *Nucl. Phys.* **B853** (2011) 174–195, arXiv:1105.3122.

[9] A. Tanasa, "Multi-orientable Group Field Theory," *J. Phys.* **A45** (2012) 165401, arXiv:1109.0694.

[10] V. Bonzom, R. Gurau, and V. Rivasseau, "Random tensor models in the large N limit: Uncoloring the colored tensor models," *Phys. Rev.* **D85** (2012) 084037, arXiv:1202.3637.

[11] S. Carrozza and A. Tanasa, "$O(N)$ Random Tensor Models," *Lett. Math. Phys.* **106** (2016), no. 11 1531–1559, arXiv:1512.06718.

[12] R. Gurau and J. P. Ryan, "Colored Tensor Models - a review," *SIGMA* **8** (2012) 020, arXiv:1109.4812.

[13] A. Tanasa, "The Multi-Orientable Random Tensor Model, a Review," *SIGMA* **12** (2016) 056, arXiv:1512.02087.

[14] N. Delporte and V. Rivasseau, "The Tensor Track V: Holographic Tensors," arXiv:1804.11101.

[15] I. R. Klebanov, F. Popov, and G. Tarnopolsky, "TASI Lectures on Large N Tensor Models," *PoS* **TASI2017** (2018) 004, arXiv:1808.09434.

[16] C. Krishnan, S. Sanyal, and P. N. Bala Subramanian, "Quantum Chaos and Holographic Tensor Models," *JHEP* **03** (2017) 056, arXiv:1612.06330.

[17] C. Krishnan and K. V. P. Kumar, "Towards a Finite-N Hologram," *JHEP* **10** (2017) 099, arXiv:1706.05364.

[18] I. R. Klebanov, A. Milekhin, F. Popov, and G. Tarnopolsky, "Spectra of eigenstates in fermionic tensor quantum mechanics," *Phys. Rev.* **D97** (2018), no. 10 106023, arXiv:1802.10263.

[19] C. Krishnan and K. P. Kumar, "Exact Solution of a Strongly Coupled Gauge Theory in 0+1 Dimensions," *Physical Review Letters* **120** (May, 2018) arXiv:1802.02502.

[20] C. Krishnan and K. V. P. Kumar, "Complete solution of a gauged tensor model," *Advances in Theoretical and Mathematical Physics* **23** (2019), no. 7 1805–1847, arXiv:1804.10103.

[21] K. Pakrouski, I. R. Klebanov, F. Popov, and G. Tarnopolsky, "Spectrum of Majorana Quantum Mechanics with $O(4)^3$ Symmetry," *Phys. Rev. Lett.* **122** (2019), no. 1 011601, arXiv:1808.07455.

[22] J. S. Cotler, G. Gur-Ari, M. Hanada, J. Polchinski, P. Saad, S. H. Shenker, D. Stanford, A. Streicher, and M. Tezuka, "Black Holes and Random Matrices," *JHEP* **05** (2017) 118, arXiv:1611.04650.

[23] D. Poland, S. Rychkov, and A. Vichi, "The conformal bootstrap: Theory, numerical techniques, and applications," *Reviews of Modern Physics* **91** (Jan, 2019) arXiv:1805.04405.

[24] M. Moshe and J. Zinn-Justin, "Quantum field theory in the large N limit: a review," *Physics Reports* **385** (Oct, 2003) 69–228, arXiv:hep-th/0306133.

[25] F. Kos, D. Poland, and D. Simmons-Duffin, "Bootstrapping the O(N) vector models," *Journal of High Energy Physics* **2014** (Jun, 2014) arXiv:1307.6856.

[26] G. Hooft, "A planar diagram theory for strong interactions," *Nuclear Physics B* **72** (1974), no. 3 461–473.

[27] A. Athenodorou and M. Teper, "SU(N) gauge theories in 2+1 dimensions: glueball spectra and k-string tensions," *Journal of High Energy Physics* **2017** (Feb, 2017) arXiv:1609.03873.

[28] K. Bulycheva, I. R. Klebanov, A. Milekhin, and G. Tarnopolsky, "Spectra of Operators in Large N Tensor Models," *Phys. Rev.* **D97** (2018), no. 2 026016, arXiv:1707.09347.

[29] S. Sachdev and J. Ye, "Gapless spin fluid ground state in a random, quantum Heisenberg magnet," *Phys. Rev. Lett.* **70** (1993) 3339, arXiv:cond-mat/9212030.

[30] A. Kitaev, "A simple model of quantum holography," *Talks at KITP, April 7, 2015 and May 27, 2015.*

[31] S. Sachdev, "Bekenstein-Hawking Entropy and Strange Metals," *Phys. Rev.* **X5** (2015), no. 4 041025, arXiv:1506.05111.

[32] J. Polchinski and V. Rosenhaus, "The Spectrum in the Sachdev-Ye-Kitaev Model," *JHEP* **04** (2016) 001, arXiv:1601.06768.

[33] A. Kitaev and S. J. Suh, "The soft mode in the Sachdev-Ye-Kitaev model and its gravity dual," *JHEP* **05** (2018) 183, arXiv:1711.08467.

[34] D. J. Gross and V. Rosenhaus, "A generalization of Sachdev-Ye-Kitaev," *Journal of High Energy Physics* **2017** (Feb, 2017) arXiv:1610.01569.

[35] V. Bonzom, V. Nador, and A. Tanasa, "Diagrammatic proof of the large N melonic dominance in the SYK model," *Letters in Mathematical Physics* **109** (Jul, 2019) 2611–2624, arXiv:1808.10314.

[36] Y. Gu, A. Kitaev, S. Sachdev, and G. Tarnopolsky, "Notes on the complex Sachdev-Ye-Kitaev model," *Journal of High Energy Physics* **2020** (Feb, 2020) arXiv:1910.14099.

[37] E. P. Wigner, "Characteristic Vectors of Bordered Matrices With Infinite Dimensions," *Annals of Mathematics* **62** (1955), no. 3 548–564.

[38] G. Livan, M. Novaes, and P. Vivo, "Introduction to Random Matrices," *SpringerBriefs in Mathematical Physics* (2018) arXiv:1712.07903.

[39] M. L. Mehta, "Random Matrices," vol. 142 of *Pure and Applied Mathematics*. Elsevier, 2004.

[40] Y. Y. Atas, E. Bogomolny, O. Giraud, and G. Roux, "Distribution of the Ratio of Consecutive Level Spacings in Random Matrix Ensembles," *Physical Review Letters* **110** (Feb, 2013) arXiv:1212.5611.

[41] H. Gharibyan, M. Hanada, S. H. Shenker, and M. Tezuka, "Onset of random matrix behavior in scrambling systems," *Journal of High Energy Physics* **2018** (Jul, 2018) arXiv:1803.08050.

[42] A. Altland and D. Bagrets, "Quantum ergodicity in the SYK model," *Nuclear Physics B* **930** (May, 2018) 45–68, arXiv:1712.05073.

[43] V. Oganesyan and D. A. Huse, "Localization of interacting fermions at high temperature," *Phys. Rev. B* **75** (Apr, 2007) 155111, arXiv:cond-mat/0610854.

[44] I. R. Klebanov, P. N. Pallegar, and F. K. Popov, "Majorana fermion quantum mechanics for higher rank tensors," *Phys. Rev. D* **100** (Oct, 2019) 086003, arXiv:1905.06264.

[45] P. N. Pallegar, "Poster: Majorana fermion quantum mechanics for higher rank tensors," in *Strings 2019–Brussels, Belgium*, July, 2019.

[46] P. N. Pallegar and W. Zhao, "Prismatic quantum mechanics with complex fermions." Work in progress.

[47] K. Pakrouski, P. N. Pallegar, F. K. Popov, and I. R. Klebanov, "Many-Body Scars as a Group Invariant Sector of Hilbert Space," *Phys. Rev. Lett.* **125** (Dec, 2020) 230602, arXiv:2007.00845.

[48] K. Pakrouski, P. N. Pallegar, F. K. Popov, and I. R. Klebanov, "Group theoretic approach to many-body scar states in fermionic lattice models," arXiv:2106.10300.

[49] P. Narayan and J. Yoon, "SYK-like tensor models on the lattice," *JHEP* (2017) 83, arXiv:1705.01554.

[50] F. Ferrari, V. Rivasseau, and G. Valette, "A New Large N Expansion for General Matrix-Tensor Models," arXiv:1709.07366.

[51] S. S. Gubser, C. Jepsen, Z. Ji, and B. Trundy, "Higher melonic theories," *Journal of High Energy Physics* **2018** (Sep, 2018) arXiv:1806.04800.

[52] M. Kobayashi, "Perfect one-factorizations of the complete graph," *Nagasaki university's academic output site* **4** (1988) 85–90.

[53] C. J. Colbourn and J. H. Dinitz, *Handbook of Combinatorial Designs*. Chapman and Hall/CRC, 2006.

[54] M. Berkooz, M. Isachenkov, V. Narovlansky, and G. Torrents, "Towards a full solution of the large N double-scaled SYK model," *Journal of High Energy Physics* **2019** (Mar, 2019) arXiv:1811.02584.

[55] A. Bernevig and T. Neupert, "Topological Superconductors and Category Theory," arXiv:1506.05805.

[56] C. Krishnan, K. V. P. Kumar, and S. Sanyal, "Random Matrices and Holographic Tensor Models," *JHEP* **06** (2017) 036, arXiv:1703.08155.

[57] M. Stephanov, J. Verbaarschot, and T. Wettig, "Random Matrices," arXiv : hep-ph/0509286.

[58] D. Freedman and A. Van Proeyen, *Supergravity*. Cambridge, 2012.

[59] V. Arnol'd, *Mathematical Methods of Classical Mechanics*. Springer-Verlag, 1989.

[60] P. Bocchieri and A. Loinger, "Quantum Recurrence Theorem," *Phys. Rev.* **107** (Jul, 1957) 337–338.

[61] J. Zhang and Y. Liu, "Witnessing a Poincaré recurrence with Mathematica," *Results in Physics* **7** (2017) 3373–3379, arXiv:1705.01444.

[62] García-García, Antonio M. and Verbaarschot, Jacobus J. M., "Analytical Spectral Density of the Sachdev-Ye-Kitaev Model at finite N," *Phys. Rev.* **D96** (2017) 066012, arXiv:1701.06593.

[63] D. Bagrets, A. Altland, and A. Kamenev, "Power-law out of time order correlation functions in the SYK model," *Nuclear Physics B* **921** (Aug, 2017) 727–752, arXiv:1702.08902.

[64] A. M. García-García and J. J. M. Verbaarschot, "Spectral and thermodynamic properties of the Sachdev-Ye-Kitaev model," *Phys. Rev.* **D94** (2016), no. 12 126010, arXiv:1610.03816.

[65] J. Cotler, N. Hunter-Jones, J. Liu, and B. Yoshida, "Chaos, complexity, and random matrices," *Journal of High Energy Physics* **2017** (Nov, 2017) 48, arXiv:1706.05400.

[66] D. J. Gross and V. Rosenhaus, "All point correlation functions in SYK," *Journal of High Energy Physics* **2017** (Dec, 2017) arXiv:1710.08113.

[67] A. Almheiri and J. Polchinski, "Models of AdS_2 backreaction and holography," *JHEP* **11** (2015) 014, arXiv:1402.6334.

[68] K. Jensen, "Chaos in AdS_2 Holography," *Phys. Rev. Lett.* **117** (2016), no. 11 111601, arXiv:1605.06098.

[69] J. Maldacena, D. Stanford, and Z. Yang, "Conformal symmetry and its breaking in two dimensional Nearly Anti-de-Sitter space," *PTEP* **2016** (2016), no. 12 12C104, arXiv:1606.01857.

[70] J. Engelsoy, T. G. Mertens, and H. Verlinde, "An investigation of AdS_2 backreaction and holography," *JHEP* **07** (2016) 139, arXiv:1606.03438.

[71] K. Bulycheva, "A note on the SYK model with complex fermions," *JHEP* **12** (2017) 069, arXiv:1706.07411.

[72] W. Fulton and J. Harris, *Representation Theory, A First Course*. Springer-Verlag, 1991.

[73] S. Prakash and R. Sinha, "Melonic dominance in subchromatic sextic tensor models," *Physical Review D* **101** (Jun, 2020) arXiv:1908.07178.

[74] S. Giombi, I. R. Klebanov, F. Popov, S. Prakash, and G. Tarnopolsky, "Prismatic large N models for bosonic tensors," *Phys. Rev. D* **98** (Nov, 2018) 105005, arXiv:1808.04344.

[75] S. Giombi, I. R. Klebanov, and G. Tarnopolsky, "Bosonic tensor models at large N and small ϵ," *Phys. Rev.* **D96** (2017), no. 10 106014, arXiv:1707.03866.

[76] S. Prakash and R. Sinha, "A Complex Fermionic Tensor Model in d Dimensions," *JHEP* **02** (2018) 086, arXiv:1710.09357.

[77] D. Benedetti, S. Carrozza, R. Gurau, and M. Kolanowski, "The $1/N$ Expansion of the Symmetric Traceless and the Antisymmetric Tensor Models in Rank Three," *Communications in Mathematical Physics* **371** (Aug, 2019) 55–97, arXiv:1712.00249.

[78] S. Carrozza, "Large N limit of irreducible tensor models: $O(N)$ rank-3 tensors with mixed permutation symmetry," *JHEP* **06** (2018) 039, arXiv:1803.02496.

[79] J. Murugan, D. Stanford, and E. Witten, "More on Supersymmetric and 2d Analogs of the SYK Model," *JHEP* **08** (2017) 146, arXiv:1706.05362.

[80] P. Breitenlohner and D. Z. Freedman, "Stability in gauged extended supergravity," *Annals of Physics* **144** (1982), no. 2 249–281.

[81] I. R. Klebanov and E. Witten, "AdS/CFT correspondence and symmetry breaking," *Nuclear Physics B* **556** (1999), no. 1 89–114, arXiv:hep-th/9905104.

[82] S. Moudgalya, N. Regnault, and B. A. Bernevig, "Entanglement of exact excited states of Affleck-Kennedy-Lieb-Tasaki models: Exact results, many-body scars, and violation of the strong eigenstate thermalization hypothesis," *Phys. Rev. B* **98** (Dec, 2018) 235156, arXiv:1806.09624.

[83] N. Shiraishi and T. Mori, "Systematic Construction of Counterexamples to the Eigenstate Thermalization Hypothesis," *Phys. Rev. Lett.* **119** (Jul, 2017) 030601, arXiv:1702.08227.

[84] C. J. Turner, A. A. Michailidis, D. A. Abanin, M. Serbyn, and Z. Papić, "Weak ergodicity breaking from quantum many-body scars," *Nature Physics* **14** (May, 2018) 745–749, arXiv:1711.03528.

[85] S. Choi, C. J. Turner, H. Pichler, W. W. Ho, A. A. Michailidis, Z. Papić, M. Serbyn, M. D. Lukin, and D. A. Abanin, "Emergent SU(2) Dynamics and Perfect Quantum Many-Body Scars," *Phys. Rev. Lett.* **122** (Jun, 2019) 220603, arXiv:1812.05561.

[86] V. Khemani and R. Nandkishore, "Local constraints can globally shatter Hilbert space: a new route to quantum information protection," *Phys. Rev. B* **101** (2020), no. 17 174204, arXiv:1904.04815.

[87] P. Sala, T. Rakovszky, R. Verresen, M. Knap, and F. Pollmann, "Ergodicity Breaking Arising from Hilbert Space Fragmentation in Dipole-Conserving Hamiltonians," *Physical Review X* **10** (Feb, 2020) arXiv:1904.04266.

[88] S. Moudgalya, A. Prem, R. Nandkishore, N. Regnault, and B. A. Bernevig, "Thermalization and its absence within Krylov subspaces of a constrained Hamiltonian," arXiv:1910.14048.

[89] M. Schecter and T. Iadecola, "Weak Ergodicity Breaking and Quantum Many-Body Scars in Spin-1 XY Magnets," *Phys. Rev. Lett.* **123** (2019), no. 14 arXiv:1906.10131.

[90] O. Vafek, N. Regnault, and B. A. Bernevig, "Entanglement of Exact Excited Eigenstates of the Hubbard Model in Arbitrary Dimension," *SciPost Phys.* **3** (2017) 043, arXiv:1608.06639.

[91] T. Iadecola and M. Žnidarič, "Exact Localized and Ballistic Eigenstates in Disordered Chaotic Spin Ladders and the Fermi-Hubbard Model," *Phys. Rev. Lett.* **123** (Jul, 2019) 036403, arXiv:1811.07903.

[92] N. Shibata, N. Yoshioka, and H. Katsura, "Onsager's Scars in Disordered Spin Chains," *Phys. Rev. Lett.* **124** (2020), no. 18 180604, arXiv:1912.13399.

[93] A. A. Michailidis, C. J. Turner, Z. Papić, D. A. Abanin, and M. Serbyn, "Stabilizing two-dimensional quantum scars by deformation and synchronization," *Physical Review Research* **2** (Jun, 2020) arXiv:2003.02825.

[94] D. K. Mark and O. I. Motrunich, "Eta-pairing states as true scars in an extended Hubbard model," *Physical Review B* **102** (Aug, 2020) arXiv:2004.13800.

[95] K. Bull, I. Martin, and Z. Papić, "Systematic Construction of Scarred Many-Body Dynamics in 1D Lattice Models," *Phys. Rev. Lett.* **123** (Jul, 2019) 030601, arXiv:1903.10491.

[96] V. Khemani, C. R. Laumann, and A. Chandran, "Signatures of integrability in the dynamics of Rydberg-blockaded chains," *Phys. Rev. B* **99** (Apr, 2019) 161101, arXiv:1807.02108.

[97] K. Lee, R. Melendrez, A. Pal, and H. J. Changlani, "Exact three-colored quantum scars from geometric frustration," *Physical Review B* **101** (2020), no. 24 241111, arXiv:2002.08970.

[98] D. K. Mark, C.-J. Lin, and O. I. Motrunich, "Unified structure for exact towers of scar states in the Affleck-Kennedy-Lieb-Tasaki and other models," *Physical Review B* **101** (2020), no. 19 195131, arXiv:2001.03839.

[99] T. Iadecola and M. Schecter, "Quantum many-body scar states with emergent kinetic constraints and finite-entanglement revivals," *Physical Review B* **101** (2020), no. 2 024306, arXiv:1910.11350.

[100] "Eta-pairing in Hubbard models: From spectrum generating algebras to quantum many-body scars," arXiv:2004.13727.

[101] G. Magnifico, M. Dalmonte, P. Facchi, S. Pascazio, F. V. Pepe, and E. Ercolessi, "Real Time Dynamics and Confinement in the $\mathbb{Z}_n$ Schwinger-Weyl lattice model for 1+1 QED," *Quantum* **4** (Jun, 2020) 281, arXiv:1909.04821.

[102] C. N. Yang, "η pairing and off-diagonal long-range order in a Hubbard model," *Phys. Rev. Lett.* **63** (Nov, 1989) 2144–2147.

[103] C. N. Yang and S. Zhang, "SO(4) symmetry in a Hubbard model," *Modern Physics Letters B* **4** (1990), no. 11 759–766.

[104] S. Zhang, "SO(4) Symmetry of the Hubbard Model and its Experimental Consequences," *International Journal of Modern Physics B* **05** (1991), no. 01n02 153–168, https://doi.org/10.1142/S0217979291000110.

[105] H. Bernien, S. Schwartz, A. Keesling, H. Levine, A. Omran, H. Pichler, S. Choi, A. S. Zibrov, M. Endres, M. Greiner, V. Vuletić, and M. D. Lukin, "Probing many-body dynamics on a 51-atom quantum simulator," *Nature* **551** (11, 2017) 579 EP–, arXiv:1707.04344.

[106] J. M. Deutsch, "Quantum statistical mechanics in a closed system," *Physical Review A* **43** (1991), no. 4 2046.

[107] M. Srednicki, "Chaos and quantum thermalization," *Physical Review E* **50** (1994), no. 2 888, arXiv:cond-mat/9403051.

[108] M. Rigol, V. Dunjko, and M. Olshanii, "Thermalization and its mechanism for generic isolated quantum systems," *Nature* **452** (2008), no. 7189 854–858, arXiv:0708.1324.

[109] X.-C. Wu, C.-M. Jian, and C. Xu, "Lattice models for non-Fermi liquids with tunable transport scalings," *Phys. Rev. B* **100** (Aug, 2019) 075101, arXiv:1902.10154.

[110] G. Gaitan, I. R. Klebanov, K. Pakrouski, P. N. Pallegar, and F. K. Popov, "Hagedorn Temperature in Large N Majorana Quantum Mechanics," *Phys. Rev. D* **101** (2020), no. 12 126002, arXiv:2002.02066.

[111] B. Buča, J. Tindall, and D. Jaksch, "Non-stationary coherent quantum many-body dynamics through dissipation," *Nature Communications* **10** (2019), no. 1 1730, arXiv:1804.06744.

[112] S. Daul, D. J. Scalapino, and S. R. White, "Pairing Correlations on $t - U - J$ Ladders," *Phys. Rev. Lett.* **84** (May, 2000) 4188–4191, arXiv:cond-mat/9907301.

[113] S. Basu, R. J. Gooding, and P. W. Leung, "Enhanced bound-state formation in two dimensions via stripelike hopping anisotropies," *Phys. Rev. B* **63** (Feb, 2001) 100506, arXiv:cond-mat/0010116.

[114] F. C. Zhang, "Gossamer Superconductor, Mott Insulator, and Resonating Valence Bond State in Correlated Electron Systems," *Phys. Rev. Lett.* **90** (May, 2003) 207002, arXiv:cond-mat/0209272.

[115] R. Micnas, J. Ranninger, and S. Robaszkiewicz, "Superconductivity in narrow-band systems with local nonretarded attractive interactions," *Rev. Mod. Phys.* **62** (Jan, 1990) 113–171.

[116] E. Dagotto, "Correlated electrons in high-temperature superconductors," *Rev. Mod. Phys.* **66** (Jul, 1994) 763–840, arXiv:cond-mat/9311013.

[117] M. Abram, M. Zegrodnik, and J. Spalek, "Antiferromagnetism, charge density wave, and d-wave superconductivity in the extended t-J-U model: role of intersite Coulomb interaction and a critical overview of renormalized mean field theory," *Journal of Physics: Condensed Matter* **29** (Aug, 2017) 365602, arXiv:1607.05399.

[118] L. Sá, P. Ribeiro, and T. c. v. Prosen, "Complex Spacing Ratios: A Signature of Dissipative Quantum Chaos," *Phys. Rev. X* **10** (Apr, 2020) 021019, arXiv:1910.12784.

[119] R. Hamazaki, K. Kawabata, N. Kura, and M. Ueda, "Universality classes of non-Hermitian random matrices," *Phys. Rev. Research* **2** (Jun, 2020) 023286, arXiv:1904.13082.

[120] A. Milekhin, "Quantum error correction and large N," arXiv:2008.12869.

[121] D. A. Lidar, I. L. Chuang, and K. B. Whaley, "Decoherence-Free Subspaces for Quantum Computation," *Phys. Rev. Lett.* **81** (Sep, 1998) 2594–2597, arXiv:quant-ph/9807004.

[122] J. M. Maldacena, "The Large N limit of superconformal field theories and supergravity," *Int. J. Theor. Phys.* **38** (1999) 1113–1133, arXiv:hep-th/9711200. [Adv. Theor. Math. Phys.2,231(1998)].

[123] S. S. Gubser, I. R. Klebanov, and A. M. Polyakov, "Gauge theory correlators from noncritical string theory," *Phys. Lett.* **B428** (1998) 105–114, arXiv:hep-th/9802109.

[124] E. Witten, "Anti-de Sitter space and holography," *Adv. Theor. Math. Phys.* **2** (1998) 253–291, arXiv:hep-th/9802150.

[125] D. J. Gross and I. R. Klebanov, "One-dimensional string theory on a circle," *Nucl. Phys. B* **344** (1990) 475–498.

[126] D. J. Gross and I. R. Klebanov, "Vortices and the nonsinglet sector of the $c = 1$ matrix model," *Nucl. Phys. B* **354** (1991) 459–474.

[127] J. Maldacena and A. Milekhin, "To gauge or not to gauge?," *JHEP* **04** (2018) 084, arXiv:1802.00428.